Title
Electrochemical Concentration Gradients Enable Novel Catalytic Routes

Author
Natinsky, Ben

Publication Date
2022

Peer reviewed|Thesis/dissertation

UNIVERSITY OF CALIFORNIA

Los Angeles

Electrochemical Concentration Gradients Enable Novel Catalytic Routes

A dissertation submitted in partial satisfaction

of the requirements for the degree Doctor of Philosophy in Chemistry

by

Benjamin Seth Natinsky

2022

ABSTRACT OF THE DISSERTATION

Electrochemical Concentration Gradients

Enable Novel Catalytic Routes

by

Benjamin Seth Natinsky

Doctor of Philosophy in Chemistry

University of California, Los Angeles, 2022

Professor Chong Liu, Chair

In biology, chemical species (such as oxygen (O_2)) and their local concentrations are highly regulated. One example is the reduction of dinitrogen (N_2) to ammonia by aerobic bacteria. In this scenario, the O_2 sensitive nitrogenase enzyme provides electrons for N_2 reduction through aerobic respiration. The tandem reactions of N_2 fixation and aerobic respiration are only possible due to the buildup of a chemical O_2 concentration gradient where the O_2 sensitive nitrogenase is situated in an O_2-free region and aerobic respiration in an O_2-rich region. Inspired by biological microscopic chemical gradients, my research aims to use electricity and nanomaterials to mimic these natural phenomena and apply them to synthetic organometallic chemistry to offer new pathways in carbon maintenance. Homogeneous organometallic complexes are often utilized for small molecule activation because they offer a delicate synthetic control and can be characterized

extensively, but can suffer from air or moisture sensitivity. Therefore, the marriage of traditional organometallic chemistry with electricity and nanoscience can help reconcile this incompatibility by offering new reactivity or unforeseen reaction routes. The projects described below illustrate the spatiotemporal control we can achieve over electroactive chemical species to induce novel catalytic routes and difficult-to-achieve transformations.

In my first research project (**Chapter 2**), I developed an electricity-powered catalytic system mediated by a Rh^{II} metalloradical complex for the conversion of methane (CH_4) to methanol (CH_3OH) with air as the terminal oxidant. The challenge here is that the Rh^{II} complex kinetically reacts with O_2 faster than with CH_4. I reconciled this incompatibility by introducing a nanowire electrode, which, when combined with a reducing potential, created a steep O_2 gradient within the wire array while also regenerating the Rh^{II} complex. Thus, C–H activation occurred anaerobically while CH_3OH synthesis proceeded aerobically together in one catalytic cycle. Moreover, the reaction rate of CH_4 activation increased 220,000-fold within the wire array, achieving a turnover number of 52,000 in 24 hours. Additionally, other light alkanes (such as ethane, propane, and toluene) were used as substrates and oxidation to primary alcohols was acheived in all cases.

Building off the work presented in **Chapter 2**, the work described in **Chapter 3** uncovers the identity and the role of the terminal oxidant responsible for generating CH_3OH from the methylated Rh complex. While O_2 reduction at the silicon nanowire array working electrode creates an anaerobic region within the wire array in air, it simultaneously generates the reactive oxygen species necessary for alcohol formation. The utilization of electron paramagnetic resonance spectroscopy identified the electrogenerated oxidant as superoxide and reactions with a selective chromophore quantified the rate of superoxide generation. While superoxide is the

immediately generated species at the electrode, it is presumed that chemical and/or further electrode reactions convert superoxide into a hydroperoxyl or hydroperoxide species, which is ultimately responsible for the oxidation reaction.

Chapter 4 investigates the role of the nanowire array's efficacy in creating a microscopic compartment for the Rh^{II} metalloradical-assisted CH_4 activation. While quantitative analysis of microscopic compartmentalization is typically applied to biochemical reactions, in this work we translated this quantitative understanding to organometallic cascade reactions in terms of reaction efficiency. We analyzed the reaction efficiency of our nanowire array compartment as the ratio of product molecules leaving the nanowire array to substrate molecules that enter the wire array compartment. In order to properly quantify this reaction metric, we utilized the experimental data obtained in **Chapter 3**. In conclusion, we found good agreement between our experimental results and the results from our semi-quantitative kinetic model.

The final chapter of my dissertation (**Chapter 5**) aims to translate the O_2 gradient observed previously to an electrochemical carbon monoxide (CO) gradient, from carbon dioxide (CO_2) reduction, to control the microstructure of synthetic polyketones. The ultimate goal of this project is to integrate, in one pot, the electroreduction of CO_2 to CO and the palladium (Pd) assisted copolymerization of CO and ethylene (C_2H_4). While polyketone synthesis typically follows a perfectly alternating pattern (1:1 stoichiometry between CO and C_2H_4), recent work has focused on utilizing Pd catalysts with asymmetric ligand frameworks to induce a non-alternating structure. The goal of this effort is to reduce the CO content (through extra C_2H_4 insertions) in order to improve the degradability of the polymer while maintaining its durability. However, non-alternating copolymerization still requires modulation of both the monomer feed ratio (C_2H_4 relative to CO) and reaction temperature to control the extent of CO insertion. Based on the

previously observed chemical O_2 gradient, our hypothesis here is that electricity and a nanowire array will allow us to spatiotemporally control the local concentration of CO and ultimately its incorporation into the polymer.

During my graduate career, I have shown that interfacing electrochemistry and nanomaterials with homogeneous catalysis can offer new insight into fundamental chemistry and push the boundaries of what was thought was possible with traditional organometallic chemistry. The utilization of electrochemically generated concentration gradients is a unique phenomenon that can provide an avenue to bypass inherent incompatibilities and enable novel reactivities.

The dissertation of Benjamin Seth Natinsky is approved.

Paula L. Diaconescu

Alexander M. Spokoyny

Paul S. Weiss

Chong Liu, Committee Chair

University of California, Los Angeles

2022

DEDICATION

I dedicate this thesis to my family: Howard and Stephanie Natinsky, my parents, and Jessica Natinsky, my sister. Thank you for being by my side, humoring me along the way, and for always giving me something to laugh about. I love you all.

Table of Contents

List of Figures

Chapter 2. Finding harmony among incompatibility in the ambient air oxidation of CH_4 to CH_3OH

Chapter 3. Uncovering the identity and the role of the terminal oxidant in the ambient air oxidation of CH_4 to CH_3OH

Chapter 4. Compartmentalization of O_2-sensitive Rh^{II} metalloradical within nanowire array electrode enables ambient CH_4 activation

Chapter 5. Polyketone from carbon dioxide and ethylene by integrating electrochemical and organometallic catalysis

List of Tables

Chapter 2. Finding harmony among incompatibility in the ambient air oxidation of CH_4 to CH_3OH

Acknowledgements

I would like to acknowledge my advisor and mentor Prof. Chong Liu for welcoming me into his lab and guiding me throughout my graduate student career. While working in the lab of Prof. Craig Hill at Emory University during my undergraduate education, I was experienced in the air- and water-free synthesis of inorganic complexes, however I had no prior skills in electrochemical characterization and materials synthesis. I was among the first class of graduate students that joined Prof. Liu's lab. As such, Prof. Chong Liu took the time to teach me such skills and embed me with his knowledge in the areas of electrochemistry and nanoscience.

The completion of my dissertation would not be possible without the other group members in Prof. Liu's lab. Prof. Liu has fostered an environment of collaboration and cooperation which showed through the group members' willingness to help and support each other, especially during trying times. I would like to especially thank Dr. Shengtao Lu, a postdoctoral researcher in Prof. Liu's lab during my first three years, for his guidance in electron microscopic techniques and finite element simulations. Whenever I came face to face with what felt like an insoluble problem, both Prof. Liu and Dr. Lu were ready to help problem solve. I would like to thank Brandon Jolly who was instrumental in developing an organometallic-based mathematical model for compartmentalization. In addition, Xun Guan, Jesus Iniguez, Benjamin Hoar, and Dr. Shuangning Xu all contributed to my growth as a graduate student and scientific researcher. David Dumas and Emma Copeland, both undergraduates at the University of California, Los Angeles during my graduate tenure, facilitated my projects through their synthetic work and electrochemical characterizations.

Without the necessary funding, I would not be able to perform research, so I would like to acknowledge UCLA for providing Teaching Assistant assignments. I would also like to thank

Chong for providing funding while I was a Graduate Student Researcher. And lastly, I would like to thank UCLA again for providing the funding for my final year through the Dissertation Year Fellowship.

I would like to thank Prof. Paula Diaconescu for her guidance and critical discussions in the realm of organometallic catalysis as well as being a member of my doctoral committee. In that vein, I would also like to thank Prof. Alex Spokoyny and Prof. Paul Weiss for their advice and support as my committee members over the course of my Ph.D.

Alongside research, I would like to thank my friends in the Chemistry and Biochemistry Department: Benjamin Hoar, Zachary Hern, Dr. Roselyn Rodrigues, and Dr. Mary Grumbles for their support outside of the laboratory. They were always there to laugh with (or at) me and encourage me through the toughest of times.

Outside of UCLA, I need to thank my friends (and roommates) Matthew Berns and Heather Monte. They were the first and last people I saw everyday which made working in the laboratory that much easier.

Lastly, I would not be where I am without my family. My dad, Howard Natinsky, my mom, Stephanie Natinsky, and my sister, Jessica Natinsky, were my foundation throughout this entire process. They were with me through the good and the bad. They lifted me up and put things in perspective when I could not do so myself.

Thank you to everyone. I would not be completing my dissertation and graduating with a Ph.D. in Chemistry without you in my life. I love you all.

VITA

EDUCATION

University of California, Los Angeles — **Los Angeles, CA**
Ph.D. Track Chemistry – Inorganic Concentration — Expected June 2022
M.S. Chemistry – Inorganic Concentration — March 2019
Advanced to Candidacy — September 2019

Emory University — **Atlanta GA**
Bachelor of Science: Chemistry, Minor in Spanish — May 2017

WORK EXPERIENCE

University of California, Los Angeles — **Los Angeles, CA**
Graduate Researcher, Department of Chemistry and Biochemistry — August 2017 – Present
Advisor: Chong Liu

- Designed electrocatalytic systems that interface electricity, nanomaterials and organometallic chemistry for small molecule functionalization, namely carbon-containing molecules such as methane and carbon dioxide
- Synthesized silicon nanowire arrays via a wet chemical etching technique with silver nitrate and hydrofluoric acid for electrocatalysis (with post-surface modification such as nanoparticle deposition and alterations of the terminal functional groups)
- Employed characterization techniques such as NMR (^{1}H, ^{13}C, or ^{31}P), ultraviolet-visible spectroscopy, infrared spectroscopy, gas chromatography, gas chromatography equipped with mass spectrometry, liquid chromatography equipped with mass spectrometry, scanning electron microscopy (equipped with electron dispersive spectroscopy) and cyclic voltammetry
- Honed skills in electrochemical measurements that utilize two and three-electrode setups, cyclic voltammetry, chronopotentiometry, chronoamperometry, linear sweep voltammetry, and electrochemical impedance spectroscopy
- Experienced in air- and water-free syntheses that employ glove box and/or Schlenk line techniques
- Proficient with high-pressure and high-temperature electrochemical experiments
- Presented and communicated project results at numerous scientific conferences as well as the general public
- Mentored undergraduate and graduate students in research techniques, lab etiquette, synthetic procedures, and characterization

University of California, Los Angeles — **Los Angeles, CA**
Graduate Teaching Assistant, Department of Chemistry and Biochemistry — August 2017 – June 2020
Advisors: Prof. Chong Liu, Dr. Pang, Dr. Casey, Dr. Russell

- Taught General and Organic Chemistry Laboratory I (14BL), General Chemistry and Organic Laboratory II (14CL), General Chemistry Laboratory (20L), Teaching College Chemistry (CHEM495), and Electrochemical Systems (C173/C273)

Center for Integrated Catalysis — **Los Angeles, CA**
Graduate Student Member, NSF-funded research collaboration — August 2020 – Present

- Integrated electrochemical reduction of CO_2 to CO and CO/ethylene copolymerization together

- Detected and quantified CO_2 reduction products (gas and liquid) via online gas chromatography and NMR
- Designed and set up high-pressure electrochemical reactor for integrated catalysis
- Optimized both the electrochemical and copolymerization reaction conditions for improved polymer synthesis
- Demonstrated the ability to work as part of a collaborative team with research groups from other institutions (Boston college, UNC-Chapel Hill, and University of Houston)

National Technology Energy Laboratory **Pittsburgh, PA**
Summer Fellow June 2021 – August 2021

- Selected as a summer fellow by the DOE to participate in the Energy Efficiency & Renewable Energy Storage Internship Program hosted at the NETL
- Conducted a comprehensive literature review regarding the application of fossil fuel resources to renewable energy storage systems (the conversion of coal and natural gas to support electrochemical and chemical storage systems)

Emory University **Atlanta, GA**
Undergraduate Research Assistant, Department of Chemistry August 2015 – May 2017
Advisor: Craig L. Hill

- Synthesized large anionic and air-sensitive polyoxometalate (POM) clusters on a Schlenk line and characterized them via infrared spectroscopy and solid-state NMR
- Performed alterations of the organic linker and counter cation exchange (tetrabutylammonium, lithium, and sodium)
  Conducted tests on the catalytic POM materials towards the hydrolysis of nerve agent analogs

AWARDS AND HONORS

(1) UCLA Graduate Dean's Scholar Award ($2000) *September 2017*
(2) UCLA ACS Research Showcase Fellowship ($500) *August 2019*
(3) Majeti-Alapati Fellowship ($3,250) *September 2019*
(4) Michael E. Jung Excellence in Teaching Award ($500) *May 2021*
(5) John Stauffer Excellence in Research Award ($500) *May 2021*
(6) Dissertation Year Fellowship *October 2021 – June 2022*

PUBLICATIONS

(1) **Natinsky, Benjamin S.**; Liu, Chong. Two are better than one. *Nature Chemistry* **2019**, *11*, 200-201.
(2) **Natinsky, Benjamin S.**; Lu, Shengtao; Copeland, Emma D.; Quintana, Jason C.; Liu, Chong. Solution Catalytic Cycle of Incompatible Steps for Ambient Air Oxidation of Methane to Methanol. *ACS Central Science* **2019**, *5*, 1584-1590 (Highlighted by *ACS Central Science* under "Control of Substrates Beyond the Active Site")
(3) **Natinsky, Benjamin S.**; Jolly, Brandon J.; Dumas, David M.; Liu, Chong. Efficacy Analysis of Compartmentalization for Ambient CH_4 Activation Mediated by Rh^{II} Metalloradical in Nanowire Array. *Chemical Science* **2021**, *12*, 1818-1825

Chapter 1. General Introduction

Motivation: Biological compartmentalization and concentration gradients

In biology, organisms have evolved to compartmentalize sequential reactions such that substrates and products are efficiently shuttled between localized enzymes.[1, 2] This ensures a high reaction throughput by successfully transporting reactive or transitory intermediates between successive catalytic sites.[3] Without such substrate channeling, ephemeral intermediates would most likely react elsewhere or be deactivated in the bulk solution, minimizing reaction turnover.[4, 5] For example, tryptophan synthase, which catalyzes the conversion of indole-3-glycerol-phosphate to indole and then to tryptophan, advantages substrate channeling of its intermediates, ensuring maximum reaction conversion.[6, 7] The subunits of the synthase enzyme create a hydrophobic channel which segregates the indole intermediate from the bulk solution and thus its free diffusion and participation in deactivating side reactions.[6, 7] Biological compartmentalization provides an avenue for which biology can manage such complex and intricate reaction mechanisms so as to circumvent competitive reactions and incompatibilities that would exist in a homogeneous solution.

Within the concept of compartmentalization, there can exist phenomena such as concentration gradients. In one instance, the rate of carbon dioxide (CO_2) fixation is enhanced due to spatial organization of the carboxysome microcompartments.[8, 9] These microcompartments create a high local concentration of CO_2 and exclude deactivating oxygen (O_2) to ensure the effective conversion of CO_2 to 3-phosphoglycerate by the O_2-sensitive ribose 1,5-bisphosphate carboxylase/oxygenase.[8, 9] Here, there exist concentration gradients with respect to the molecules of CO_2 and O_2; the local concentration of CO_2 within the carboxysome compartment is high

relative to the bulk concentration, whereas the concentration of O_2 is low in comparison. This prevents deactivation of the enzyme by O_2 and establishes high rates of reactivity. Based on such natural phenomena, the efforts presented in this dissertation are aimed at generating synthetic concentration gradients and microcompartments in order to mitigate unwanted side reactions and bypass reaction incompatibilities.

Precedence: Synthetic compartmentalization and concentration gradients

The integration of electrochemistry with nanomaterials can induce a synthetic concentration gradient and establish a compartmentalization effect. For example, the application of sufficient cathodic potential to an electrode in air will reduce O_2 at the electrode and establish a local anaerobic region near the surface of the electrode. This phenomenon is much more pronounced with the introduction of a porous or nanostructured electrode.[10, 11] Specifically, nanowire array electrodes have shown the ability to selectively control mass transport into, out of, and within the wire array domain.[12, 13] Previously, it was shown that a nanowire array electrode can render the local area within the wire array O_2-free (< 20 %) allowing anaerobic bacteria to fix CO_2 in air.[10] In this example, the nanowire electrode together with an applied potential create an anaerobic compartment within the wire array, allowing anaerobic bacteria to survive and thrive in air. The local O_2-free regime presented in this work motivated us to pursue other areas for which such a phenomenon can be applied, specifically in the realm of organometallic chemistry.

This work: Novel reactivity through the integration of electrochemistry, nanomaterials, and homogeneous organometallic catalysis

Homogeneous organometallic complexes offer high synthetic control through active site engineering, however they can suffer from air- or moisture-sensitivity, requiring the use of a glove

box or Schlenk line.[14–16] In the aforementioned system, a nanowire array working electrode was biased at a potential more negative than what was required to reduce O_2, establishing a local anaerobic region within the wire array compartment.[10] In a similar scenario, the air sensitivity of a catalyst was bypassed with gel networks that minimized O_2 diffusion in order to promote ambient C–C bond-formation via a photochemical pathway.[17] We sought to apply the synthetic pseudo "glove box" that is formed within the nanowire electrode system and observed in the gel network to reactions that typically require the use of inert atmospheres.

As a model system, rhodium porphyrin metalloradicals are known to stoichiometrically activate light alkanes, namely methane (CH_4), at room temperature and 1 bar pressure[18–20], but will react with O_2 at a faster rate[21], impeding C–H activation. We sought to exploit this system to catalytically convert CH_4 to methanol (CH_3OH) with O_2 as the terminal oxidant, but the O_2 sensitivity of the rhodium metalloradical posed a challenge. This motivated us to introduce a nanowire array electrode and electricity to this homogeneous organometallic reaction to resolve the undesirable reaction with O_2 and create a catalytic cycle of incompatible steps (**Chapter 2**). The reduction of O_2 at the electrode surface not only gave rise to an anaerobic domain in air but also generated the reactive oxygen species responsible for CH_3OH synthesis (**Chapter 3**). Moreover, the conversion of CH_4 to CH_3OH proceeded by successfully retaining the air-sensitive rhodium complex within the nanowire compartment, without which this reaction would be impossible (**Chapter 4**). Lastly, the spatiotemporal control we achieved with O_2 was applied to the electroreduction of CO_2 to carbon monoxide (CO). This electrochemical reduction reaction was integrated with the homogeneous copolymerization of CO and ethylene whereby the extent of CO insertion into the polymer was modulated by its electrochemical synthesis (**Chapter 5**).

References

(1) Shi, J.; Wu, Y.; Zhang, S.; Tian, Y.; Yang, D.; Jiang, Z. Bioinspired construction of multi-enzyme catalytic systems. *Chem. Soc. Rev.*, **2018**, *47*, 4295−4313.

(2) M. Vázquez-González, M.; Wang, C.; Willner, I. Biocatalytic cascades operating on macromolecular scaffolds and in confined environments, *Nat. Catal.*, **2020**, *3*, 256−273.

(3) Trantidou, T.; Friddin, M.; Elani , Y.; Brooks, N. J.; Law, R. V.; Seddon, J. M.; Ces, O. Engineering Compartmentalized Biomimetic Micro- and Nanocontainers, *ACS Nano*, 2017, **11** , 6549−6565

(4) Hurley, S. Spatial cell biology. Location, location, location. Introduction. *Science* **2009**, *326*, 1205.

(5) Avalos, J. L.; Fink, G. R.; Stephanopoulos, G. Compartmentalization of metabolic pathways in yeast mitochondria improves the production of branched chain alcohols. *Nat. Biotech.* **2013**, *31*, 335−341.

(6) Anderson, K. S.; Miles, E. W.; Johnson, K. A. Serine modulates substrate channeling in tryptophan synthase. A novel intersubunit triggering mechanism. *J. Biol. Chem.* 1991, *266*, 8020−8033.

(7) Chavan, K. S.; Barton, S. C. Simulation of Intermediate Channeling by Nanoscale Confinement. *J. Phys. Chem. C* **2018**, *122*, 14474−14480.

(8) Cannon, G. C.; Bradburne , C. E.; Aldrich, H. C.; Baker, S. H.; Heinhorst, S.; Shively, J. M. Microcompartments in Prokaryotes: Carboxysomes and Related Polyhedra. *Appl. Environ. Microbiol.*, 2001, 67 , 5351−5361.

(9) Rae, B. D.; Long, B. M.; Whitehead, L. F.; Förster, B.; Badger, M. R.; Price, G. D. Cyanobacterial Carboxysomes: Microcompartments that Facilitate CO_2 Fixation. *J. Mol. Microbiol. Biotechnol.*, 2013, 23 , 300−307.

(10) Liu, C.; Gallagher, J. J.; Sakimoto, K. K.; Nichols, E. M.; Chang, C. J.; Chang, M. C. Y.; Yang, P. Nanowire−Bacteria Hybrids for Unassisted Solar Carbon Dioxide Fixation to Value-Added Chemicals. *Nano Lett*. **2015**, *15*, 3634−3639.

(11) Newman, J. S.; Tobias, C. W. Theoretical Analysis of Current Distribution in Porous Electrodes. *J. Electrochem. Soc*. **1962**, *109*, 1183−1191.

(12) Liu, C.; Dasgupta, N. P.; Yang, P. Semiconductor Nanowires for Artificial Photosynthesis. *Chem. Mater.* **2014**, *26*, 415–422.

(13) Xiang, C.; Meng, A. C.; Lewis, N. S. Evaluation and optimization of mass transport of redox species in silicon microwire-array photoelectrodes. *Proc. Nat. Acad. Sci. U. S. A.* **2012**, *109*, 15622−15627.

(14) Thompson, S. J.; Brennan, M. R.; Lee, S. Y.; Dong, G. Synthesis and applications of rhodium porphyrin complexes. *Chem. Soc. Rev*. **2017**, *47*, 929–981.

(15) Brothers, P. J.; Collman, J. P. The organometallic chemistry of transition-metal porphyrin complexes *Acc. Chem. Res.* **1986**, *19*,, 209–215.

(16) Cui, W.; Wayland, B. B. Hydrocarbon C–H bond activation by rhodium porphyrins . *J. Porphyrins Phthalocyanines* **2004**, *8* , 103–110.

(17) Häring, M.; Abramov, A.; Okumura, K.; Ghosh, I.; König, B.; Yanai, N.; Kimizuka, N.; Díaz, D. D. Air-Sensitive Photoredox Catalysis Performed under Aerobic Conditions in Gel Networks. *J. Org. Chem.* **2018**, *83*, 7928–7938.

(18) Sherry, A. E.; Wayland, B. B. Metalloradical activation of methane. *J. Am. Chem. Soc.* **1990** , *112*, 1259 −1261.

(19) Wayland, B. B.; Ba, S.; Sherry, A. E. Activation of methane and toluene by rhodium(II) porphyrin complexes. *J. Am. Chem. Soc.* **1991**, *113*, 5305 −5311.

(20) Zhang, X.-X.; Wayland, B. B. Rhodium(II) Porphyrin Bimetalloradical Complexes: Preparation and Enhanced Reactivity with CH_4 and H_2. *J. Am. Chem. Soc*. **1994**, *116*, 7897−7898.

(21) Cui, W.; Wayland, B. B. Superoxo, Peroxo, and Hydroperoxo Complexes Formed from Reactions of Rhodium Porphyrins with Dioxygen: Thermodynamics and Kinetics. *J. Am. Chem. Soc.* **2006**, *128*, 10350−10351.

Chapter 2. Finding harmony among incompatibility in the ambient air oxidation of methane to methanol

This chapter is a version of Natinsky, B. S.; Lu, S., Copeland, E. D.; Quintana, J. C.; Liu, C. "A solution catalytic cycle of incompatible steps for ambient air oxidation of methane to methanol." *ACS Central Science*. **2019**, *5*, 1584–1590.

Abstract

Direct chemical synthesis from methane and air under ambient conditions is attractive yet challenging. Low-valent organometallic compounds are known to activate methane, but their electron-rich nature seems incompatible with O_2 and prevents a catalytic air oxidation. We report selective oxidation of methane to methanol with O_2-sensitive metalloradical as the catalyst and air as the oxidant at room temperature and ambient pressure. The incompatibility between C−H activation and O_2 oxidation is reconciled by electrochemistry and nanomaterials, with which a concentration gradient of O_2 within the nanowire array spatially segregated incompatible steps in the catalytic cycle. An unexpected 220,000-fold increase of the apparent reaction rate constants within the nanowire array leads to a turnover number up to 52,000 within 24 hours. The synergy between nanomaterials and organometallic chemistry warrants a new catalytic route for CH_4 functionalization.

Introduction

It is attractive to directly use air and natural gas, mostly methane (CH_4), as raw materials for the synthesis of methanol (CH_3OH)[1–4], an important commodity chemical. High-valent electron-deficient organometallic compounds have been attempted as the centers for C−H activation and

the immediate oxidants, presuming that the metal complexes can be re-oxidized by air to fulfill a catalytic cycle.[5–8] Due to the low reactivity of its C−H bond, CH_4 functionalization proceeds at elevated temperatures which incurs possible overoxidation into other products.[9–11] Alternatively, electron-rich organometallic compounds are capable of selectively activating CH_4 at low temperature.[2,4,12] This intrigues us to establish a hypothetical catalytical cycle at ambient condition, in which a reductive or homolytic step of CH_4 activation is followed by air oxidation to yield CH_3OH with minimal overoxidation. However, as the step of CH_4 activation may not be favored thermodynamically and O_2 can oxidatively quench the catalytic species (Figure 2.1A), external energy input is needed for catalyst regeneration and a spatial control of these incompatible reactions is required.

In biology, incompatible biochemical reactions co-exist within one organelle by localizing conflicting reactions. One example is the fixation of dinitrogen (N_2) in aerobic bacteria (Figure 2.1B). O_2-senstive nitrogenase for N_2 fixation is powered by the reducing equivalents generated from the tricarboxylic acid (TCA) cycle with O_2 as the terminal electron acceptor.[13] The tandem reactions of aerobic respiration and N_2 fixation is only possible with the buildup of a O_2 gradient, where the O_2-senstive nitrogenase is positioned in a local anaerobic part of cytoplasm and the TCA cycle in an aerobic one.[14] Inspired by the strategies employed in biology, we propose that in order to fulfill a catalytic cycle, the steps of C−H activation and air oxidation should be connected for the catalysis yet spatially separated with mitigated oxidative quenching (Figure 2.1C). While these requirements are challenging in a homogenous solution, we posit that they can be satisfied with the use of a nanowire array electrode and electrochemistry. When an electrode is biased at a potential more negative than the redox potentials of O_2 and the catalyst, redox-active catalysts can be regenerated by electrochemistry.[15] Moreover, the electrochemical reduction of O_2 will establish

a local O_2 gradient in the solution near the electrode surface. This effect is much more pronounced for nanomaterials and porous electrodes in general,[16,17] effectively creating an O_2-free domain within nanomaterials suitable for chemical steps incompatible with O_2. In support of this argument, our previous work demonstrated that a nanowire array electrode can create an O_2-free domain that allows anaerobic microbial reduction of CO_2.[16] Establishing a similar O_2 gradient and regenerating the CH_4-activating catalyst with electrochemically active nanowires (Figure 2.1C), here we report a catalytic cycle for ambient air oxidation of CH_4 to CH_3OH with O_2-sensitive, electron-rich Rh^{II} tetramesityl porphyrin metalloradical, (TMP)Rh^{II} (**1a**, Figure 2.2A), as the catalyst.[18,19,20]

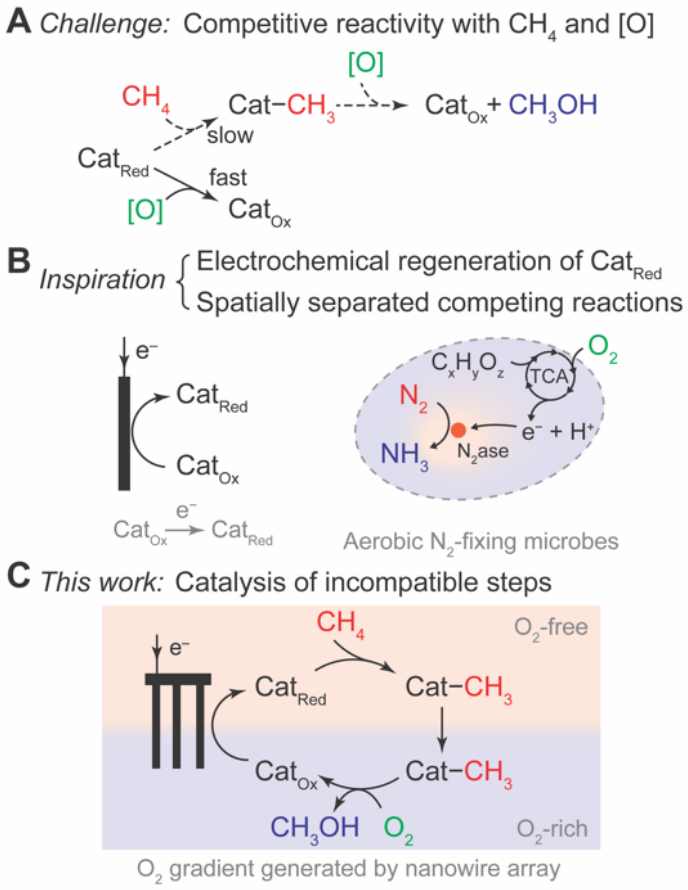

Figure 2.1. Motivation towards a catalytic cycle for ambient air oxidation of CH_4 to CH_3OH. (**A**) The incompatibility of low-valent electron-rich organometallic compounds for CH_4

functionalization with O_2-derived oxidants ([O]). (**B**) The inspirations to address such an incompatibility from examples in biology and (**C**) the proposed approach reported in this work.

Results and Discussion

At ambient conditions, two equivalents of **1a** reversibly activate one equivalent of CH_4 with a large equilibrium constant (K = 2.2×10^5 at 298 K), which yields the methylated and hydride species ((TMP)Rh−CH_3, **1b**; (TMP)Rh−H, **1c**, respectively) (Figure 2.2A).[19] The sterically bulky TMP ligand and the requirement of a four-centered transition state warrant a selectivity towards CH_4 by two orders of magnitude versus other larger substrates including CH_3OH.[21] However, in a homogenous solution, such a reactivity with CH_4 is not translatable to catalysis when paired with oxidants such as O_2. **1a** and O_2 react to form a Rh^{III} superoxo species under a fast equilibrium (K' = 8.4×10^3 at 298 K, Figure 2.2A),[22] and this reaction outcompetes the kinetically slow process of CH_4 activation ($k_{f,bulk}$ = 0.132 $M^{-2}\cdot s^{-1}$ at 296 K).[19] Despite this, we argue that electrochemistry can regenerate **1a** *in situ* from its oxidized counterparts thereby potentially allowing the activation of CH_4 with **1a** in air. Rh^{III} tetramesityl porphyrin iodide ((TMP)Rh−I, **1d**) was synthesized based on literature (Figure S2.1).[19] In argon (Ar) environment and non-coordinating solvent, 1,2-difluorobenzene (1,2-DFB),[23] with 0.1 M tetrabutylammonium perchlorate ($TBAClO_4$), a cyclic voltammogram (CV) of **1d** on a platinum (Pt) working electrode displays a quasi-reversible behavior at an electrode potential E_{appl} = −1.26 V vs. standard calomel electrode (SCE) (Figure 2B), consistent with a previous report that the Rh^{II} species can be regenerated by electrochemistry.[24,25] In the presence of O_2, a catalytic cathodic wave was observed on glassy carbon electrode preceding the Rh^{III}/Rh^{II} redox couple (E_{appl} < −0.7 V vs. SCE) (green trace in

Figure 2.2B), while the CV trace in the absence of **1d** yielded no such activity (Figure S2.2). Previous literature reports the generation of superoxide and peroxide as the immediate products both in solution or electrochemically when O_2 and Rh^{II} porphyrin are in stoichiometric ratio.[22,26,27] Here our experimental data in air suggest that additional catalytic irreversible reduction of O_2 is feasible when the amount of O_2 is in surplus.

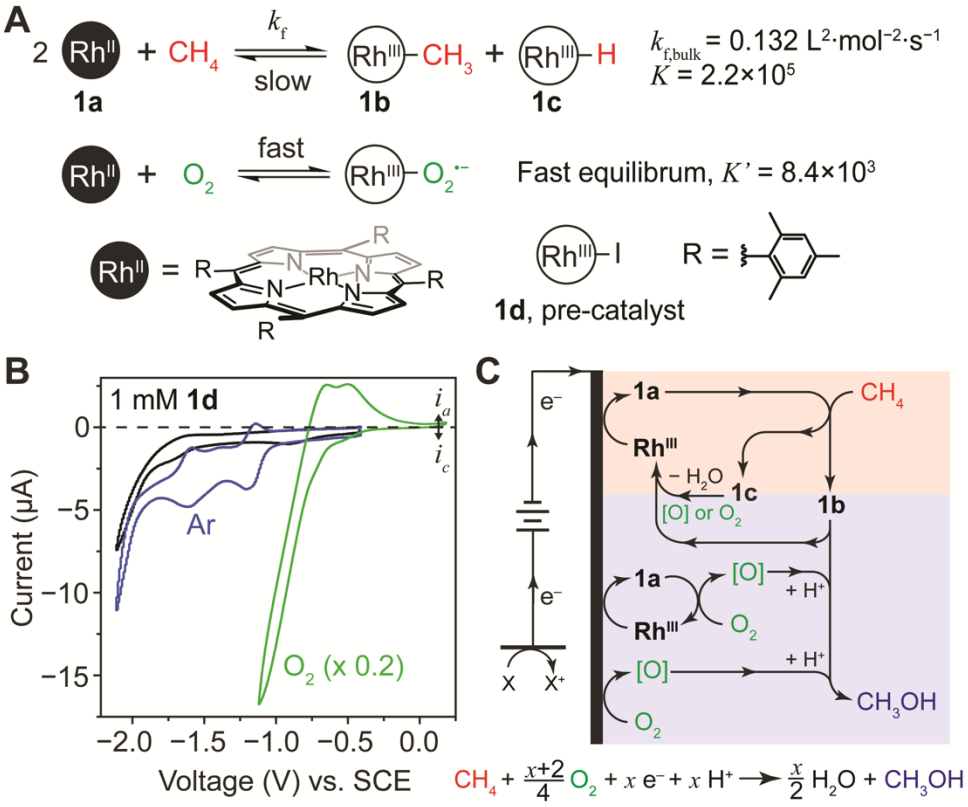

Figure 2.2. Electrochemical characterization and proposed catalytic cycle utilizing (TMP)Rh^{II}, **1a**, as the catalyst. (**A**) The reactivities of Rh^{II} metalloradical with CH_4 and O_2. (**B**) Cyclic voltammograms of 1 mM **1d** with 0.1 M $TBAClO_4$ in 1,2-DFB under Ar (blue) and air (green) environment. Black, blank solution without **1d**. 100 mV/s; Pt working electrode for blank and in Ar, glassy carbon electrode in O_2. The current in O_2 is multiplied by a factor of 0.2. (**C**) Schematic of the proposed catalytic cycle with **1d** as the pre-catalyst. Upon CH_3OH formation, Rh^{III} is generated whose charged is balanced by the perchlorate anion (ClO_4^-) in solution, which has been omitted for clarity. Oxidant [O] signifies reactive oxygen species such as hydrogen peroxide and

superoxide. The proposed cathodic reaction is displayed below the catalytic cycle. x = 2.1 on average based on experimental data (entries *2* to *6* in Table S2.1).

The capability of generating reaction oxygen species [O] electrochemically with Rh porphyrin lead us to explore whether those [O] can activate **1b** and yield CH_3OH. Stoichiometric reactions between different hydroperoxide species and **1b,** a stable compound prepared in air (Figure S2.3), were performed at a 1:1 ratio under ambient conditions (see Supplementary Information). The reaction between *t*-butyl hydroperoxide and **1b** were tracked via ^1H NMR and indicated the formation of CH_3OH at the expense of the methyl group in **1b** (Figure S2.4). This suggests that the methylated species **1b** is capable to release CH_3OH by hydroperoxide. Moreover, we found that a 3-hr electrolysis of **1b** at E_{appl} = −1.4 V vs. SCE yielded a stoichiometric amount of CH_3OH (Table S1, entry *1*). A gas chromatograph equipped with a mass spectrometer (GC-MS), allowing for a clear separation of electrolyte and catalyst from product determination, was used to detect the product after establishing a calibration curve (Figure S2.5). This indicates that the electrochemically generated [O] from O_2 reduction can be a serendipitous oxidant which yields CH_3OH after the step of CH_4 activation. During the aforementioned electrolysis, on average 2.3 equivalents of electrons are consumed per CH_3OH molecule synthesized, indicating that [O] is possibly of a hydroperoxide nature. However, not all of the generated [O] will lead to CH_3OH formation, conveying that the value of 2.3 electrons acts as an upper bound for the reaction during electrolysis.

Given the literature and our experimental data, we propose to establish a solution catalytic cycle of incompatible reactions at ambient conditions in air (Figure 2.2C), which is impossible in homogenous solution but potentially feasible when combining electrochemistry and

nanomaterials. A silicon (Si) nanowire array was proposed to offer a similar and even enhanced effect as that of a porous electrode with respect to induced concentration gradients.[16,17] By utilizing a nanowire array morphology as the working electrode in the presence of **1d** and O_2, oxidant [O] will be electrochemically generated *in situ* from O_2 with the creation of a O_2 gradient. The created O_2 gradient enables a nano-scopic separation of incompatible reaction steps. In a localized anaerobic environment near the base of the wire array (pink area in Figure 2.2C), electrochemically regenerated **1a** activates CH_4 and yields **1b**, which diffuses out and oxidatively hydroxylates to yield CH_3OH in the aerobic region (blue area in Figure 2.2C).

Numerical simulations based on electrochemistry models support the feasibility of the proposed catalytic cycle in the wire array. Finite-element simulations using the COMSOL Multiphysics program were conducted for different electrode geometries based on the experimentally available information (see Supplementary Information),[16,17] including the fast electrochemical equilibrium of Rh^{III}/Rh^{II} redox couple, the reported chemical reactivities,[19,22] and the molecular diffusion coefficients determined by diffusion ordered spectroscopy (DOSY) with ^1H nuclear magnetic resonance (NMR) (Figure S2.6). Figure 2.3A displays the calculated concentrations of **1a**, **1d** and O_2, denoted as [**1a**], [**1d**] and [O_2] respectively, versus the distance away from electrode surface (z) on a planar electrode at $E_{appl} = -1.4$ V vs. SCE. An anaerobic domain of predominantly CH_4-reactive **1a**, pink colored in Figure 2.3A, is minimal as compared to the extensive aerobic domain (light blue) where CH_4-unreactive **1d** is predominant. In contrast, for an exemplary wire array of 50 μm length, 4 μm diameter, and 15 μm periodicity (*i.e.* distance between adjacent wires) under the same condition, an extended anaerobic region is visible towards the base of the array and potentially favors CH_4 activation (Figure 2.3B). These results support our hypothesis that nanowire array electrode can spatially define an anaerobic region for CH_4 activation, which is

microscopically adjacent to an aerobic one ready for CH_3OH formation. Variation of the physical parameters such as the reactivities between O_2 and **1a** as well as the charge-transfer rate of O_2 reduction (Figure S2.7) does not alter the effectiveness of the wire array for establishing concentration gradients, indicating the robustness of this design.

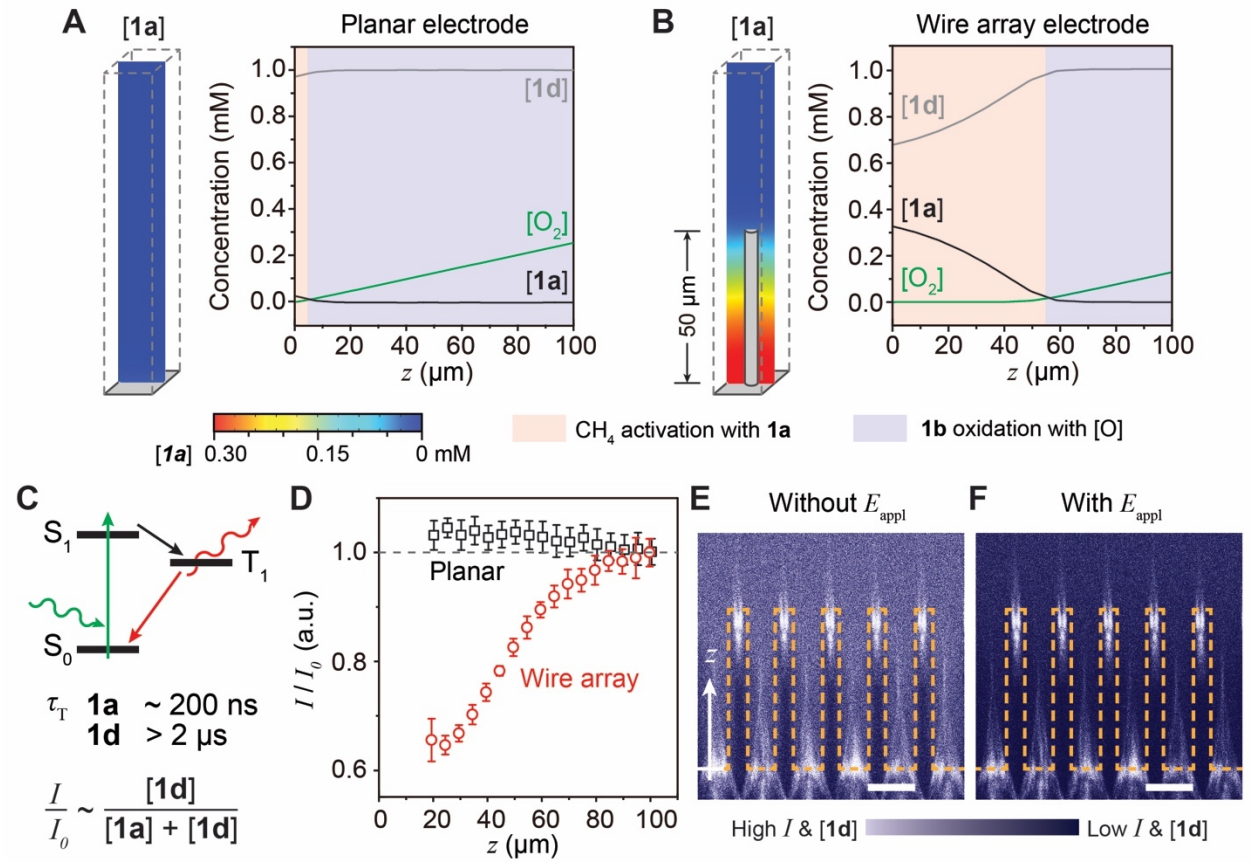

Figure 2.3. Numerical simulations and experimental validation of a microscopic concentration gradient for CH_4 activation. (**A**) and (**B**), simulated concentration gradients of O_2, **1a**, and **1d** ([O_2], [**1a**], and [**1d**], respectively) near a planar (**A**) and wire array (**B**) electrode. *z*, distance away from electrode surface; E_{appl} = −1.5 V vs. SCE. (**C**) Jablonski diagram illustrating potential phosphorescence emission of **1a** and **1d**. The triplet state lifetime (τ_T) of **1a** is much shorter than the one of **1d**. I/I_0, normalized emission intensity of phosphorescence. (**D**) experimentally determined I/I_0 versus *z* for planar (black) and wire array (red). 0.1 mM **1d** in the bulk solution, 0.1 M $TBAClO_4$ in 1,2-DFB, E_{appl} = −1.5 V vs. SCE. (**E**) and (**F**), the corresponding cross-

sectional heatmaps of unnormalized phosphorescence intensity without (**E**) and with (**F**) E_{appl}. The surface of Si wire array is delineated in yellow. Scale bar, 15 μm.

Spatially resolved optical measurements confirmed the predicted concentration gradients of **1a** and **1d** within the wire array electrode. The Si wire array, used as a model system, was prepared by reactive ion etching after photolithography (Figure S2.8).[28] The geometry was based on the same one used in the numerical simulation (Figure 2.3B) to help validate the conclusions drawn from the simulations. Electrochemical characterizations suggest that the prepared Si wire arrays are electrochemically active towards O_2 reduction with the presence of **1d** (Figure S2.9). As the lifetime of the excited triplet (τ_T) for **1d** (>2 μs) is much longer than the one of **1a** (~200 ns),[24] under optical excitation **1d** exhibits much stronger phosphorescence emission from 630 to 750 nm as compared to **1a** (Figure S2.10). Thus in a mixed solution containing both **1a** and **1d**, the local concentration percentage of **1d**, and subsequently the percentage of **1a**, can be tracked by monitoring the phosphorescence intensity after normalizing to the intensity when only **1d** is in the solution (I/I_0) (Figure 2.3C). An electrochemical setup was constructed under a confocal microscope with 526-nm excitation to *in situ* map the phosphorescence intensity near the electrode surface in air (Figure S2.11, see Supplementary Information). Figure 2.3D displays the values of I/I_0 at different z values for both planar (black) and wire array (red) Si electrodes when $E_{appl} = -1.5$ V vs. SCE. Near a planar electrode, the values of I/I_0 remain constant and it suggest that the local concentration of **1d** was not significantly perturbed (Figure 2.3D and S2.12). For a Si wire array (Figure S2.8) that possesses the exact same geometry simulated in Figure 2.3B,[28] the values of I/I_0 decrease towards the base of wire array, indicating a local depletion of **1d** and subsequently an accumulation of **1a**. The accumulation of CH_4-reactive **1a** is also suggested in the steady-state

cross-sectional heatmaps of phosphorescence. A distinguishably lower emission intensity profile was observed when E_{appl} = −1.5 V vs. SCE in the wire array (Figure 2.3E), as compared to the case at open-circuit condition (Figure 3F). The fidelity between simulation (Figure 2.3A and 2.3B) and experimental results (Figure 2.3E and 2.3F) confirms that wire array spatially generates an O_2-free domain in air with a localized accumulation of **1a**, which is reactive towards ambient CH_4 activation.

Selective ambient air oxidation of CH_4 to CH_3OH was observed with **1d** as the pre-catalyst when E_{appl} = −1.4 V vs. SCE on a Si wire array electrode. Si nanowire array, prepared by electroless wet etching with wire length of ~15 μm and diameter of ~100 nm (Figure 2.4A),[29] was applied as the working electrode for a three-electrode configuration in a customized electrochemical reactor (Figure S13). A gas mixture with a defined ratio between CH_4 and air (P_{CH4}/P_{air}) was delivered at a constant rate under ambient pressure. In a 1,2-DFB solution of 1 mM **1d** and P_{CH4}/P_{air} = 35, a 3-hr bulk electrolysis on a Si nanowire electrode (E_{appl} = −1.4 V vs. SCE) yielded 0.37±0.20 mM CH_3OH (n = 3, Figure 2.2B, Table S2.1, entry *2*). The observed CH_3OH can be directly attributed to the reactivity of **1a** and not the platinum (Pt) counter electrode as a similar performance is observed when graphitic carbon cloth is substituted as the counter electrode (Table S2.1, entry *3*). Longer electrolysis up to 24 hrs led to a higher concentration of CH_3OH up to 6.45±0.92 mM (Table S2.1, entries *4* to *6*). Since experimentally there were some fluctuation of electrochemical current as the electrolysis was conducted at a constant potential, a fairer comparison between experiments of different durations is based on the moles of CH_3OH normalized to the average electrochemical current. The CH_3OH yielded normalized by the current (n_{CH3OH}/I) is a near linear function of the electrolysis duration (Figure 2.4C), which suggests a continuous catalytic reaction without much catalyst degradation. On average, 2.1±0.3 equivalents of electrons, a value averaged

based on entries *2* to *6* in table S2.1, correspond to the formation of one equivalent of CH_3OH. The calculated value in the bulk electrolysis of **1d** in CH_4/air mixture is lower than the theoretical value of 4 should hydroperoxide be the only reactive oxygen species. This suggests that other reactive oxygen species other than hydroperoxide, such as superoxide, likely contribute to the oxidation of **1b** and the formation of CH_3OH. Interestingly, no other C_1 or C_2 liquid products were observed and the generation of CO or CO_2 was not detectable in the outgas by GC-MS (Figure S2.14). While overoxidation may pose an issue since **1a** is known to activate CH_3OH,[17] the absence of other products but CH_3OH formation in the electrolysis suggests a strong selectivity for CH_4, possibly due to the 100-time faster rate of CH_4 activation as compared to CH_3OH by **1a**,[21,30] as well as the relatively high solubility of CH_4 in the solvent (9.54 mM at 1-bar CH_4 based on ^{1}H-NMR).

Electrolysis in the absence of either **1d**, air or CH_4 led to the disappearance of CH_3OH formation (Table S2.1, entries *7* to *9*, respectively). Introducing ^{13}C-labelled CH_4 as the substrate in lieu of the one with natural ^{13}C abundance resulted in the surge of m/z = 33 peak in the mass spectrum (Figure 2.4D, Table S2.1, entry *10*). This suggests the formation of a $^{13}CH_3OH^{\bullet+}$ fragment in the spectrum from the yielded $^{13}CH_3OH$ (Figure S2.15). Our observations are consistent with a selective catalysis of CH_3OH formation with CH_4 as the substrate and O_2 as the oxidant. The turnover numbers (TON), defined as the ratio between product concentration and the concentration of pre-catalyst **1d** in solution, was calculated to be 0.37 for the 3-hr electrolysis and 6.45 for the 24-hr electrolysis (Figure 2.4E and Table S2.1). Such a definition of TON values obviates the fact that only the catalyst molecules within the nanowire array are responsible to CH_4 activation in our proposed mechanism. Therefore, we also calculated an alternative turnover number (TON'), which is defined as ratio between the moles of generated product and the moles of **1d** pre-catalyst within

the nanowire array. This TON' relevant to electrochemical catalysis[15] was found to be 2,972 for the 3-hr electrolysis and up to 51,807 for a 24-hr experiment (Figure 2.4E and Table S2.1). The calculated values of turnover numbers are comparable to those reported values of other catalysts for CH_4 functionalization (Tables S2.2 and S2.3), while our process is operating at room temperature and ambient pressure with air as the oxidant and CH_3OH as the product.

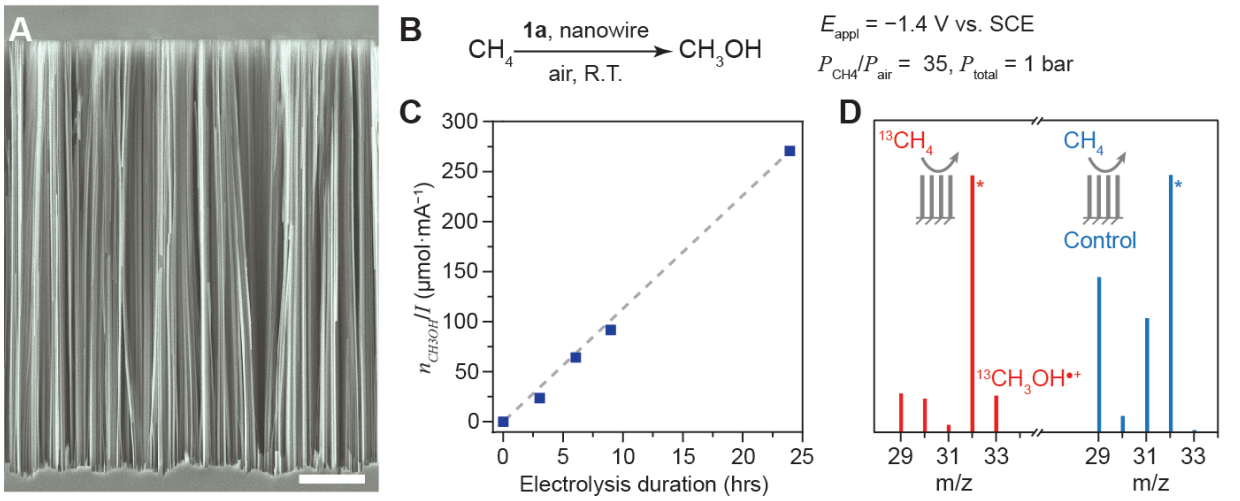

E	CH_4	C_2H_6	C_3H_8	$PhCH_3$
C−H BDE (kcal/mol)	105	101	101 (1°), 99 (2°)	88 (CH_3)
Product	CH_3OH	C_2H_5OH	OH (> 99%)	$PhCH_2OH$
TON (avg in solution)	0.37	1.49	0.32 (1°)	1.22
TON' (avg in array)	2972	11968	2570	9799
$k_{f,nano}$ ($L^2 \cdot mol^{-2} \cdot s^{-1}$)	2.9×10^4	9.3×10^3	1.0×10^3	9.1×10^3
$k_{f,bulk}$ ($L^2 \cdot mol^{-2} \cdot s^{-1}$)	0.132	–	–	0.0104

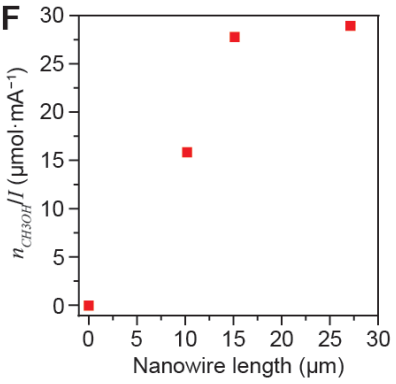

Figure 2.4. Ambient air oxidation of alkanes to primary alcohols enabled by nanomaterials and electrochemistry. (**A**) Si nanowire array imaged by scanning electron microscope. Scale bar, 2 μm. (**B**) General conditions used for catalytic ambient air CH_4 oxidation to CH_3OH. (**C**) The amount of generated CH_3OH normalized to the average electric current (n_{CH3OH}/I), as a function of the electrolysis duration. (**D**) Mass spectra for the electrolyte solution after 3-hr bulk electrolysis. Red, $^{13}CH_4$ as the substrate; blue, CH_4 of natural isotope abundance. (**E**) Catalytic reactivities for

different alkane substrates. BDE, bond dissociation energy; TON, turnover number based on catalyst in solution; TON', turnover number based on catalyst in reaction layer; $k_{f,nano}$ and $k_{f,bulk}$, kinetic rate constants of C−H activation by **1a** calculated in nanowire array and reported in literature[19], respectively. (**F**) The relationship between n_{CH3OH}/I in a 3-hr electrolysis and the lengths of nanowire array. A planar electrode was considered as an array of 0 μm wire length.

We further applied this ambient catalytic system to other substrates including ethane (C_2H_6), propane (C_3H_8) and toluene ($PhCH_3$). In all cases, selective oxidation to primary alcohols were observed (Table S2.1, entries *11* to *13*) and their corresponding TON and TON' are shown in Figure 4E. When *t*-butylbenzene was introduced as the substrate, no oxidation products were observed, which is in line with a previous report about the reactivity of Rh^{II} porphyrin species[31] (Table S2.1, entry *14*). The reaction kinetics for different substrates were also compared in the developed catalytic system. As catalytic reactions of different substrates were conducted under different substrate concentrations in solution, the observed kinetic rate constants other than the turnover numbers were employed for evaluation. Given that the step of C−H activation is shown to be turnover-limiting (vide infra), we calculated the rate constants of C−H activation in nanowire array, $k_{f,nano}$, based on the observed rate of alcohol accumulation (Figure 2.4E). Despite the large differences of bond dissociation energies (BDE) of the cleaved C−H bonds (Figure 2.4E), $k_{f,nano}$, which is independent of substrate concentration, appears to decrease even as BDE is simultaneously decreasing. Such a dependence of $k_{f,nano}$ over different substrates conveys the significant effect of steric constraint from **1a** as reported before.[18,19]

Electrochemically generated **1a** is the active species for CH_4 activation and the nanowire array is responsible for **1a**'s sustained presence and activity in air. We found that halving the concentration

of **1d** in bulk-electrolysis led to a decrease of reaction rate by 4.3 times (Table S2.1, entry *15*). This is consistent with the second-order kinetics on **1a** for CH_4 activation (Figure 2.2A) and implies that C−H activation is turnover-limiting in the proposed catalytic cycle (Figure 2.2A). When we substituted the pre-catalyst **1d** in the bulk electrolysis with a Rh^{III} octaethyl porphyrin iodide ((OEP)Rh−I, **2**) synthesized based on literature (Figure S2.16),[32] no CH_3OH was produced (Table S2.1, entry *16*). While **2** exhibits similar electrochemical response as **1d** with a slight shift of redox potential (Figure S17), the less bulky OEP supporting ligand is reported to favor the formation of $[(OEP)Rh^{II}]_2$ dimer, which is unreactive towards CH_4.[18] The observed difference of reactivities between **1d** and **2** as pre-catalysts suggests that it is the electrochemically generated **1a** that activates CH_4. Moreover, the catalytic ambient air oxidation of CH_4 to CH_3OH stopped and no CH_3OH was observed when the nanowire array electrode was replaced with a planar wireless electrode, a wire array with larger spacing among wires, or an increased O_2 partial pressure at P_{CH4}/P_{air} = 1 (Table S2.1, entry *17, 18,* and *19*, respectively). Such observations are indeed consistent with our simulation results that a higher concentration of O_2, planar wireless electrode, or a less dense nanowire array all mitigate the anaerobic domain, the population of **1a**, and thereby the reactivity towards CH_4 (Figure S2.18). On the other hand, a 3-hr electrolysis with P_{CH4}/P_{air} > 1000 yielded 0.25 mM CH_3OH (Table S2.1, entry *20*), illustrating the existence of a fine window of O_2 partial pressure which will result in optimal CH_3OH generation.

Along the same lines, the effect of nanowire length was also investigated to ascertain its role in catalysis and CH_3OH formation. Additional nanowire arrays of 10 and 27 μm in length were prepared (Figure S2.19). The yields of CH_3OH for a 3-hr electrolysis were 0, 0.19 (Table S2.1, entry *21*), 0.37, and 0.45 (Table S2.1, entry *22*) for a planar electrode and nanowires of 10, 15, and 27 μm, respectively. The corresponding n_{CH3OH}/I are plotted as a function of nanowire length in

Figure 2.4F. As the length of the nanowire increases, the anaerobic domain in which C–H activation occurs expands, resulting in accelerated catalysis and subsequently more CH_3OH formation. Such an increase of reaction rate plateaued between nanowires of 15 and 27 μm in length, suggesting that the system reached the intrinsic limit based on its mechanism and additional length of nanowire is not beneficial for reaction productivity any more. Last, a spent nanowire electrode, defined as a nanowire array that was previously utilized for a CH_3OH-yielding electrolysis, exhibited no activity towards CH_4 (Table S2.1, entry *23*) and measurement of X-ray photoelectron spectroscopy (Figure S2.20) found no residual Rh species on the nanowire's surface after electrolysis. It shows that the catalytic system is robust with minimal catalyst degradation and any possible Rh nanoparticle formation on the surface of the nanowires are not responsible for the observed reactivity.

Interestingly, the rate of CH_4 activation by **1a** was significantly increased in the nanowire array as compared to the one in bulk solution. $k_{f,nano} = 2.9\times10^4$ $L^2\cdot mol^{-2}\cdot s^{-1}$ for CH_4 activation, about 220,000 times the value in bulk solution ($k_{f,bulk} = 0.132$ $L^2\cdot mol^{-2}\cdot s^{-1}$).[19] A similar enhancement, by a factor of about 870,000, was observed when toluene was the substrate. As the C−H activation step of **1a** undergoes an entropically disfavored four-centered transition state,[18,19] high concentration and favorable orientation between two Rh centers will increase the reaction kinetics of CH_4 activation.[21] We speculated that the negative charges from the native oxide on Si nanowire's surface as well as the relatively low dielectric constant of 1,2-DFB[23] promote the adsorption of pre-catalyst **1d** near the nanowire's surface. This effect will lead to a high local concentration of **1a**, potentially create favorable intermolecular orientation between neighboring Rh centers, and subsequently increase its rate of CH_4 activation. Such a putative argument is supported by the observation that the rate of CH_3OH formation was minimal when the negative

charges on the Si surface were passivated with terminal trimethyl silyl groups[33] (Table S2.1, entry *24*). It implies that confining homogenous organometallic reactions within the space of nanowire array can accelerate the reaction rate significantly, an effect possibly similar to the one observed when an organometallic catalyst is encapsulated in a supramolecular cavity.[34]

Conclusion

Overall, the introduction of electrochemistry and nanomaterials enables a catalytic ambient air oxidation of CH_4 to CH_3OH with the use of a low-valent electron-rich organometallic compound that is otherwise unsuitable as a catalyst in a homogenous solution. The concept of spatially separating incompatible reaction steps at the nanoscale for a complete catalytic cycle provides new options for designing catalysis for a broad range of chemical transformations.

References

(1) Gunsalus, N. J.; Koppaka, A.; Park, S. H.; Bischof, S. M.; Hashiguchi, B. G.; Periana, A. R. Homogeneous Functionalization of Methane. *Chem. Rev.* **2017**, *117*, 8521−857.

(2) Labinger, J. A.; Bercaw, J. E. Understanding and exploiting C-H bond activation. *Nature* **2002**, *417*, 507−514.

(3) Caballero, A.; Perez, P. J. Methane as raw material in synthetic chemistry: the final frontier. *Chem. Soc. Rev.* **2013**, *42*, 8809−8820.

(4) Shilov, A. E.; Shul'pin, G. Activation and Catalytic Reactions of Saturated Hydrocarbons in the Presence of Metal Complexes. In *Activation of C-H Bonds by Low-Valent Metal Complexes ("The Organometallic Chemistry")*; Kluwer Academic Publishers, **2002**; pp 127–129.

(5) Periana, R. A.; Taube, D. J.; Evitt, E. R.; Loffler, D. G.; Wentrcek, P. R.; Voss, G.; Masuda, T. A Mercury-Catalyzed, High-Yield System for the Oxidation of Methane to Methanol. *Science* **1993**, *259*, 340−343.

(6) Periana, R. A.; Taube, D. J.; Gamble, S.; Taube, H.; Satoh, T.; Fujii, H. Platinum Catalysts for the High-Yield Oxidation of Methane to a Methanol Derivative. *Science* **1998**, *280*, 560−564.

(7) Jones, C.; Taube, D.; Ziatdinov, V. R.; Periana, R. A.; Nielson, R. J.; Oxgaard, J.; Goddard, W. A. Selective Oxidation of Methane to Methanol Catalyzed, with C−H Activation, by Homogeneous, Cationic Gold. *Angew. Chem. Int. Ed.* **2004**, *116*, 4726−4729.

(8) O'Reilly, M. E.; Kim, R. S.; Oh, S.; Surendranath, Y. Catalytic Methane Monofunctionalization by an Electrogenerated High-Valent Pd Intermediate. *ACS Cent. Sci.* **2017**, *3*, 1174−1179.

(9) Latimer, A. A.; Kakekhani, A.; Kulkarni, A. R.; Nørskov, J. K. Direct Methane to Methanol: The Selectivity–Conversion Limit and Design Strategies. *ACS Catal.* **2018**, *8*, 6894−6907.

(10) Schwarz, H. Chemistry with Methane: Concepts Rather than Recipes. *Angew. Chem. Int. Ed.* **2011**, *50*, 10096−10115.

(11) Labinger, J. A. Selective alkane oxidation: hot and cold approaches to a hot problem. *J. Mol. Catal. A: Chem.* **2004**, *220*, 27−35.

(12) Janowicz, A. H.; Kovac, C. A.; Periana-Pillai, R. A.; Buchanan, J. M.; Gilbert, T. M.; Bergman, R. G. Oxidative addition of soluble iridium and rhodium complexes to carbon-hydrogen bonds in methane and higher alkanes. *Pure Appl. Chem.* **1984**, *56*, 13−23.

(13) Dixon, R.; Kahn, D. Genetic regulation of biological nitrogen fixation. *Nat. Rev. Microbio.* **2004**, *2*, 621−631

(14) Tsoy, O. V.; Ravcheev, D. A.; Čuklina, J.; Gelfand, M. S., Nitrogen Fixation and Molecular Oxygen: Comparative Genomic Reconstruction of Transcription Regulation in Alphaproteobacteria. *Front. in Microbio.* **2016**, *7*, 1343.

(15) Savéant, J. M. Elements of Molecular and Biomolecular Electrochemistry: An Electrochemical Approach to Electron Transfer Chemistry. John Wiley & Sons, Inc., **2006**.

(16) Liu, C., *et al.* Nanowire–Bacteria Hybrids for Unassisted Solar Carbon Dioxide Fixation to Value-Added Chemicals. *Nano Lett.* **2015**, *15*, 3634−3639.

(17) Newman, J. S.; Tobias, C. W. Theoretical Analysis of Current Distribution in Porous Electrodes. *J. Electrochem. Soc.* **1962**, *109*, 1183−1191.

(18) Sherry, A. E.; Wayland, B. B.; Metalloradical activation of methane. *J. Am. Chem. Soc.* **1990**, *112*, 1259−1261.

(19) Wayland, B. B.; Ba, S.; Sherry, A. E. Activation of methane and toluene by rhodium(II) porphyrin complexes. *J. Am. Chem. Soc.* **1991**, *113*, 5305−5311.

(20) Thompson, S. J.; Brennan, M. R.; Lee, S. Y.; Dong, G. Synthesis and applications of rhodium porphyrin complexes. *Chem. Soc. Rev.*, **2018**, *47*, 929−981

(21) Zhang, X.-X.; Wayland, B. B. Rhodium(II) Porphyrin Bimetalloradical Complexes: Preparation and Enhanced Reactivity with CH_4 and H_2. *J. Am. Chem. Soc.* **1994**, *116*, 7897−7898.

(22) Cui, W.; Wayland, B. B. Superoxo, Peroxo, and Hydroperoxo Complexes Formed from Reactions of Rhodium Porphyrins with Dioxygen: Thermodynamics and Kinetics. *J. Am. Chem. Soc.* **2006**, *128*, 10350−10351.

(23) O'Toole, T. R.; Younathan, J. N.; Sullivan, B. P.; Meyer, J. T. 1,2-Difluorobenzene: a relatively inert and noncoordinating solvent for electrochemical studies on transition-metal complexes. *Inorg. Chem.* **1989**, *28*, 3923−3926.

(24) Vitols, S. E.; Friesen, D. A.; Williams, D. S.; Melamed, D.; Spiro, T. G. Excited State Dynamics of Rh(II) Tetramesityl Porphyrin Monomer from Nanosecond Transient Absorption and Emission Spectroscopy. *J. Phys. Chem.* **1996**, *100*, 207−213.

(25) Grass, V.; Lexa, D.; Momenteau, M.; Savéant, J.-M. Reductive Electrochemistry of Rhodium Porphyrins. Disproportionation of Intermediary Oxidation States. *J. Am. Chem. Soc.* **1997,** *119*, 3536−3542.

(26) Wayland, B. B.; Newman, A. R. Dioxygen and nitric oxide complexes of rhodium porphyrins. *Inorg. Chem.* **1981,** *20*, 3093−3097.

(27) Anderson, J. E.; Yao, C. L.; Kadish, K. M. Electroreduction of the dioxygen adduct of rhodium tetraphenylporphyrin: (TTP)Rh(O_2). *Inorg. Chem.* **1986,** *25*, 3224−3228

(28) Liu, C.; Tang, J.; Chen, H. M.; Liu, B.; Yang, P. A Fully Integrated Nanosystem of Semiconductor Nanowires for Direct Solar Water Splitting. *Nano Lett.* **2013**, *13*, 2989−2992.

(29) Huang, Z.; Geyer, N.; Werner, P.; de Boor, J.; Gösele, U. Metal-Assisted Chemical Etching of Silicon: A Review. *Adv. Mater.* 2011, *23*, 285−308.

(30) Cui, W.; Wayland, B. B. Activation of C−H / H−H Bonds by Rhodium(II) Porphyrin Bimetalloradicals. *J. Am. Chem. Soc.* **2004**, *126*, 8266-8274.

(31) Del Rossi, K. J.; Wayland, B. B. Formation and thermal reactions of rhodium-carbon bonds derived from the reactions of octaethylporphyrin-rhodium(III) dimer with alkyl carbon-hydrogen bonds in alkyl aromatics. *J. Am. Chem. Soc.* **1985**, *107*, 7941−7944.

(32) Collman, J. P.; Boulatov, R. Synthesis and Reactivity of Porphyrinatorhodium(II)−Triethylphosphine Adducts: The Role of PEt_3 in Stabilizing a Formal Rh(II) State. *J. Am. Chem. Soc.* **2000**, *122*, 11812−11821.

(33) Plummer, J. D.; Deal, M. D.; Griffin, P. B. Silicon VLSI Technology: Fundamentals, Practice and Modeling. Prentice Hall, Inc, **2000**.

(34) Fiedler, D.; Leung, D. H.; Bergman, R. G.; Raymond, K. N. Selective Molecular Recognition, C−H Bond Activation, and Catalysis in Nanoscale Reaction Vessels. *Acc. Chem. Res.* **2005**, *38*, 349−358.

Supplementary Information

Chemicals

Chemicals. The commercial reagents used in the various procedures were purchased from Sigma Aldrich, Alfa Aesar, Acros Organics, VWR and Fisher Chemicals unless otherwise noted; all chemicals were used as received unless specified. The deionized (DI) water that was used throughout the experiments came from a Millipore Milli-Q Water Purification System. The porphyrin ligands, protonated tetramesityl porphyrin (TMP)H_2 and protonated octaethyl porphyrin (OEP)H_2, were purchased from Frontier Scientific. 1,2-difluorobenzene (1,2-DFB) was purchased from Oakwood Chemical. The 1,2-DFB used in the glove box was distilled from CaH_2 and freeze-pump-thawed to remove residual O_2. The 1,2-DFB used in other experiments outside of the glove box was purified with activated 4 Å molecular sieves to remove residual moisture and methanol (CH_3OH) impurities. Tetrabutylammonium perchlorate ($TBAClO_4$), purified by recrystallization in ethanol (C_2H_5OH), was used as the electrolyte in all electrochemical measurements.

Chemical and materials characterizations. Spectra of one-dimensional proton nuclear magnetic resonance (^{1}H NMR) were recorded on a Bruker AV400 (400 MHz) spectrometer. The proton diffusion ordered spectroscopy (^{1}H DOSY) was performed on a Bruker AV300 (300 MHz) spectrometer. Chemical shifts for protons are reported in parts per million (ppm) and deuterated benzene (C_6D_6) and chloroform ($CDCl_3$) from Cambridge Isotope Laboratories were used as the locking solvents. ^{1}H NMR data are represented as follows: chemical shift, proton signal in molecule, multiplicity (s = singlet, d = doublet), coupling constants in Hertz (Hz), and integration. The mass spectral (MS) data were obtained on a Thermo Fisher Scientific Exactive series Direct Analysis in Real Time (DART) Mass Spectrometer. X-ray photoelectron spectroscopy (XPS) was measured on a Kratos Analytical AXIS Supra photoelectron spectrometer. The phosphorescence

intensity measurements were conducted on a Leica SP8 SMD confocal laser scanning microscope. A JEOL JSM-6700F Field Emission scanning electron microscope (SEM) and a Zeiss Supra 40VP SEM were used to image the silicon (Si) nanowire arrays.

Synthetic procedures

(TMP)Rh−I (**1d**). This synthesis follows the procedure published by Wayland et al.[19] The solvent in this procedure, 1,2-dichloroethane (1,2-DCE), was freeze-pumped prior to use. In a four-neck flask equipped with an addition funnel and a reflux condenser, 250 mg of di-μ-chloro-tetracarbonyldirhodium(I) ($Rh_2(CO)_4Cl_2$), kept under inert atmosphere, was dissolved in 40 mL of 1,2-DCE and then added drop wise under dinitrogen (N_2) to a suspension containing 375 mg of (TMP)H_2 and 300 mg of anhydrous sodium acetate (CH_3COONa) dissolved in 200 mL of 1,2-DCE. The resulting solution mixture was refluxed at 90 ºC under N_2 for 48 hrs. After cooling to room temperature, I_2 was added in two stages: 100 mg initially and then 80 mg after 2 hrs. The reaction mixture was stirred at room temperature for 3 hrs after the second addition of I_2. The crude product was filtered to remove any insoluble inorganic salts, concentrated by rotary evaporation, and chromatographed on alumina by using $CHCl_3$ as the eluent. ^{1}H NMR (C_6D_6) (Figure S2.1): 8.77 (pyrrole H, s, 8H), 2.31 (*o*-CH_3, s, 12 H), 1.69 (*o*'-CH_3, s, 12 H), 7.18 (*m*-H, s, 4 H), 6.98 (*m*'-H, s, 4 H), 2.39 (*p*-CH_3, s, 12 H). DART MS: m/z = 1010.

(TMP)Rh−CH₃ (**1b**). This synthesis follows the procedure published by Wayland et al.[19] In a round bottom flask equipped with a reflux condenser, 50 mg of (TMP)Rh−I was dissolved in 25 mL of C_2H_5OH and warmed to 60 ºC for 40 min. The resulting solution was filtered and the filtrate was flushed with N_2 for 30 min. 7 mg of sodium borohydride ($NaBH_4$) dissolved in 2 mL of aqueous 0.5 M sodium hydroxide (NaOH) was added to the solution under N_2 and was stirred for 30 min. Addition of 0.1 mL of methyl iodide (CH_3I) resulted in the formation of an orange/red precipitate,

which was collected via filtration. ^{1}H NMR (C_6D_6) (Figure S2.3): 8.69 (pyrrole H, s, 8 H), 2.20 (*o*-CH_3, s, 12 H), 1.68 (*o*'-CH_3, s, 12 H), 7.16 (*m*-H, s, 4 H), 7.03 (*m*'-H, s, 4 H), 2.39 (*p*-CH_3, s, 12 H), -5.31 (axial methyl, d, 3 H, 2.88 Hz). DART MS: m/z = 898.

(OEP)Rh−I (**2**). This synthesis follows the procedure published by Collman et, al.[32] Under N_2, 100 mg of (OEP)H_2 and 100 mg $Rh_2(CO)_4Cl_2$ were dissolved in 10 mL anhydrous dichloromethane (CH_2Cl_2). Then, 500 mg anhydrous CH_3COONa was added to the solution. Avoiding exposure to air, the stream of N_2 was adjusted such that the CH_2Cl_2 evaporated within 45 min. The resulting mixture was placed under vacuum for 10 min. This process of solvation with CH_2Cl_2, evaporation, and drying under vacuum was repeated. The resulting mixture was dissolved in 10 mL anhydrous C_6H_6 and, avoiding exposure to air, 100 mg I_2 was added. The reaction mixture was allowed to stir at room temperature for 20 min before the dry C_6H_6 was removed via rotary evaporation. The resulting mixture was chromatographed on silica by using CH_2Cl_2 as the eluent and then dried under vacuum. ^{1}H NMR ($CDCl_3$) (Figure S2.17): 10.28 (meso, s, 4 H), 4.19 (CH_2, m, 8 H, 6.5 Hz), 4.07 (CH_2, m, 8 H, 6.5 Hz), 1.96 (CH_3, t, 24 H, 6.5 Hz). DART MS: m/z = 763.

Si wire array. Si nanowire array applied in the bulk electrolysis was prepared following a modified electroless etching recipe based on the works by Huang et al.[29] A 4-inch, 500 μm thick, *p*-type boron-doped (100) Si wafer with an electrical resistivity of 0.01-0.02 Ω•cm (University Wafer, Inc.) was first sequentially rinsed with acetone, 2-propanol (IPA), and DI water, before being treated overnight in a piranha solution (3:1 H_2SO_4 (95-98%): H_2O_2 (30%)). The treated wafer was then etched in buffered HF (BHF) solution (10:1 NH_4F (40%):HF (49%)) to remove the native oxide, and exposed to O_2 plasma cleaning (Harrick Plasma, Plasma Cleaner PDC-32G) to remove organic residuals. The wafer was quickly transferred over to the etching solution ($AgNO_3$ and 5 M HF). To obtain nanowires of 15 μm length (Figure 2.4A), the wafer was etched for 3 hrs in 0.02

M $AgNO_3$ and 5 M HF. The duration of etching was minimized to 1 hr for nanowires of 10 μm in length (Figure S2.19A); 0.04 M $AgNO_3$ was utilized for a 3 hr etching process in order to prepare nanowires of 27 μm in length (Figure S2.19B) Afterward, 25% nitric acid (HNO_3) was added to dissolve the silver (Ag) deposited on the surface of the nanowires. Upon disposal of the HNO_3, the wafer was sequentially rinsed with DI water and acetone before drying. In the experiments of optical mapping of phosphoresce emission (Figure S2.8), Si wafer surface was patterned by photolithography with arrays of 4 μm-diameter dots of photoresist (AZ-5214-E) with 15 μm center-to-center distance between adjacent dots. Reactive ion etching was performed on the patterned wafer using a Versaline Fast DRIE system (Unaxis). After etching the remaining photoresist was removed using a Matrix-105 plasma asher (Matrix Integrated Systems). Before electrochemical testing, an ohmic contact between the Si electrode and a titanium foil was established with a combined use of Gallium-Indium eutectic, fast-drying Ag paint (Ted Pella, Inc.), and double-sided copper conductive tape (Ted Pella, Inc.). The passivation of residual negative charge on Si's surface was achieved by treating the electrode with the vapor of hexamethyldisilazane (HMDS) under slight vacuum, which allows the terminal surface Si−OH to react and yield $Si{-}O{-}Si(CH_3)_3$ moieties.[33] The electrode was used immediately for electrolysis after such a treatment.

Electrochemical characterizations

Cyclic voltammetry. Cyclic voltammograms were both performed inside a glove box under argon (Ar) and under atmospheric conditions with a Gamry Instruments Interface 1000-E potentiostat. All the solid chemicals used were dried under vacuum overnight prior to any testing. In a typical experimental condition, the electrolyte contains 0.1 M $TBAClO_4$ in 1,2-DFB, with a platinum (Pt) wire as the counter electrode and a Ag^+/Ag pseudo-reference electrode equipped with a glass frit.

A 2 mm diameter Pt working electrode was used in most cases. For electrochemical characterizations in air a 3 mm diameter glassy carbon working electrode was used to avoid the high reactivity of Pt with O_2 (Figure S2.2). Si wire array was also employed as the working electrode under Ar and in air in the presence of **1d** (Figure S2.9). The reported data are after *iR* correction. Cyclic voltammograms of decamethylferrocene were also conducted to calibrate the potentials of Ag^+/Ag pseudo-reference electrode, based on the reported standard potential of decamethylferrocene (−0.059 V vs. Saturated Calomel Electrode, SCE).[23]

Bulk electrolysis. The experiments of bulk electrolysis were performed using a Gamry Instruments Interface 1000-E potentiostat. A customized three-electrode electrochemical reactor with gas inlet/outlet ports was assembled as pictured in Figure S2.13. In a typical experiment, the electrochemical cell contains 0.1 M $TBAClO_4$ in 1,2-DFB, with a Pt wire as the counter electrode and a Ag^+/Ag pseudo-reference electrode with a glass frit. A mixture of CH_4 (Airgas, 99.5%) and house air were introduced into the reactor at a fixed ratio (P_{CH4}/P_{air}) under a constant flow rate with the use of mass flow controllers (Omega Engineering, Inc., Model: FMA5502A 0-10 sccm). The bulk electrolysis was conducted under a constant applied potential (E_{appl}) for varying durations. The procedures of *iR* correction and calibration of pseudo-reference electrode are similar as the ones in cyclic voltammetry. For the experiment of isotope labelling, bulk electrolysis was carried out with the same setup and procedure but with ^{13}C-labelled CH_4 (99 atom % ^{13}C, Sigma Aldrich). When needed, graphitic carbon cloth counter electrode was applied in place of the Pt wire counter (entry *3*, Table S1). Electrolysis with **1b** and flowing air was conducted in a three-electrode cell with glass carbon as the working electrode. When ethane (C_2H_6, 99%, Sigma Aldrich) and propane (C_3H_8, 98%, Sigma Aldrich) were introduced, the same setup and procedure

as previous bulk electrolysis experiments were applied. Toluene ($PhCH_3$) was added in a concentration of 10 mM and a mixture of N_2 (Airgas, 99.999%) and air was fed into the reactor.

Stoichiometric reactions with 1b

Stoichiometric reactions between **1b** and different hydroperoxide species were performed and monitored by ^{1}H NMR. In one example, 0.25 mM **1b** and 0.25 mM *t*-butyl hydroperoxide were mixed in 1,2-difluorobenzene (1,2-DFB) for 6 hrs at room temperature. The ^{1}H NMR spectra in C_6D_6 indicate the formation of CH_3OH at the expense of the axial methyl group of **1b** (shown below). Similar results were also obtained with cumene hydroperoxide in decane and 2-(1-hydroperoxy-1-methoxyethyl)-5-methylcyclohexan-1-ol in 1,2-DFB. The reaction between **1b** and *t*-butyl hydroperoxide is presented in Figure S2.4.

Product quantification

The products of CH_4 activation were quantified with a gas chromatograph equipped with a mass spectrometer (GC-MS, Agilent Technologies 5975 with Inert XL Selective Detector), owing to the interference of the $TBAClO_4$ electrolyte in the ^{1}H NMR spectra. A split/splitless injector was applied with a split ratio of 5:1 and a split flow of 5 mL/min. The instrument operated with an oven temperature of 50 ºC, an inlet temperature of 280 ºC, a column pressure of 16.08 psi, and a flow rate of 1.2 mL/min with helium carrier gas. A capillary HP-5MS column with 5% phenyl methyl siloxane (Model No.: 19091S-433, 30.0 m × 250 μm × 0.25 μm) was applied. The mass spectrometer had a source temperature of 230 ºC and a quadrupole temperature of 150 ºC. The injection volume was 1 μL and the injector was cleaned with $CHCl_3$ before and after each injection. For all analysis, samples were analyzed along with standards of known concentrations and the

concentration of product in the analyzed samples is calculated based on the concurrent calibration curve (Figure S2.5).

CH_3OH was quantified at a retention time of ~2.71 min by the intensity of the 31 m/z peak, due to the interference of O_2 at m/z = 32. The detection limit of CH_3OH was found to be ~10 μM. In the case that $^{13}CH_4$ was introduced, the concentration of $^{13}CH_3OH$ was monitored with the peak of m/z = 33. Formaldehyde (HCHO) was monitored at a m/z ratio of 29 and quantified at a retention time of ~2.43 min with a detection limit of ~100 μM. Formic acid (HCOOH) was monitored at a m/z ratio of 46 and quantified at a retention time of ~2.51 min with a detection limit of ~100 μM. C_2H_5OH was monitored at a m/z ratio of 45 and quantified at a retention time of ~2.65 min with a detection limit of ~100 μM. 1-propanol was monitored at a m/z ratio of 31 and quantified at a retention time of ~2.90 min with a detection limit of ~100 μM. 2-propanol was monitored at a m/z ratio of 45 and quantified at a retention time of ~2.70 min with a detection limit of ~100 μM. Potential gaseous products including carbon monoxide (CO) and carbon dioxide (CO_2) were monitored on the same GC-MS instrument with a modified recipe. 2-mL gas samples were taken before and during the electrolysis and were manually injected into the GC-MS. Since the instrument cannot differentiate the molecular ion peaks of CO and N_2, CO was monitored at the peak of m/z = 12. CO_2 was observed at its molecular ion peak of m/z = 44. Since CO_2 is present in the atmosphere, control samples were obtained to determine a baseline for the general CO_2 concentration. A calibration gas tank (Scott Mini-Mix) with 0.5 % CO, 0.5 % CO_2, 0.5 % O_2, and 0.5 % H_2 in N_2 was used to quantify the product. When $PhCH_3$ was used as the substrate, potential product benzyl alcohol was quantified by ^{1}H NMR. The peak at a chemical shift of ~4.4 ppm in C_6D_6 was integrated versus 1 mM internal standard tetramethylsilane. The concentration was determined based on an established calibration curve. Along the same lines, when *t*-butylbenzene

was introduced as the substrate, ^{1}H NMR was also utilized to monitor the reaction at a chemical shift of ~1.8 ppm in C_6D_6 versus internal standard tetramethylsilane (TMS).

Numerical simulation

Experimental preparation for numerical simulation. The diffusion coefficients of compounds were determined in diffusion ordered spectroscopy (DOSY) on the Bruker AV300 spectrometer. One-dimensional ^{1}H NMR spectra were taken prior to determine and optimize spectral width, acquisition time, and the receiver gain. The DOSY spectra were obtained with a diffusion time (Δ) of 50 ms, a diffusion gradient length (δ) of 1.5 ms, a recycle delay between scans of 2 s, and the maximum gradient was 50 gauss·cm^{-1}. The spectra are reported in log of diffusion coefficient ($m^2 \cdot s^{-1}$) versus chemical shift (ppm). The diffusion coefficients were found to be 5.62×10^{-10} $m^2 \cdot s^{-1}$ for **1d** (Figure S2.6) and 1.75×10^{-9} $m^2 \cdot s^{-1}$ for ferrocene (Fc). The thickness of the diffusion layer in the setup of bulk electrolysis was determined by measuring the steady-state oxidation current of electrolyte with 1 mM Fc under the same condition of bulk electrolysis. The model of diffusion layer and the Fick's law of diffusion dictate[36]:

$$(I_{Fc} - I_{blank}) = AnFD\frac{C}{L_D} \quad (1)$$

Here I_{Fc} and I_{blank} are the steady-state oxidation currents at the same oxidation potential with and without Fc, respectively; A is the area of the electrode; F is the Faraday's constant; n = 1; D = 1.75×10^{-9} $m^2 \cdot s^{-1}$ for Fc; C = 1 mM; and L_D is the thickness of diffusion layer. The thickness of diffusion layer was calculated to be about 375 μm. This determined thickness of diffusion layer sets the boundary of computational model in numerical simulation below.

Numerical simulation. The finite-element simulations of a three-dimensional microkinetic model[37] were performed using COMSOL Multiphysics (Ver. 5.3). Two electrode geometries were simulated: a nanowire array and a planar electrode. The nanowire array had a fixed length of 50 μm and a diameter of 4 μm. A periodic boundary condition was applied parallel along the electrode surface, featuring a square array of wires vertical to the surface. The boundary of simulation perpendicular to the electrode is set to be the thickness of diffusion layer, L_D (375 μm). Convection and migration are not considered in the model. The periodicity of the array, p, defines the distance between the geometric center of adjacent wires. In the case of Figures S2.8 and 2.3B, p was set to 15 μm to reflect the wire array prepared in Figure S2.8, whereas in Figure S2.18B and S2.18C, p was varied to 20 and 30 μm to test the efficacy of the generated O_2 concentration gradient. The concentrations of species at the boundary of the diffusion layer and the initial concentration in the simulation are considered to be the bulk concentration of each species. The initial condition of the system contains 1 mM (TMP)Rh^{III+} and 0.97 mM O_2, which is calculated based on the solubility of O_2 in C_6H_6 with a partial pressure of 0.1 atm.[38] However, in Figure S2.18D and S2.18E, we studied the effect of the concentration gradients as the initial concentration of O_2 is increased to 2 and 4 mM, respectively. Based on our reaction model, we consider two electrochemical reactions taking place at the electrode surface:

Reaction 1 (*rxn 1*): electrochemical reduction of (TMP)Rh^{III+} to (TMP)Rh^{II} (**1a**)

Reaction 2 (*rxn 2*): electrochemical reduction of O_2 that is catalyzed by Rh porphyrin species

and one homogenous reaction taking place in the electrolyte:

Reaction 3 (*rxn 3*): solution bimolecular reaction between **1a** and O_2 that also eventually leads to the consumption of O_2

Based on the experimental data shown in Figure 2.2B, we assumed the equilibrium redox potentials for the reduction of Rh^{III} and O_2 occur at −1.26 V (*rxn 1*) and –1.0 V (*rxn 2*) vs. SCE, respectively. Concentration-dependent Butler-Volmer equations were applied to account for the electrochemical reactions on the materials' surface. Correspondingly, each reaction had a defined exchange current density ($i_{0,Rh}$ and $i_{0,O2}$ ($mA \cdot cm^{-2}$)) and *rxn 3* was taken to be an elementary reaction with second-order kinetics with a kinetic rate constant named as k_{O2} ($L \cdot mol^{-1} \cdot s^{-1}$). $i_{0,Rh}$ was limited to 1×10^{-6} $mA \cdot cm^{-2}$ to ensure that the simulation could converge. In addition, the second-order kinetic rate constant of reaction between **1a** and O_2 (k_{O2}) is set to be 10^6 $L^1 \cdot mol^{-1} \cdot s^{-1}$ in simulation results shown in Figures 2.3A and 2.3B, and Figure S2.18. Figure S2.7 describes the modulation of the parameters $i_{0,O2}$ and k_{O2}, which cover 4 orders of magnitude, and the resulting concentration gradients that are induced. The diffusion coefficient for O_2 is set as 3.46×10^{-9} $m^2 \cdot s^{-1}$, the literature value of O_2 in C_6H_6.[39] The diffusion coefficient of $(TMP)Rh^{III+}$ as well as **1a** was set to be 5.62×10^{-10} m^2 $s^{-}1$, as determined experimentally using DOSY NMR.

***in situ* phosphorescence mapping**

An electrochemical setup with a microfluidic channel of about 200 μm thick (Figure S2.11) was constructed with a Pt wire used as the counter electrode and a Ag wire as the pseudo-reference electrode. The setup was mounted on the slide holder of a reverted confocal laser scanning microscope (Leica SP8 SMD). A 526 nm line of the white light laser was used as the excitation source and the phosphorescent emission between 570 – 750 nm was collected for confocal imaging with a 20 × 20 immersion type objective lens. The confocal scan works on the x-z-t mode at a spatial resolution of 146 nm/pixel, over an area of 150 μm × 150 μm *x-z* cross-section with a time-lapse of 0.361 frame s^{-1}.

Calculations of equivalent turnover numbers (TON and TON') and kinetic rate constants

Equivalent TON. The equivalent TON is defined as the number of product molecules generated per total catalyst in the system. The amount of active catalyst, **1a**, is taken as the amount of pre-catalyst, **1d**, added into the system. This approximation may significantly over-estimate the amount of active catalyst therefore the equivalent TON may be underestimated.

Equivalent TON'. The equivalent TON' is defined as the number of product molecules generated per catalyst molecule within the nanowire array. As the CH_4-reactive **1a** is only existent within the nanowire array due to the concentration gradient, we assume only the solution within the nanowire array are catalytically active. Furthermore, we approximate the bulk concentration of **1d** as the steady-state concentration of **1a** during catalysis. This approximation may over-estimate the amount of active catalyst therefore the equivalent TON' may be underestimated.

Kinetic rate constants of C−H activation. As the step of C−H activation was shown to be turnover-limiting in the proposed catalytic cycle, the kinetic rate constant of C−H activation in the wire array ($k_{f,nano}$) can be calculated based on rate of product accumulation in the catalysis. Moreover, assumptions of the active catalyst similar to the case of calculating TONs are made, which implies that the reported values of $k_{f,nano}$ may be underestimated. Last, experiments of ^{1}H NMR was used to determine the solubility of gaseous substrates under a certain partial pressure. The resultant concentrations of substrates at 1-atm partial pressure are: $[CH_4]$ = 9.54 mM, $[C_2H_6]$ = 119 mM, and $[C_3H_8]$ = 235 mM. Additionally, $[PhCH_3]$ = 10 mM as dictated by the experimental condition.

Supplementary Table 2.1. Experimental results of bulk electrolysis in this work.

Entry	Pre-catalyst	Duration (hrs)	Substrates	Gas composition [a]	Electrode	Product	[Product] (mM)	TON [b] Avg in solution	TON' [c] Avg in array
1	–	3	1 mM **1b**	N_2/air (35:1)	Glassy carbon	CH_3OH	1.30±0.36 [d]	–	–
2	1 mM **1d**	3	CH_4	CH_4/air (35:1)	15-µm Si NW	CH_3OH	0.37±0.20	0.37	2972
3 [e]	1 mM **1d**	3	CH_4	CH_4/air (35:1)	15-µm Si NW	CH_3OH	0.39	0.39	3133
4	1 mM **1d**	6	CH_4	CH_4/air (35:1)	15-µm Si NW	CH_3OH	0.92±0.06	0.92	7390
5	1 mM **1d**	9	CH_4	CH_4/air (35:1)	15-µm Si NW	CH_3OH	1.48±0.06	1.44	12771
6	1 mM **1d**	24	CH_4	CH_4/air (35:1)	15-µm Si NW	CH_3OH	6.45±0.92	6.45 [f]	51807 [f]
7	–	3	CH_4	CH_4/air (35:1)	15-µm Si NW	None	–	–	–
8	1 mM **1d**	3	CH_4	CH_4 in Ar [g]	15-µm Si NW	None	–	–	–
9	1 mM **1d**	3	–	N_2/air (35:1)	15-µm Si NW	None	–	–	–
10	1 mM **1d**	3	$^{13}CH_4$	$^{13}CH_4$/air (35:1)	15-µm Si NW	$^{13}CH_3OH$	0.46	0.46	3694
11	1 mM **1d**	3	C_2H_6	C_2H_6/air (29:1)	15-µm Si NW	C_2H_5OH	1.49	1.49	11968
12	1 mM **1d**	3	C_3H_8	C_3H_8/air (12:1)	15-µm Si NW	C_3H_7OH	0.32	0.32	2570
13	1 mM **1d**	3	10 mM $PhCH_3$	N_2/air (35:1)	15-µm Si NW	$PhCH_2OH$	1.22	1.22	9799
14	1 mM **1d**	3	10 mM *t*-butylbenzene	N_2/air (35:1)	15-µm Si NW	None	–	–	–
15	0.5 mM **1d**	6	CH_4	CH_4/air (35:1)	15-µm Si NW	CH_3OH	0.15±0.07	0.30	602
16	1 mM **2**	3	CH_4	CH_4/air (35:1)	15-µm Si NW	None	–	–	–
17	1 mM **1d**	3	CH_4	CH_4/air (35:1)	Si planar electrode	None	–	–	–
18	1 mM **1d**	3	CH_4	CH_4/air (35:1)	50-µm Si array [h]	None	–	–	–
19	1 mM **1d**	3	CH_4	CH_4/air (1:1)	15-µm Si NW	None	–	–	–
20	1 mM **1d**	3	CH_4	CH_4/air (>1000) [i]	15-µm Si NW	CH_3OH	0.25	0.25	2008
21	1 mM **1d**	3	CH_4	CH_4/air (35:1)	10-µm Si NW	CH_3OH	0.19	0.19	2289
22	1 mM **1d**	3	CH_4	CH_4/air (35:1)	27-µm Si NW	CH_3OH	0.45	0.45	1807
23	–	3	CH_4	CH_4/air (35:1)	"Spent" 15-µm Si NW [j]	None	–	–	–
24	1 mM **1d**	3	CH_4	CH_4/air (35:1)	Passivated 15 µm Si NW [k]	None	–	–	–

General conditions: 0.1 M $TBAClO_4$ in 1,2-DFB, E_{appl} = −1.4 V vs. SCE. The products are considered as "none" when the concentration of the potential products is below the instrument detection limit (~ 0.01 mM). NW, nanowire array. Error denotes SEM; n = 2 or 3 when errors were noted. [a] The value in the bracket is the ratio of partial pressure between the two gases, if applicable. When CH_4 and air were used, the ratio is denoted as P_{CH4}/P_{air} in the main text. [b] TON, turnover number, calculated as the concentration of CH_3OH divided by concentration of pre-catalyst **1d**. [c] TON' is calculated as the moles of generated CH_3OH divided by moles of pre-catalyst **1d** within the nanowire array. [d] Solvent evaporation during the bulk electrolysis leads to a slight over-estimation about the concentration of the yielded CH_3OH. [e] Plain carbon cloth was used as the counter electrode in place of a Pt wire. [f] Significant solvent evaporation was observed within 24 hrs. The values was calculated by taking this into account. [g] Conducted in an Ar glove box with the addition of 10 mM de-ionized water. [h] Si wire array, periodicity is 15-µm, length is 50-µm, and

diameter is 4-μm which is shown in Figure S2.12. [i] Trace atmospheric O_2 was used. [j] The electrode is a spent Si nanowire electrode that was used in a previous 3-hr bulk electrolysis at the same condition in entry *2* which yielded CH_3OH. [k] Si nanowire electrode was pre-treated with HMDS vapor before bulk electrolysis. The HMDS treatment passivates the negative charge on the Si's surface.

Supplementary Table 2.2. Reactivities of reported homogeneous catalysts for methane functionalization.

Catalyst	Liquid media	Temperature (°C)	P_{CH4} (psi)	Oxidant or reactant	Product	Yield (%)	Selectivity (%)	TOF [a] (hr^{-1})	TON [b]	Ref.
K_2PtCl_4	20% SO_3/H_2SO_4	215	943	SO_3	CH_3OSO_3H	–	98	24100	–	(*40*)
$Tl(TFA)_3$ [c]	$HTFA_{(l)}$ [c]/$CH_{4(g)}$	180	500	$Tl(TFA)_3$ [c]	CH_3TFA [c]	74	100	–	–	(*41*)
$PdSO_4$	96% H_2SO_4	180	400	SO_3	CH_3OH [d]	10 [e]	17	~3.6	18 [e]	(*42*)
$PdSO_4$ [f]	H_2SO_4	140	500	Echem [f]	– [g]	–	–	2000	–	(*8*)
$PdSO_4$ [h]	20% SO_3/H_2SO_4	70	500	Echem [h] & SO_3	CH_3OSO_3H & CH_3SO_3H	46 [i]	NA	–	~ 10	(*8*)
$HgSO_4$	100% H_2SO_4	180	500	SO_3	CH_3OSO_3H	43	85	~3.6	NA	(*5*)
$Au_2(SO_4)_3$	96 % H_2SO_4	180	390	H_2SeO_4	CH_3OSO_3H	NA	77	~3.6	32	(*7*)
(bpym)$PtCl_2$ [j]	10% SO_3/H_2SO_4	220	500	SO_3	CH_3OSO_3H	43	81	~36	>500	(*6, 43*)
Ir(COD)Cl/dmpe [k]	Cyclohexane	150	500	B_2pin_2 [l]	CH_3Bpin [m]	~52	–	~6.5	104	(*44*)
Cp^*_2ScMe [o]	Cyclohexane	80	– [p]	$CH_3CH=CH_2$	$(CH_3)_3CH$	–	–	0.04	–	(*45*)
bis(NHC)$PdBr_2$ [q]	HTFA [c]	90	435	$K_2S_2O_8$	CH_3TFA [c]	–	–	2.4	–	(*46*)
$Ce(OTf)_4$ [r]	CH_3CN	25	725	CCl_3CH_2OH	Aryl and alkyl derivatives	29	NA	NA	2900	(*47*)
$RhCl_3$–NaCl–KI [s]	$H_2O_{(l)}/CF_3COOH_{(l)}$	95	870	H_2O_2/HOI [t]	C_1 [v]	–	–	[w]	–	(*48*)
Cu_3Etppz [x]	$H_2O_{(l)}$, $H_2O_{2(l)}$ [y]	25	14.5	O_2	CH_3OH	–	–	–	6.5	(*49*)

[a] TOF, turnover frequency. [b] TON, turnover number. [c] TFA, trifluoroacetate. [d] Obtained after hydrolysis from the immediate product, CH_3OSO_3H. [e] Total amount of CH_4 reacted. [f] Electrochemically generated high-valency Pd dimer during cyclic voltammetry. [g] Proposed yet not confirmed in this specific experiment. [j] Electrochemically generated high-valency Pd dimer during bulk electrolysis in the presence of CH_4. [j] bpym, bipyrimidine. [k] COD, 1,5-cyclooctadiene; dmpe, 1,2-bis(dimethylphosphino)ethane. [l] B_2pin_2, **4,4,4′,4′,5,5,5′,5′-Octamethyl-2,2′-bi-1,3,2-dioxaborolane**. [m] CH_3Bpin, 2,4,4,5,5-pentamethyl-1,3,2-dioxaborolane. [o] Cp^*, cyclopentadiene. [p] Not reported. [q] NHC, N-Heterocyclic carbenes. [r] Photocatalytic system; OTf, trifluoromethanesulfonate. [s] Represents starting materials in solution. [t] O_2 and CO are bubbled in and facilitate generation of peroxide species. [u] Proposed oxidants generated in solution. [v] CH_3OH and CF_3COOH, CH_3COOH, HCOOH, and CO_2 were all observed. [w] 71, 9, 12, and 1300 corresponding to CH_3OH and CF_3COOH (combined), CH_3COOH, HCOOH, and CO_2, respectively. [x] Cu_3Etppz, 3,30 -(1,4-diazepane1,4-diyl)bis[1-(4-ethylpiperazine-1-yl)propan-2-ol]). [y] H_2O_2 is added at 20 equivalents to regenerate the catalyst.

Supplementary Table 2.3. Reactivities of reported heterogeneous catalysts for methane functionalization.

Catalyst	Solvent/phase	T (°C)	P_{CH4} (psi)	Oxidant	Product	Yield (%)	Selectivity (%)	TOF [a] (hr^{-1})	TON [b]	Ref.
AuPd NP [c]	$H_2O_{(l)}$	50	435	O_2/H_2O_2	CH_3OH	–	92	–	–	(*50*)
Cu-zeolite	$He_{(g)}$ or $O_{2(g)}$, $CH_{4(g)}$, $H_2O_{(g)}$ [d]	400, 200 [d]	102	H_2O	CH_3OH	–	~97	–	0.204 [e]	(*51*)
Ga_2O_3/MoO_3	$CH_{4(g)}/He_{(g)}/O_{2(g)}$	455	334	O_2	CH_3OH	66	22	–	–	(*52*)
ZSM-5	$H_2O_{(l)}$	50	442	H_2O_2	CH_3OH	–	12	6320	>3000	(*53*)
Cu-ZSM-5	$H_2O_{(l)}$	50	442	H_2O_2	CH_3OH	–	83	2113	>1057	(*53*)
Fe-silicalite-1	$H_2O_{(l)}$	70	43.5	H_2O_2	CH_3OH	–	93	70	>35	(*53*)
Fe-ZSM-5	$CH_{4(g)}/N_2O_{(g)}$	160	<1	N_2O	CH_3OH	70	76	–	3.6 [f]	(*54*)
FeO_x/TiO_x [g]	$CH_{4(g)}$	25	14.5	H_2O_2	CH_3OH	97	90	–	18	(*55*)
Cu-MOF-808	$N_2O_{(g)}$ /$He_{(g)}$, $CH_{4(g)}$ $He_{(g)}/H_2O_{(g)}$ [h]	150	14.5	N_2O	CH_3OH	–	–	–	71.8 [i]	(*56*)
FeN_4 in graphene [j]	$H_2O_{(l)}/CH_{4(g)}$	25	290	H_2O_2	C_1 [k]	–	–	0.47	–	(*57*)
Cu-Fe-ZSM-5	$CH_{4(g)}/N_2O_{(g)}$	342	14.5	N_2O	CH_3OH	–	78	–	–	(*58, 59*)
Rh-ZSM-5 [l]	$CH_{4(g)}/CO_{(g)}/O_{2(g)}$	150	290	O_2	$C_{1,2}$ [m]	–	–	–	[n]	(*60*)
CuEtp@AlMSN30-ex [o]	$CH_{4(g)}/H_2O_{(l)}$, $H_2O_{2(l)}$ [p]	25	14.5	O_2	CH_3OH	–	–	–	171.2	(*61*)
CZ-12–0.58 [q]	$O_{2(g)}$, $He_{(g)}$, $CH_{4(g)}$ [r]	170	14.5	O_2	CH_3OH	–	98	–	8.2 [s]	(*62*)
Cu-MOR	$O_{2(g)}$, $CH_{4(g)}$, $H_2O_{(l)}$ [t]	200	14.5	O_2	$C_{1,2}$ [u]	–	–	–	160 [v]	(*63*)
FeZSM-5	$O_{2(g)}$, $N_2O_{(g)}$ [w], $CH_{4(g)}$,	25	14.5	N_2O	$C_{1,2}$ [u]	70 [x]	–	–	–	(*64*)
Co-ZSM-5-*at*-1-20 [y]	$O_{2(g)}/CH_{4(g)}$ [z]	150	14.5	O_2	C_1 [aa]	–	75	–	2.25 [bb]	(*65*)
Cu-H-ZSM-5 [cc]	$O_{2(g)}/CH_{4(g)}/H_2O_{(g)}$	210	14.2	O_2	C_1 [dd]	–	–	–	82 [ee]	(*66*)
Cu-Na-ZSM-5 [cc, ff]	$O_{2(g)}/CH_{4(g)}/H_2O_{(g)}$	210	14.2	O_2	C_1 [dd]	–	71	–	37 [gg]	(*66*)
Ni-ZSM5 [hh]	$O_{2(g)}/CH_{4(g)}/H_2O_{(g)}$	175	14.5	O_2	$C_{1,2}$ [ii]	–	–	–	5.1 [jj]	(*67*)

[a] TOF, turnover frequency. [b] TON, turnover number. [c] AuPd nanoparticles supported on polyvynil pyridine. [d] Cyclic operation. [e] Moles of CH_3OH per mole of Cu in zeolite. [f] Quasicatalytic due to insufficient temperatures for desorption [g] Photocatalysis under 1-sun illumination. [h] The catalyst was pretreated with 3 % N_2O in He for 2 hrs (150 °C), purged with He for 30 min, exposed to CH_4 for 1 hr (150 °C), and introduced to 3 % steam in He (150 °C) to desorb CH_3OH. [i] Moles of CH_3OH per mole of Cu in MOF. [j] Single Fe atom sites confined in graphene [k] CH_3OH, CH_3OOH, $HOCH_2OOH$, and HCOOH were all observed. [l] Rh-ZSM-5 is pretreated with 5 % H_2 at 550 °C for 3 hrs. [m] CH_3OH, CH_3COOH, HCOOH, and CO_2 were all observed. [n] 2068, 21295, 7020, and 5010 corresponding to μmol product per gram catalyst for CH_3OH, CH_3COOH, HCOOH, and CO_2, respectively. [o] CuEtp, $Cu^ICu^ICu^I$(3,3-(1,4-diazepane1,4-diyl)bis[1-(4-ethylpiperazine-1-yl)propan-2-ol]), stabilized on pore-expanded mesoporous silica nanoparticles with Al-doping (Si/Al ratio = 30). [p] H_2O_2 is added at 200 equivalents to regenerate the catalyst. [q] CZ-12–0.58, Cu-ZSM-5 with Si/Al ratio = 12 and Cu/Al ratio = 0.58. [r] CZ-12–0.58 is pretreated with O_2 at 450 °C,

cooled to room temperature, flushed with He, and CH_4 was passed over as the temperature was increased to 170 °C. [s] Corresponds to μmol CH_3OH per gram CZ-12–0.58. [t] Catalyst is pretreated with O_2 at 450 °C, reacted with CH_4, and purged with H_2O to desorb product. [u] Dimethyl ether and CH_3OH were both observed. [v] Corresponds to μmol product, dimethyl ether and CH_3OH, per gram Cu-MOR. [w] FeZSM-5 was pretreated with O_2 at 550 °C, then heated to 900 °C under vacuum, and finally treated with N_2O at 230 °C prior to use. [x] CH_3OH was extracted with ethanol for multiple cycles [x] Sample was treated with NaOH, where 1 signifies the [NaOH] and 20 the reaction time in mins. [z] Catalyst was exposed to O_2 and CH_4 and then treated with ethanol to recover the products. [aa] CH_3OH and HCOOH were both observed. [bb] Corresponds to μmol of CH_3OH per gram Co-ZSM-5-*at*-1-20 and was estimated from a bar graph. [cc] Catalyst is pretreated for 5 hrs at 550 °C with flowing O_2, cooled to 210 °C under O_2 flow and then purged under He for 0.5 hrs. Cu/Al = 0.31. [dd] Both CH_3OH and CO_2 were observed. [ee] μmol of CH_3OH per gram Cu-H-ZSM-5. [ff] Cu/Al = 0.37, Na/Al = 0.26. [gg] μmol of CH_3OH per gram Cu-Na-ZSM-5 [hh] 5 wt % Ni on ZSM5. The catalyst is activated at 650 °C with pure O_2 for 3 hrs. Ni/Al = 1. [ii] CH_3OH, HCOOH, and $HOCH_2CH_2OH$ were all observed as products. [jj] μmol of CH_3OH per gram Ni-ZSM5.

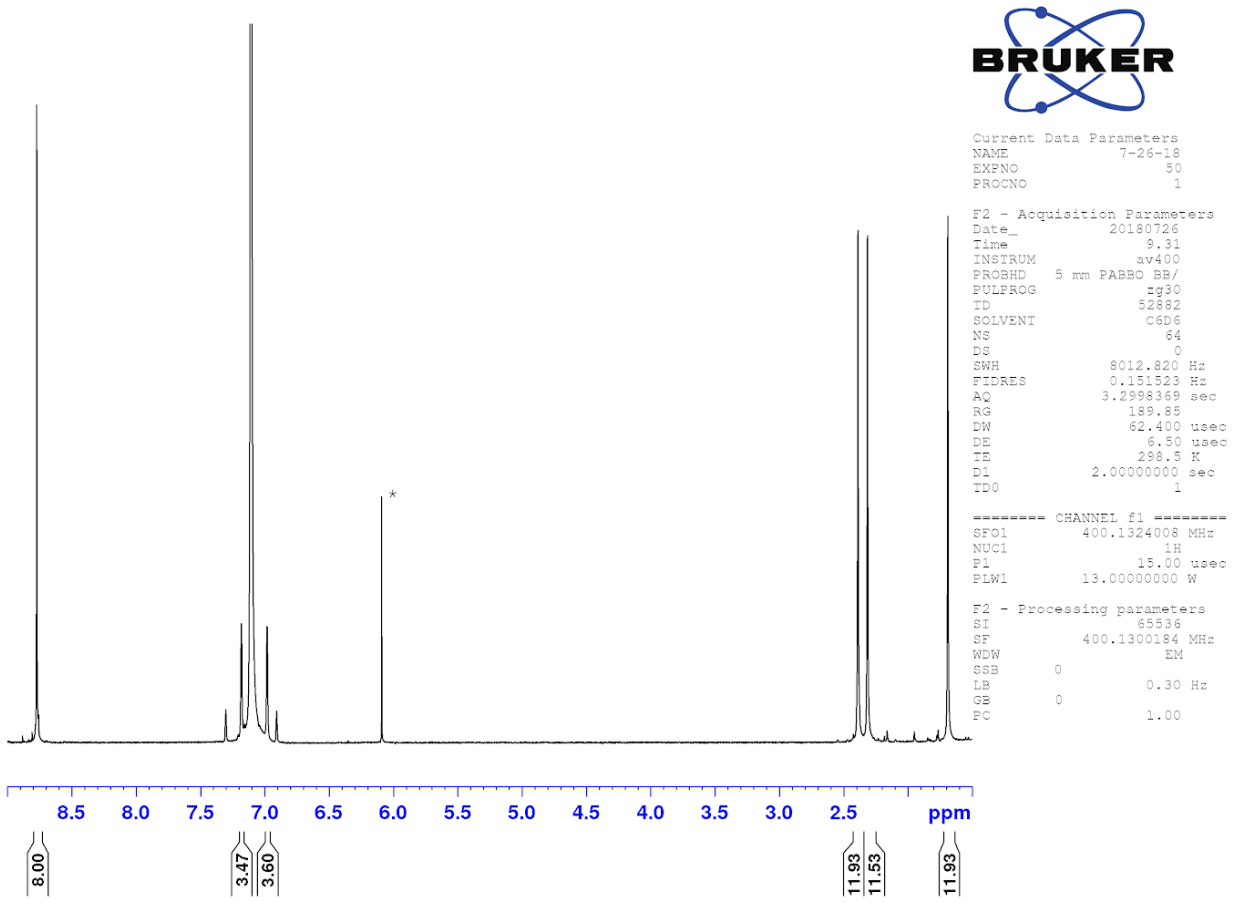

Figure S2.1. ^{1}H NMR spectrum of **1d** in C_6D_6. All integrations are referenced to the peak at 8.77 ppm. The solvent peak, C_6D_6, appears at 7.09 ppm. The marked * peak is due to residual $CHCl_3$.

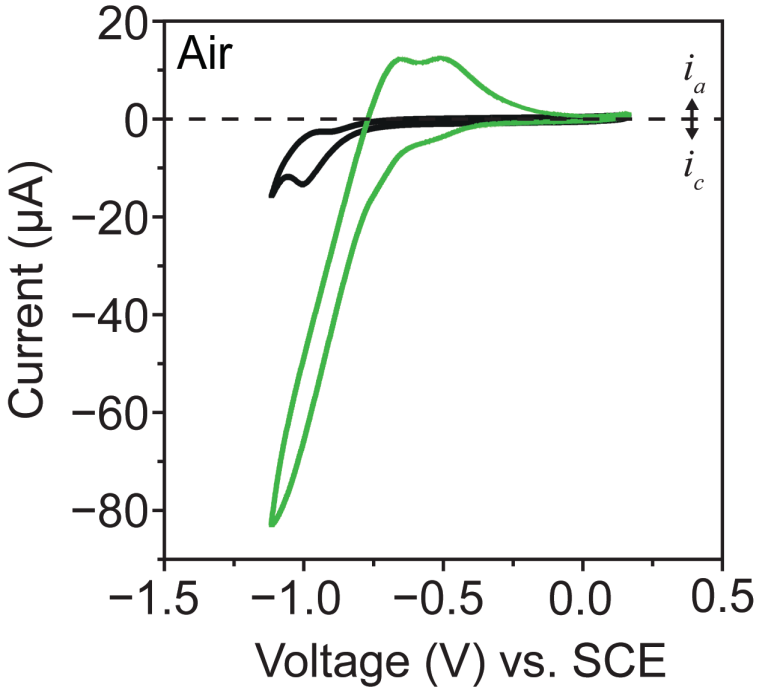

Figure S2.2. Cyclic voltammograms on glassy carbon electrodes in ambient air. Black trace, blank without the addition of **1d**; green trace, 1 mM **1d**. 0.1 M $TBAClO_4$ in 1,2-DFB, 100 mV/s.

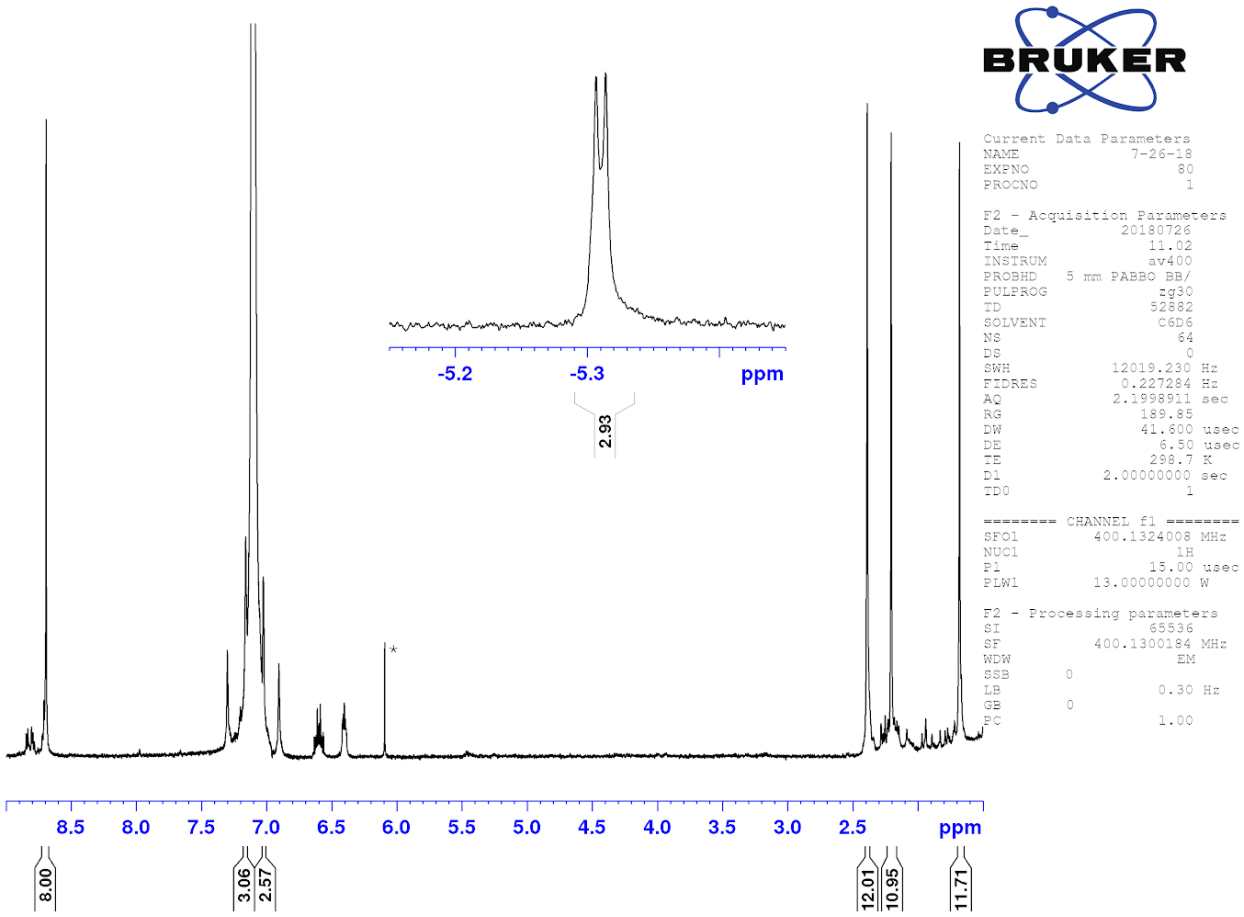

Figure S2.3. ^{1}H NMR spectrum of **1b** in C_6D_6. All integrations are referenced to the peak at 8.69 ppm. The solvent peak, C_6D_6, appears at 7.10 ppm. The marked * peak is due to residual $CHCl_3$.

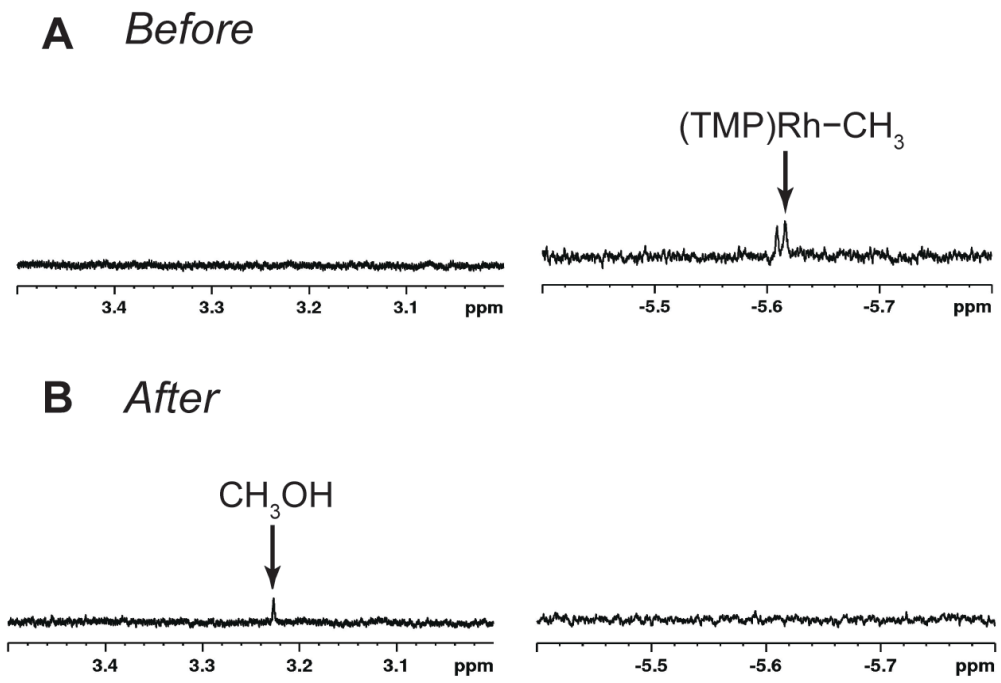

Figure S2.4. ^{1}H NMR spectra of **1b** with *t*-butyl hydroperoxide (**A**) upon mixing and (**B**) after 6 h at ambient conditions. Solvent: 80% 1,2-DFB and 20% C_6D_6. TMS was added as the internal reference after the reaction.

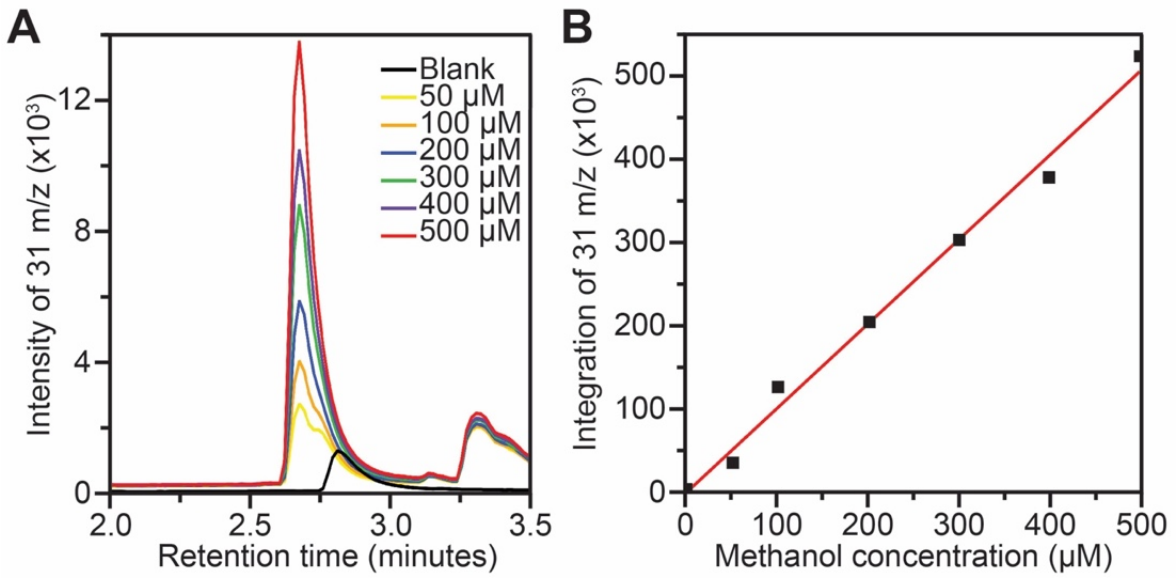

Figure S2.5. (**A**) a gas chromatograph spectrum monitoring a m/z ratio of 31 with varying concentrations of CH_3OH. The observed retention time is at about 2.62 min. (**B**) calibration curve of CH_3OH concentration and its corresponding integration of the 31 m/z on the chromatograph at the abovementioned retention time.

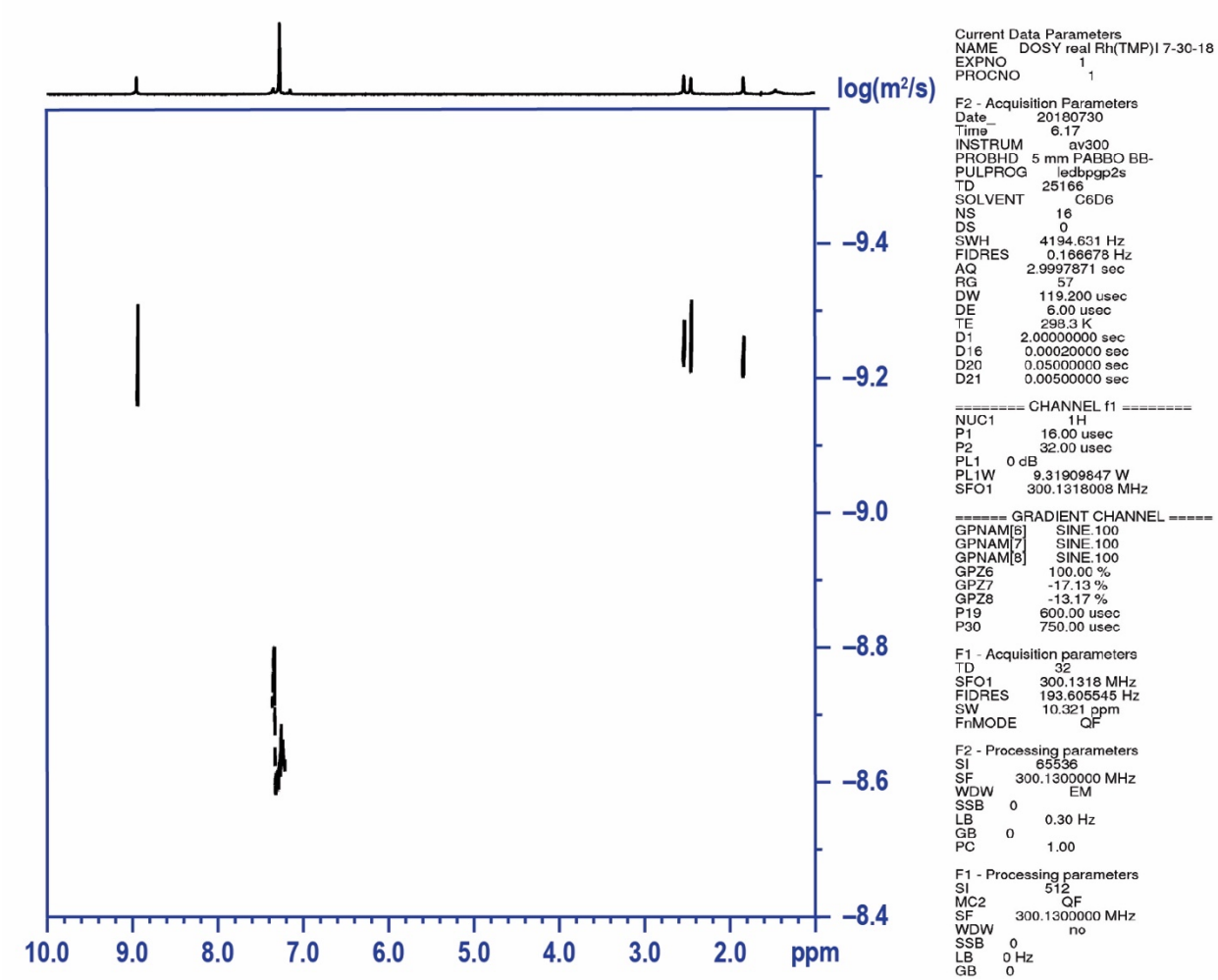

Figure S2.6. DOSY ^{1}H NMR spectrum of **1d** in C_6D_6. The major peaks of **1d** appear at 1.88, 2.47, 2.58, and 8.96 ppm. The largest peak is due to solvent and appears at 7.37 ppm. The diffusion coefficient of **1d** is determined to be 5.62×10^{-10} $m^2 \cdot s^{-1}$.

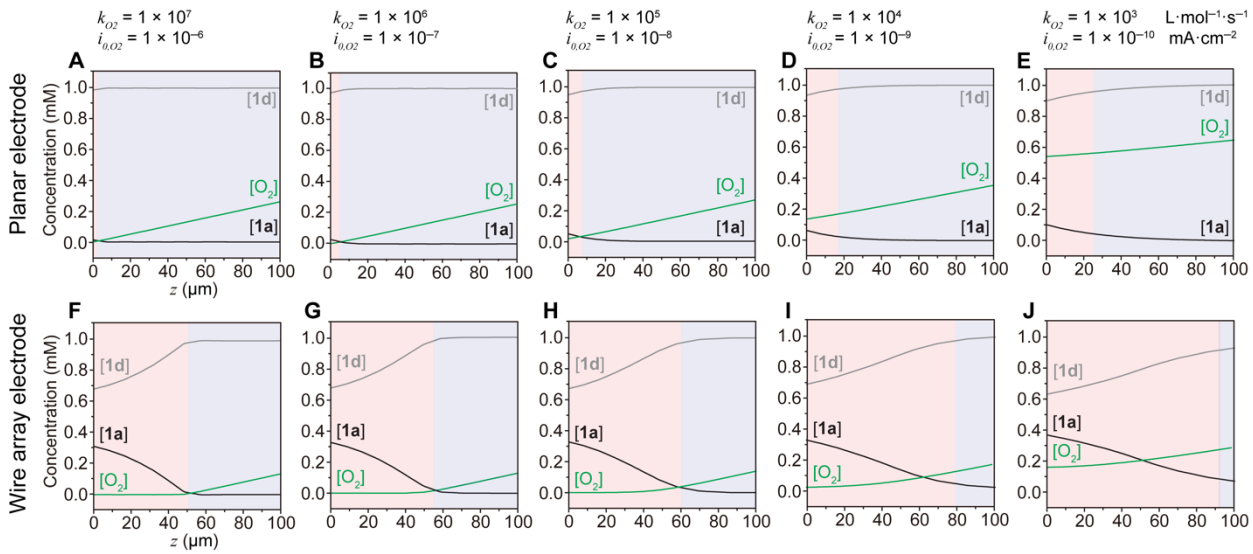

Figure S2.7. Simulation results of concentrations of **1a**, **1d** and O_2, denoted as [**1a**], [**1d**] and [O_2] on a wire array electrode (50 μm length, 4 μm diameter and 15 μm periodicity) respectively, versus the distance away from the bottom of array (z). (**A**) to (**E**), planar electrode; (**F**) to (**J**), wire array electrode. The region with the accumulation of CH_4-reactive **1a** is colored in pink, while the aerobic region in blue. The electrode geometry is the same among **f** to **j**. k_{O2}, the second-order reaction rate constant between O_2 and **1a**; $i_{0,O2}$, the exchange current density for the reduction of O_2. (**A**) and (**F**), k_{O2} = 1×10^7 L·mol^{-1}·s^{-1}, $i_{0,O2}$ = 1×10^{-6} mA/cm^2; (**B**) and (**G**), same as Figures 2.3A and 2.3B, k_{O2} = 1×10^6 L·mol^{-1}·s^{-1}, $i_{0,O2}$ = 1×10^{-7} mA/cm^2; (**C**) and (**H**), k_{O2} = 1×10^5 L·mol^{-1}·s^{-1} $i_{0,O2}$ = 1×10^{-8} mA/cm^2; (**D**) and (**I**), k_{O2} = 1×10^4 L·mol^{-1}·s^{-1}, $i_{0,O2}$ = 1×10^{-9} mA/cm^2; (**E**) and (**J**), k_{O2} = 1×10^3 L·mol^{-1}·s^{-1}, $i_{0,O2}$ = 1×10^{-10} mA/cm^2.

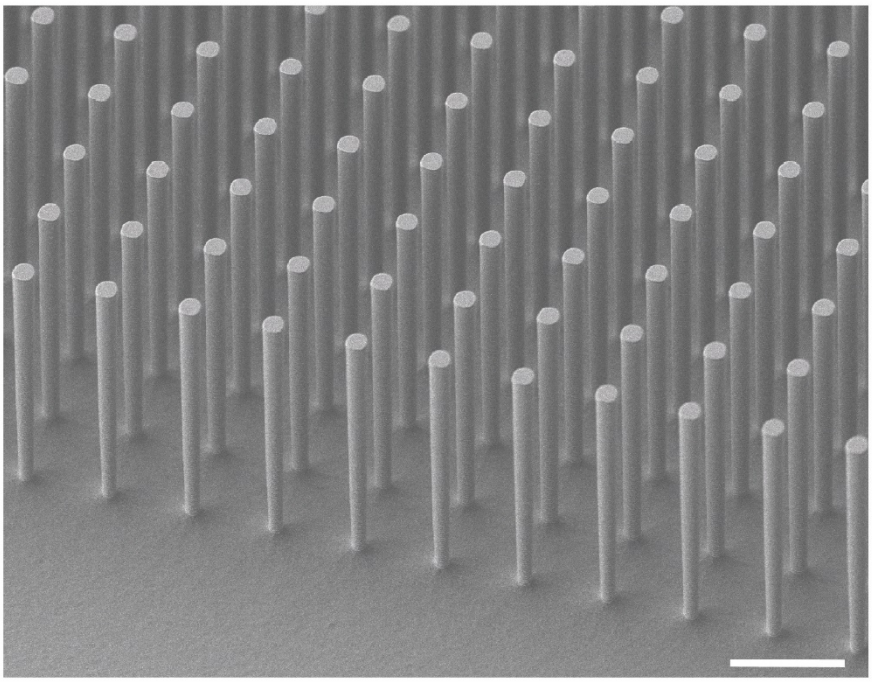

Figure S2.8. 45°-tilting SEM image of Si wire array used for optical mapping of concentration gradient. The scale bar, 20 μm.

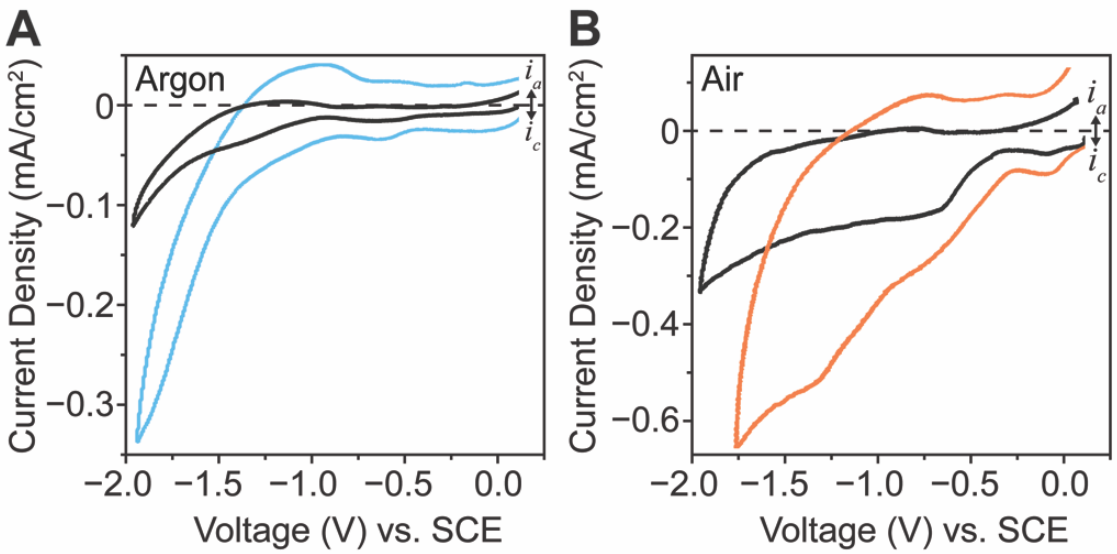

Figure S2.9. Cyclic voltammograms on Si wire electrodes in Ar (**A**) and air (**B**). Black trace, blank without the addition of **1d**; blue and orange traces, 1 mM **1d**. 0.1 M $TBAClO_4$ in 1,2-DFB, 100 mV/s.

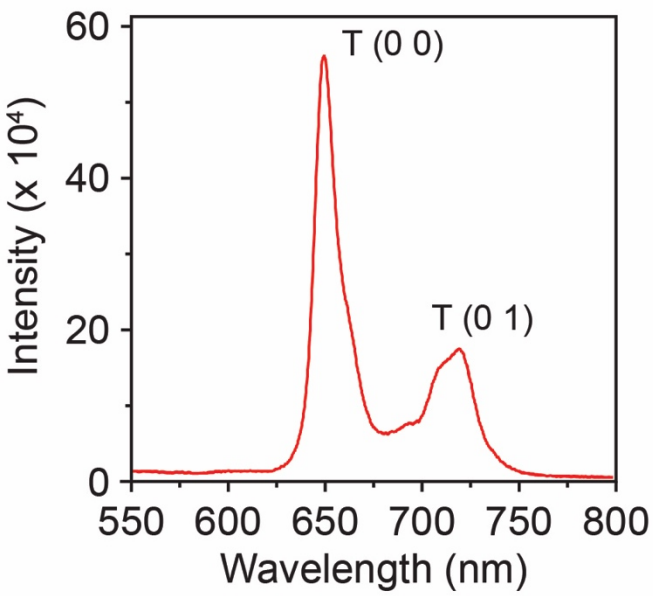

Figure S2.10. Phosphorescence emission spectrum of **1d** under a 526-nm excitation. The assignment of transitions from the triplet states are listed.[68]

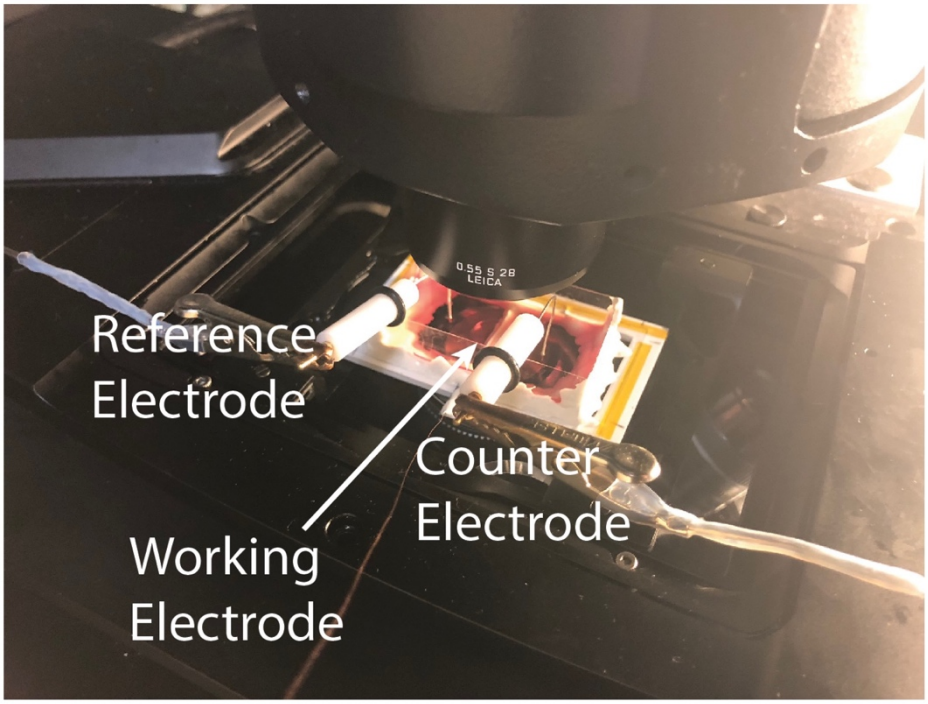

Figure S2.11. Photograph of an electrochemical setup used for *in situ* mapping of phosphorescence emission under a confocal optical microscope.

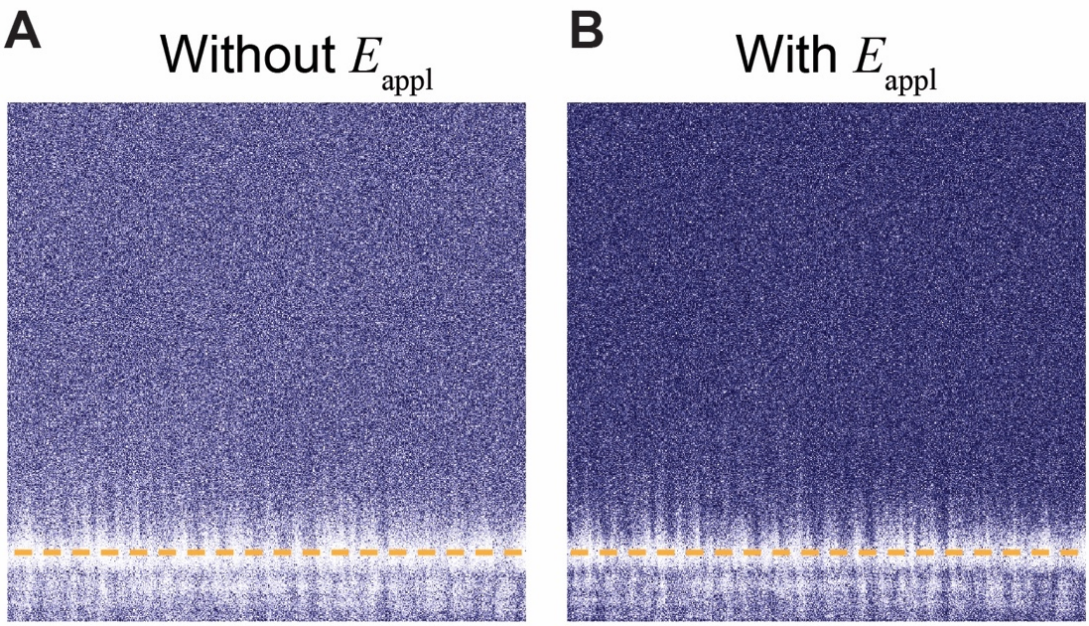

Figure S2.12. Cross-sectional heatmaps of unnormalized phosphorescence intensity on a planar electrode without (**A**) and with (**B**) E_{appl}. The surface of Si planar electrode is delineated in yellow. No significant concentration gradient was built near a planar electrode despite a uniform background change. 0.1 mM **1d** in the bulk solution, 0.1 M $TBAClO_4$ in 1,2-DFB, E_{appl} = −1.5 V vs. SCE.

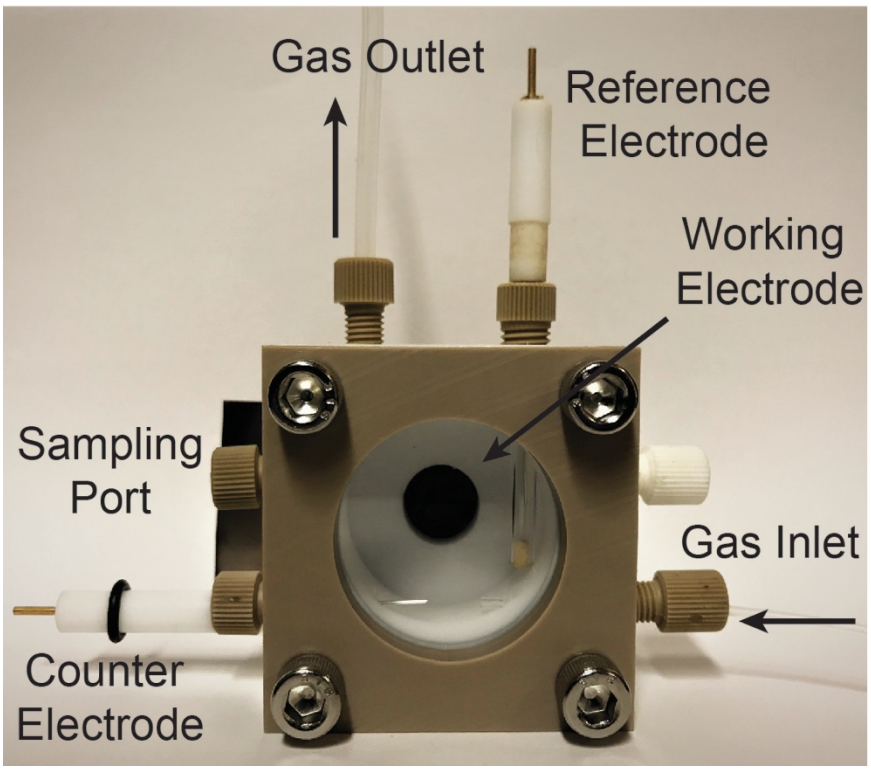

Figure S2.13. Photograph of the customized electrochemical reactor used for bulk electrolysis.

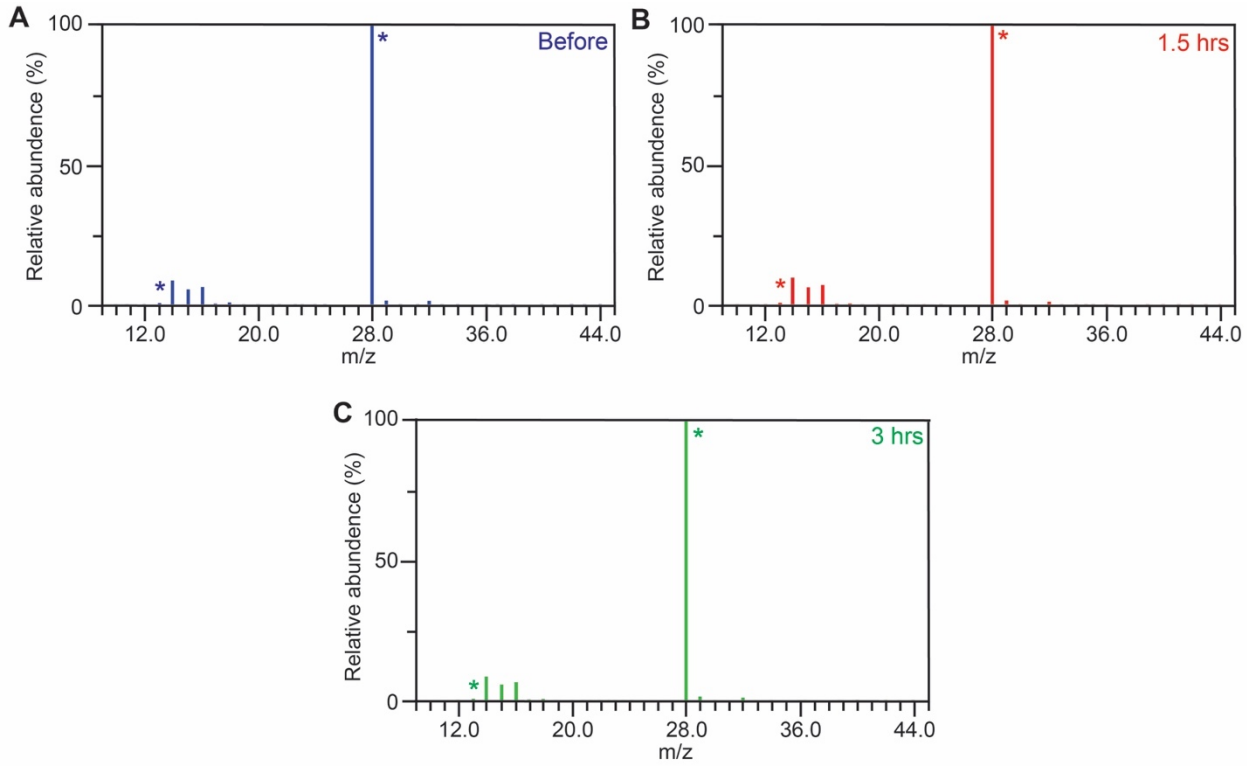

Figure S2.14. Mass spectra of gas samples taken before the bulk electrolysis (**A**), as well as 1.5 hrs (**B**) and 3 hrs (**C**) after the commencement of bulk electrolysis. The marked peaks, at m/z ratios of 14 and 28, correspond to the fragments of N_2. CO was monitored at an m/z fragment of 12 and CO_2 was monitored at a fragment of 44 m/z. CO and CO_2 were not detectable as products during the bulk electrolysis.

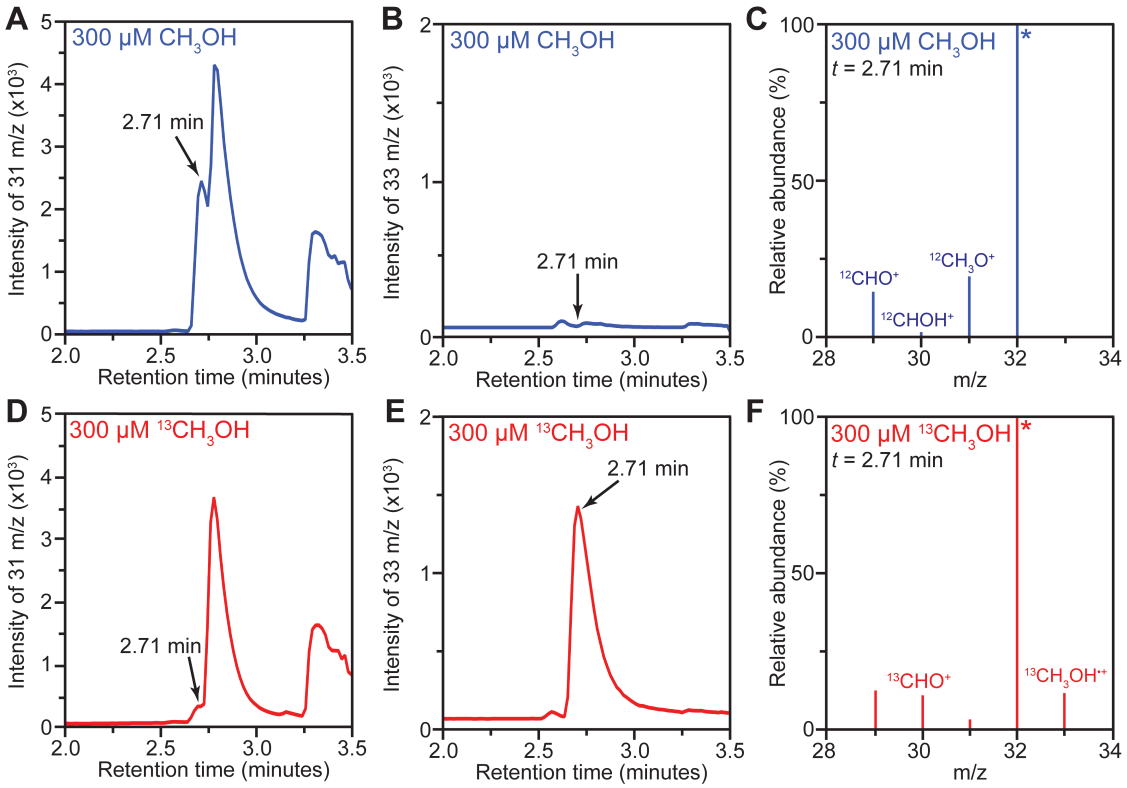

Figure S2.15. GC-MS elusion traces when monitored at m/z = 31 (**A** and **D**) or at m/z = 33 (**B** and **E**) for CH_3OH of natural abundance and $^{13}CH_3OH$, respectively. The mass spectra at an elution time of 2.71 min, the position of CH_3OH peaks, were also displayed for CH_3OH of natural abundance (**C**) and $^{13}CH_3OH$ (**F**).

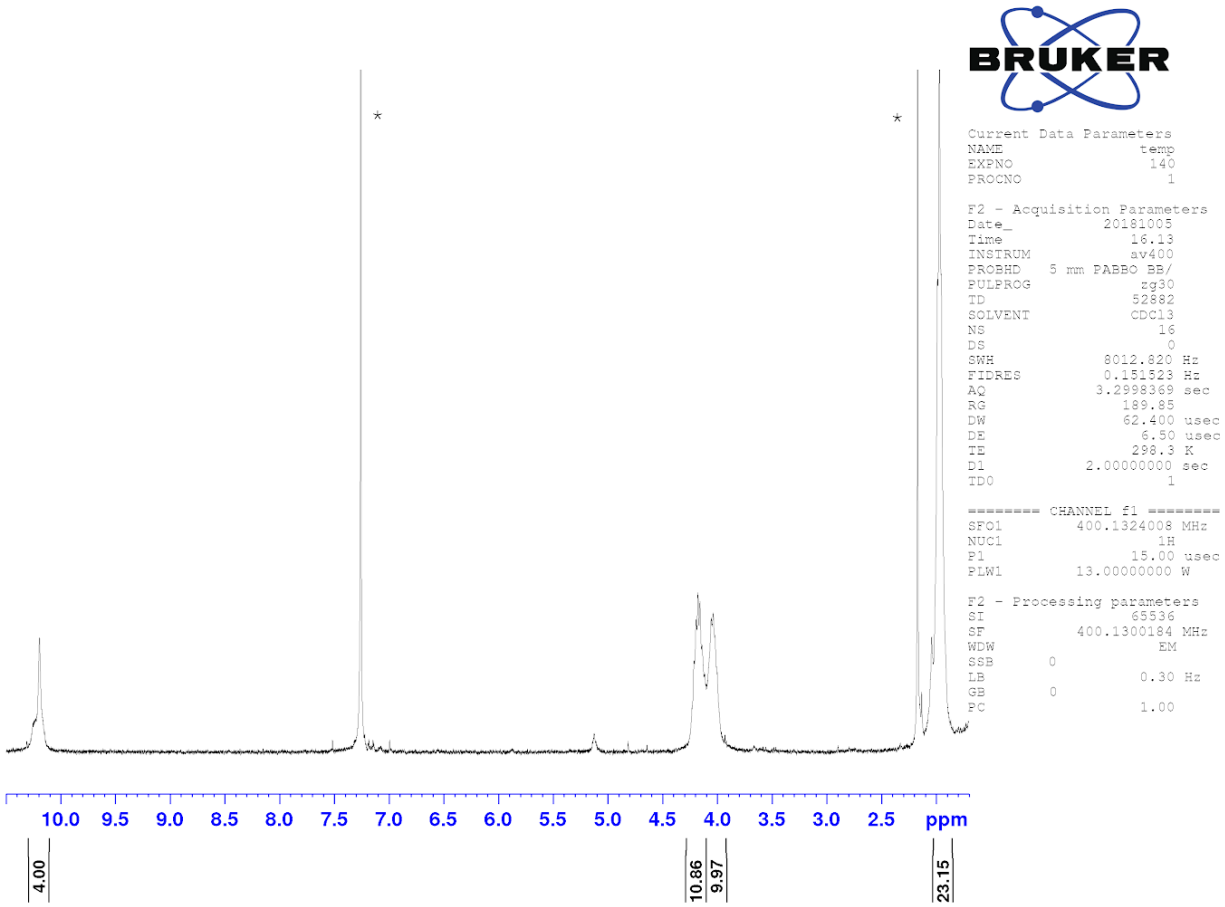

Figure S2.16. ^{1}H NMR spectrum of **2** in $CDCl_3$. All integrations are referenced to the peak at 10.28 ppm. The solvent peak, $CDCl_3$, appears at 7.27 ppm. The marked peaks are due to solvent, $CHCl_3$, and residual acetone.

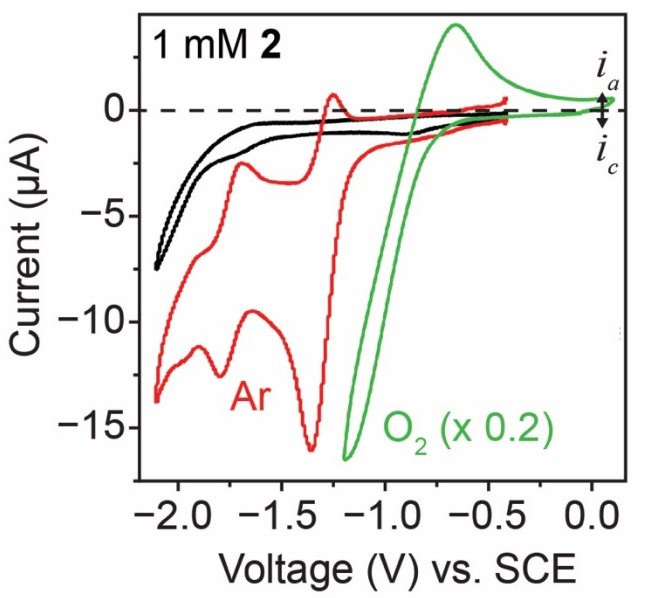

Figure S2.17. Cyclic voltammograms of 1 mM **2** with 0.1 M $TBAClO_4$ in 1,2-DFB under Ar (red) and air (green) environment. Black, blank solution without **2**. 100 mV/s; Pt working electrode for blank and in Ar, glassy carbon electrode in air. The current in O_2 is multiplied by a factor of 0.2.

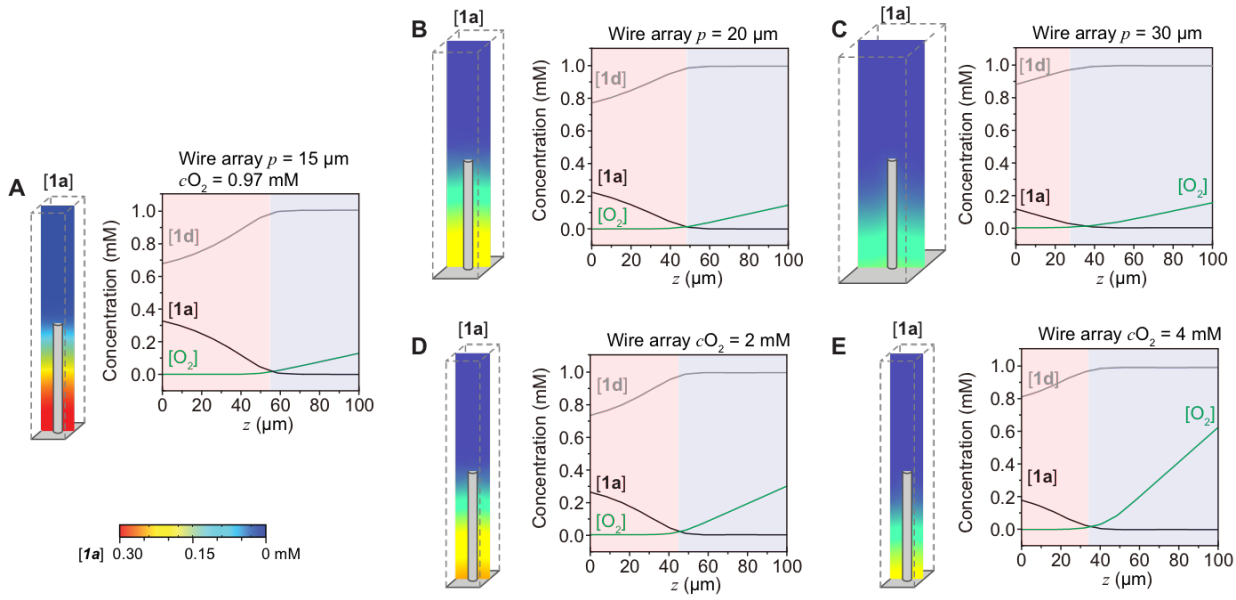

Figure S2.18. (**A**) to (**E**), simulation results of wire arrays with different periodicities of wire array (p) and bulk O_2 concentrations (C_{O2}). The concentrations of **1a**, **1d** and O_2, denoted as [**1a**], [**1d**] and [O_2] respectively, were plotted versus the distance away from electrode surface (z). The region with the accumulation of CH_4-reactive **1a** is colored in pink, while the aerobic region in blue. (**A**), same as Figure 2.2B, whose conditions corresponds to a 0.1 bar partial pressure of O_2.

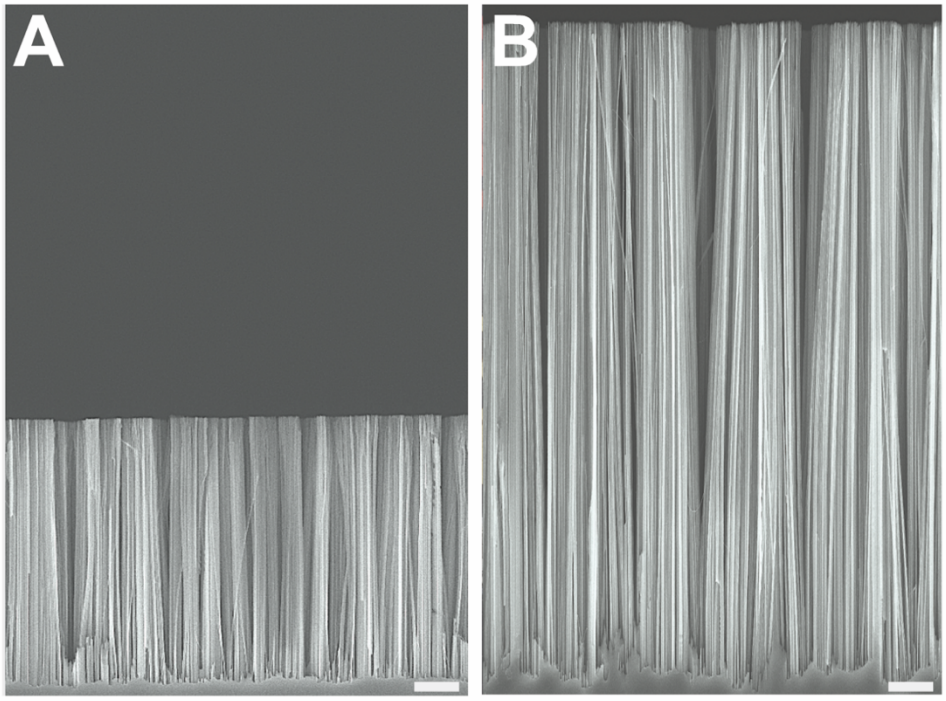

Figure S2.19. SEM images of (**A**) 10-μm and (**B**) 27-μm Si nanowire arrays. The scale bars in both images correspond to 2 μm.

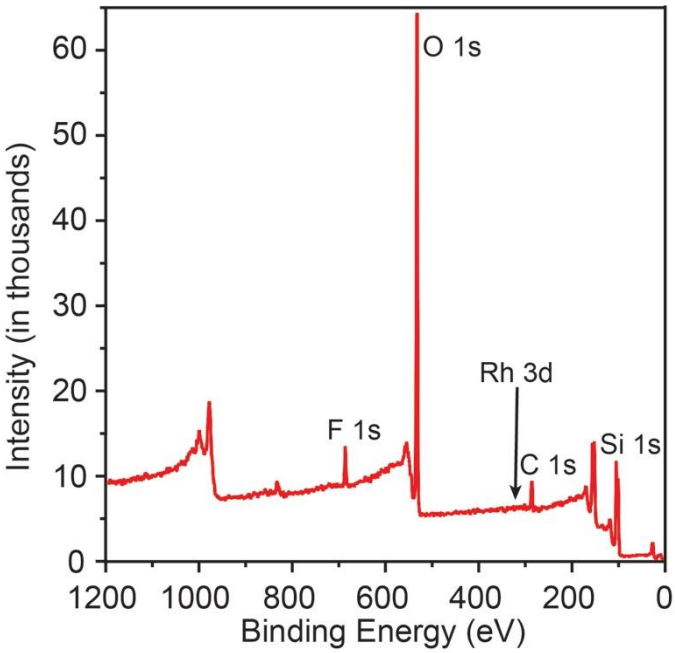

Figure S2.20. Spectrum of X-ray photoelectron spectroscopy for the surface of Si nanowire after a 3-hr bulk electrolysis with the condition of entry *23* in Supplementary Table 2.1.

Supplementary References

(36) Bard, A. J.; Faulner, L. R. Electrochemical Methods: Fundamentals and Applications. 2nd ed. John Wiley & Sons, Inc., New York, **2001**.

(37) Xiang,C.; Meng, A. C.; Lewis, N. S. Evaluation and optimization of mass transport of redox species in silicon microwire-array photoelectrodes. *Proc. Natl. Acad. Sci. U. S. A.* **2012**, *109*, 15622−15627.

(38) Sato, T.; Hamada, Y.; Sumikawa, M.; Araki, S.; Yamamoto, H. Solubility of Oxygen in Organic Solvents and Calculation of the Hansen Solubility Parameters of Oxygen. *Ind. Eng. Chem. Res.* **2014**, *53*, 19331−19337.

(39) Schumpe, A.; Luehring, P. Oxygen diffusivities in organic liquids at 293.2 K. *J. Chem. Eng. Data* **1990**, *35*, 24−25.

(40) Zimmermann, T.; Soorholtz, M.; Bilke, M.; Schüth, F. Selective Methane Oxidation Catalyzed by Platinum Salts in Oleum at Turnover Frequencies of Large-Scale Industrial Processes. *J. Am. Chem. Soc.* **2016**, *138*, 12395−12400.

(41) Hashiguchi, B. G.; Konnick, M. M.; Bischof, S. M.; Gustafson, S. J.; Devarajan, D.; Gunsalus, N.; Ess, D. H.; Periana, R. A. Main-Group Compounds Selectively Oxidize Mixtures of Methane, Ethane, and Propane to Alcohol Esters. *Science* **2014**, *343*, 1232−1237.

(42) Periana, R. A.; Mironov, O.; Taube, D.; Bhalla, G.; Jones, C. Catalytic, Oxidative Condensation of CH_4 to CH_3COOH in One Step via CH Activation. *Science* **2003**, *301*, 814−818.

(43) Mironov, O. A.; Bischof, S. M.; Konnick, M. M.; Hashiguchi, B. G.; Ziatdinov, V. R.; Goddard, W. A.; Ahlquist, M.; Periana, R. A. Using Reduced Catalysts for Oxidation

Reactions: Mechanistic Studies of the "Periana-Catalytica" System for CH_4 Oxidation. *J. Am. Chem. Soc.* **2013**, *135*, 14644−14658.

(44) Smith, K. T.; Berritt, S.; Gonzales-Moreiras, M.; Ahn, S.; Smith III, M. R.; Baik, M.-H.; Mindiola, D. J.. Catalytic borylation of methane. *Science* **2016**, *351*, 1424−1427.

(45) Sadow, A. D.; Tilley, T. D. Homogeneous Catalysis with Methane. A Strategy for the Hydromethylation of Olefins Based on the Nondegenerate Exchange of Alkyl Groups and σ-Bond Metathesis at Scandium. *J. Am. Chem. Soc.* **2003**, *125*, 7971−7977.

(46) Meyer, D.; Taige, M. A.; Zeller, A.; Hohlfeld, K.; Ahrens, S.; Strassner, T. Palladium Complexes with Pyrimidine-Functionalized N-Heterocyclic Carbene Ligands: Synthesis, Structure and Catalytic Activity. *Organometallics* **2009**, *28*, 2142−2149.

(47) Hu, A.; Guo, J.-J.; Pan, H.; Zuo, Z. Selective functionalization of methane, ethane, and higher alkanes by cerium photocatalysis. *Science*, **2018**, *361*, 668−672.

(48) Chepaikin, E. G.; Bezruchenko, A. P.; Leshcheva, A. A.; Boyko, G. N.; Kuzmenkov, I. V.; Grigoryan, E. H.; Shilov, A. E. Functionalisation of methane under dioxygen and carbon monoxide catalyzed by rhodium complexes: oxidation and oxidative carbonylation. *J. Mol. Cat. A: Chemical* **2001**, *169*, 89−98.

(49) Chan, S. I.; Lu, Y.-J.; Nagababu, P.; Maji, S.; Hung, M.-C.; Lee, M. M.; Hsu, I.-J.; Minh, P. D.; Lai, J. C.-H.; Ng, K. Y.; Ramalingam, S.; Yu, S. S.-F.; Chan, M. K. Efficient Oxidation of Methane to Methanol by Dioxygen Mediated by Tricopper Clusters. *Ang. Chem., Int. Ed.*, **2013**, *52*, 3731−3735.

(50) Agarwal, N.; Freakley, S. J.; Mcvicker, R. U.; Althahban, S. M.; Dimitratos, N.; He, Q.; Morgan, D. J.; Jenkins, R. L.; Willock, D. J.; Taylor, S. H.; Kiely, C. J.; Hutchings, G. J.

Aqueous Au-Pd colloids catalyze selective CH_4 oxidation to CH_3OH with O_2 under mild conditions. *Science* **2017**, *358*, 223−227.

(51) Sushkevich, V. L.; Palagin, D.; Ranocchiari, M.; van Bokhoven, J. A. Selective anaerobic oxidation of methane enables direct synthesis of methanol. *Science* **2017**, *356*, 523−527.

(52) Hutchings, G. J.; Taylor, S. H. Designing oxidation catalysts. *Catal. Today* **1999**, *49*, 105−113.

(53) Hammond, C., *et al.* Direct Catalytic Conversion of Methane to Methanol in an Aqueous Medium by using Copper-Promoted Fe-ZSM-5. *Angew. Chem., Int. Ed.* **2012**, *51*, 5129−5133.

(54) Starokon, E. V., *et al.* Oxidation of methane to methanol on the surface of FeZSM-5 zeolite. *J. Catal.* **2013**, *300*, 47−54.

(55) Xie, J., *et al.* Highly selective oxidation of methane to methanol at ambient conditions by titanium dioxide-supported iron species. *Nat. Catal.* **2018**, *1*, 889−896.

(56) Baek, J., *et al.* Bioinspired Metal–Organic Framework Catalysts for Selective Methane Oxidation to Methanol. *J. Am. Chem. Soc.* **2018**, *140*, 18208−18216.

(57) Cui, X., *et al.* Room-Temperature Methane Conversion by Graphene-Confined Single Iron Atoms. *Chem* **2018**, *4*, 1902−1910.

(58) Anderson, J. R.; Tsai, P. Methanol from oxidation of methane by nitrous oxide over FeZSM5 catalysts. *J. Chem. Soc., Chem. Commun.*, **1987**, *0* ,1435−1436.

(59) Tang, P.; Zhu, Q.; Wu, Z.; Ma, D. Methane activation: the past and future. *Energy Environ. Sci* **2014**, *7*, 2580−2591.

(60) Shan, J.; Li, M.; Allard, L. F.; Lee, S.; Flytzani-Stephanopoulos, M. Mild oxidation of methane to methanol or acetic acid on supported isolated rhodium catalysts. *Nature* **2017**, *551*, 605−608.

(61) Liu, C.-C.; Mou, C. Y.; Yu, S. S. F.; Chan, S. I. Heterogeneous formulation of the tricopper complex for efficient catalytic conversion of methane into methanol at ambient temperature and pressure. *Energy Environ. Sci***. 2016**, *9*, 1361−1374.

(62) Groothaert, M. H.; Smeets, P. J.; Sels, B. F.; Jacobs, P. A.; Schoonheydt, R. A. Selective Oxidation of Methane by the Bis(μ-oxo)dicopper Core Stabilized on ZSM-5 and Mordenite Zeolites. *J. Am. Chem. Soc.* **2005**, *127*, 1394−1395.

(63) Grundner, S.; Markovits, M. A. C.; Li, G.; Tromp, M.; Pidko, E. A.; Hensen, E. J. M.; Jentys, A.; Sanchez-Sanchez, M.; Lercher, J. A. Single-site trinuclear copper oxygen clusters in mordenite for selective conversion of methane to methanol. *Nat. Comm.* **2015**, *6*, 7546.

(64) Starokon, E. V.; Parfenov, M. V.; Pirutko, L. V.; Abornev, S. I.; Panov, G. I. Room-Temperature Oxidation of Methane by α-Oxygen and Extraction of Products from the FeZSM-5 Surface. *J. Phys. Chem. C* **2011**, *115*, 2155−2161.

(65) Beznis, N. V.; van Laak, A. N. C.; Weckhuysen, B. M.; Bitter, J. H. Oxidation of methane to methanol and formaldehyde over Co–ZSM-5 molecular sieves: Tuning the reactivity and selectivity by alkaline and acid treatments of the zeolite ZSM-5 agglomerates. *Micro. Meso. Mater.* **2011**, *138*, 176−183.

(66) Narsimhan, K.; Iyoki, K.; Dinh, K.; Román-Leshkov, Y. Catalytic Oxidation of Methane into Methanol over Copper-Exchanged Zeolites with Oxygen at Low Temperature. *ACS Centr. Sci***. 2016**, *2*, 424−429.

(67) Shan, J.; Huang, W.; Nguyen, L.; Yu, Y.; Zhang, S.; Yuanyuan Li, Y.; Frenkel, A. I.; Tao, F. Conversion of Methane to Methanol with a Bent Mono(μ-oxo)dinickel Anchored on the Internal Surfaces of Micropores. *Langmuir* **2014**, *30*, 8558−8569.

(68) Hanson, L. K.; Gouterman, M.; Hanson, J. C. Porphyrins. XXIX. Crystal and molecular structure and luminescence of bis(dimethylamine)etio(I)porphinatorhodium(III) chloride dihydrate. *J. Am. Chem. Soc.* **1973**, *95*, 4822−4829.

Chapter 3. Uncovering the identity and the role of the terminal oxidant in the ambient air oxidation of CH_4 to CH_3OH

This chapter is a version of Natinsky, B. S.; Jolly, B. J.; Dumas, D. M.; Liu, C. "Efficacy analysis of compartmentalization for ambient CH_4 activation mediated by Rh^{II} metalloradical in nanowire array electrode." *Chemical Science*. **2021**, *12*, 1818–1825.

Abstract

In this study, we build off our previously reported CH_4-to-CH_3OH catalysis mediated by an O_2-deactivating Rh^{II} metalloradical with O_2 as the terminal oxidant in the Si nanowire array electrode, reporting our findings on the identity of the terminal oxidant in such catalysis. We experimentally identified and quantified the productivity of key reaction intermediates, including Rh^{II} metalloradical and reactive oxygen species from O_2. *In situ* electron paramagnetic resonance spectroscopic studies uncovered the immediate O_2 reduction product from reaction with the electrode surface as superoxide, while constant potential bulk electrolysis experiments with a superoxide-selective chromophore quantified the rate of superoxide generation in solution.

Introduction

Reactive oxygen species (ROS) are integral in many biochemical processes and energy technologies.[1] Biological aerobic metabolism couples oxygen (O_2) reduction with the transfer of protons across the lipid bilayer to fuel the production of adenosine triphosphate (ATP).[2] On the other hand, fuel cell technologies typically rely on O_2 as the terminal electron acceptor.[3] The catalyst for the oxygen reduction reaction (ORR), through which ROS are created, steers product distribution and dictates the identity of the major ROS.

Previously, our group combined a nanowire-structured electrode with electricity to create a microscopic O_2 gradient, allowing an O_2-sensitive rhodium tetramesityl porphyrin metalloradical (Rh^{II}) catalyst to perform C–H activation under ambient conditions.[4] At sufficient cathodic potential, the rhodium-based pre-catalyst (Rh-cat) was activated towards methane (CH_4) while simultaneously reducing O_2 and depleting it within the wire array. The limiting of O_2 transport into the nanowire electrode maintains an environment in which the Rh^{II}-cat complex remains stable and active towards CH_4. Upon its reaction with CH_4, the methylated species (Rh^{III}–CH_3) must diffuse away and react with an oxidant to generate methanol (CH_3OH). Since O_2 remains necessary for the overall conversion, the ROS generated from reaction of O_2 with the electrode surface doubles as the terminal oxidant. Additionally, the nature of this reaction is highly dependent on the identity of the ROS as well as the role of the nanowire array in compartmentalizing the reaction pathway leading up to Rh^{III}–CH_3 formation.

The product of O_2 reduction upon contact with the electrode can be a myriad of species, leaving us to question its true identity. Depending on the applied potential, the composition of the electrode surface[5], and the local concentration of available protons (H^+)[6], O_2 can be reduced to superoxide ($O_2^{\cdot-}$), hydroxyl radical (•OH), hydrogen peroxide (H_2O_2), or water (H_2O). The latter two products represent multielectron and multiproton processes typically catalyzed by precious metals, such as gold[7] or platinum[8]. Thus, $O_2^{\cdot-}$ or •OH were the hypothesized products as silicon (Si) is used as the working electrode in a nonaqueous environment. It is customary for Si to be a source of electrons rather than active catalyst due its more inert chemical nature, similar to carbon-based electrodes (i.e. glassy carbon or graphite).[9] Here, we report a clearer mechanistic picture conveying experimental evidence that illustrates the most likely identity of the ROS and studies uncovering its role in CH_3OH formation.

Results and Discussion

The identity of the predominant ROS was probed by electron paramagnetic resonance (EPR) spectroscopy with the addition of spin trap agent 5,5-dimethyl-1-pyrroline N-oxide (DMPO) during the electrolysis.[10, 11] Superoxide ($O_2^{\bullet-}$), hydrogen peroxide (H_2O_2), and hydroxyl radical (•OH) were presumed to be the possible ROS from O_2 reduction in aprotic solvent systems.[5, 12] Among those possible ROS, H_2O_2, along with other hydroperoxide species, react with DMPO to yield the adduct DMPO–OH•, which can be detected by EPR spectroscopy.[13] While $O_2^{\bullet-}$ and •OH are short-lived, [12, 14] their reactions with DMPO yield more stable adducts DMPO–$O_2^{\bullet-}$ and DMPO–OH•, whose prolonged lifetimes are roughly 1 and 20 minutes, respectively, at room temperature and much longer at liquid N_2 condition.[11] By trapping the generated ROS with DMPO during the electrolysis and discerning the trapped radicals in EPR spectroscopy[11, 15, 16] the possible presence of $O_2^{\bullet-}$ and H_2O_2/•OH could be unveiled.

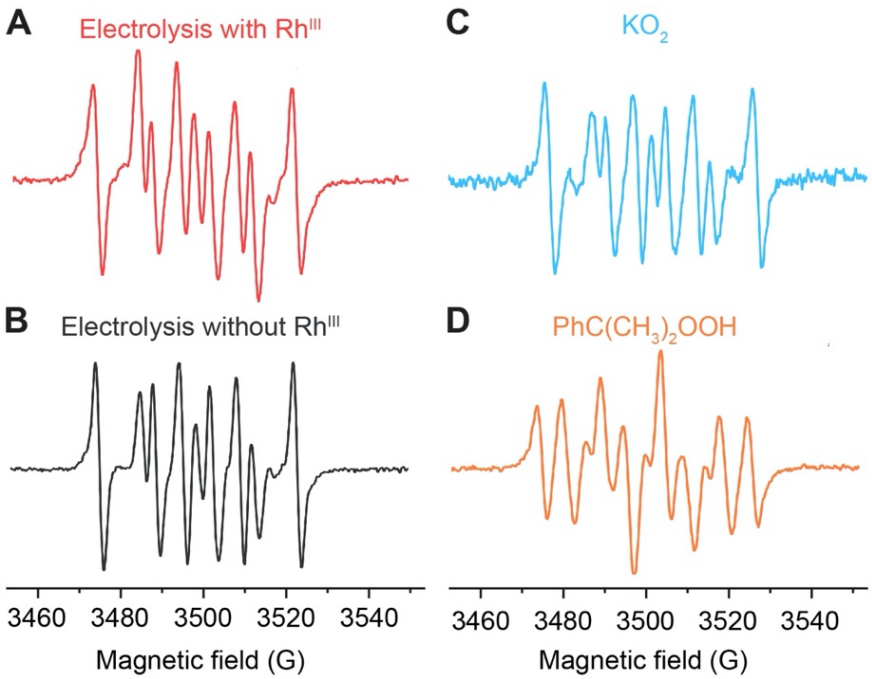

Figure 3.1. Electron paramagnetic resonance (EPR) spectra depicting the adducts formed in the reaction of 50 mM DMPO (5,5-dimethyl-1-pyrroline N-oxide): (**A**) the electrolysis with Rh catalyst during CH_4-to-CH_3OH conversion; (**B**) control electrolysis in the absence of Rh catalyst; (**C**) 0.5 mM potassium superoxide (KO_2); (**D**) 0.5 mM 2-hydroperoxypropan-2-ylbenzene ($PhC(CH_3)_2OOH$, cumene hydroperoxide). Unless otherwise noted, in the electrolyte solution, 0.1 M tetrabutylammonium perchlorate ($TBAClO_4$) in 1,2-difluorobenzene (1,2-DFB). Following previously reported condition,[4] chronoamperometry was conducted at –1.4 V vs. SCE with Si nanowire working electrode under a constant flow of CH_4/air mixture P_{CH4}/P_{air} = 35 in a customized electrochemical reactor (Figure S3.1) under ambient pressure.

EPR spectra indicate that $O_2^{\bullet-}$ is the predominant ROS during the CH_4-to-CH_3OH conversion. As reported in our previous work[4], CH_4-to-CH_3OH catalysis was conducted in a customized single-chamber electrochemical reactor (Figure S3.1), which was fed by a mixture of CH_4 and air (P_{CH4}/P_{air} = 35) at a constant flow rate at ambient pressure and room temperature. Chronoamperometry of –1.4 V vs. Saturated Calomel Electrode (SCE) was applied in 1,2-DFB with 1 mM of Rh^{III} as the pre-catalyst and 0.1 M tetrabutylammonium perchlorate ($TBAClO_4$) as the supporting electrolyte. A Si nanowire array with average wire length of 15 μm and diameter of 50 nm (Figure S3.2), prepared based on literature[4, 17], was used as the working electrode with a Pt wire counter electrode and a Ag^+/Ag pseudo-reference electrode equipped with a glass frit. 50 mM DMPO was added during the electrolysis to trap the generated ROS, and aliquots were taken for EPR experiments 5, 15, and 60 minutes after the addition of DMPO. Unless stated specifically, the aliquots were stored in liquid N_2 before the EPR measurement, although the DMPO adduct has been observed to be stable at room temperature for at least 90 minutes (Figure S3.3). We note that

the addition of DMPO per se does not significantly alter the electrochemistry in the system, if any, because previous study has shown that DMPO is cathodically stable up to –2.35 V vs. SCE.[18] The EPR spectrum from the aliquot 15 minutes after DMPO addition is shown in Figure 3.1A, which is similar to the ones from the aliquot taken at 5 and 60 minutes after DMPO addition (Figure S3.4). This similarity suggests that the radical species observed in EPR spectroscopy is the predominant species at the steady state during the electrolysis and not all of the transient ROS involved in the catalytic cycle may be captured in our experiments. Control experiments include the DMPO-added electrolysis without Rh^{III} pre-catalyst (Figure 3.1B), the mixture between DMPO and 0.5 mM KO_2 as a surrogate of $O_2^{\bullet-}$ (Figure 3.1C and Figure S3.5), as well as the mixture between DMPO and 0.5 mM 2-hydroperoxypropan-2-ylbenzene ($PhC(CH_3)_2OOH$, cumene hydroperoxide) as a surrogate of H_2O_2/•OH (Figure 3.1D and Figure S3.5). The captured ROS during electrolysis is predominantly $O_2^{\bullet-}$, based on the similar spectra shown in Figure 3.1A and 3.1C. However, the spectral pattern observed of the DMPO–$O_2^{\bullet-}$ in 1,2-DFB and 0.1 M $TBAClO_4$ solution is noticeably distinct from the DMPO–OOH observed in aqueous solvent. This difference can be rationalized by the employment of 1,2-DFB in place of H_2O and the resulting solvation sphere surrounding the adduct, the reduced proton concentration, and the possibility of TBA^+ cations to coordinate the anionic complex, which could explain the increased stability of the observed adduct upwards of 90 min. The similarity between Figures 3.1A and 3.1B suggests that it is likely that the electrochemistry of Si nanowire other than the Rh species is responsible for the generation of $O_2^{\bullet-}$.

We propose to quantify the generated ROS, predominantly $O_2^{\bullet-}$ at steady-state, by colorimetric assay with the use of nitroblue tetrazolium (NBT) chloride as a $O_2^{\bullet-}$-selective chromogen. NBT is reported to selectively react with the $O_2^{\bullet-}$ over H_2O_2 and other ROS[19], leading to the emergence of

a purple color in monoformazan, with a maximum absorption peak at ~530 nm[19, 20], from a pale yellow background. The stoichiometric reactivity between NBT and $O_2^{\bullet-}$ (1:2), ensured by utilizing a concentration of NBT / $O_2^{\bullet-}$ < 2, enables the use of UV-Vis absorption spectroscopy for the quantification of $O_2^{\bullet-}$ generation.[19, 21-23] Additionally, the NBT exhibits minimal reductive activity in organic solvent within its electrochemical window, which was not only reported in previous literature[21] but also shown in our cyclic voltammograms (Figure S3.6) and chronoamperometry (Figure 3.2A) on a glassy carbon working electrode in 0.1 M $TBAClO_4$ solution of 1,2-DFB. Thus, when added during the electrolysis under CH_4-to-CH_3OH condition, the NBT will have minimal interference with the O_2-reducing electrode and act as an $O_2^{\bullet-}$ scavenger for a colorimetric quantification of the accumulated $O_2^{\bullet-}$. While multiple methods including fluorescence measurements are viable for the $O_2^{\bullet-}$ quantification[22], the absorbance at 600 nm from monoformazan after the reaction between NBT and $O_2^{\bullet-}$[21] was chosen in order to mitigate interference from the optical absorbance and phosphorescence of Rh species (630–750 nm).[24] Furthermore, due to the ephemeral nature of $O_2^{\bullet-}$ that hinders the preparation of a standard solution of known $O_2^{\bullet-}$ concentration[25, 26], we specifically designed experiments that establish a calibration curve of the absorbance at 600 nm which accounts for the stoichiometric reaction between NBT and KO_2, the $O_2^{\bullet-}$ surrogate.[26] When an increasing concentration of NBT was mixed with a fixed concentration of KO_2 in 1,2-DFB, the absorbance at 600 nm follows a linear correlation before plateauing (Figure 3B), illustrating a stoichiometric reaction between NBT and $O_2^{\bullet-}$ without other chromogenic side reactions. This led us to determine the absorption coefficient at 600 nm of the yielded monoformazan, ε_{600nm} = 4327 $M^{-1}\bullet cm^{-1}$ (R^2 = 0.97). Similar linear response between NBT and $O_2^{\bullet-}$ was also observed in the presence of Rh catalysts in 1,2-DFB

(Figure S3.7), which suggests that the presence of Rh^{III} in the bulk solution does not interfere with the colorimetric assay.

The rate of $O_2^{\bullet-}$ generation was quantified with the use of NBT in the nanowire-based cascade system for CH_4-to-CH_3OH conversion. Under the same electrochemical conditions with the use of Si nanowire array electrode of 15 μm length at –1.4 V vs. SCE, aliquots of electrolyte solution were sequentially sampled, measured for optical absorbance at 600 nm, and applied to calculate the amount of accumulated $O_2^{\bullet-}$. The yields of net accumulated $O_2^{\bullet-}$ (Y_{ROS}), normalized by the average electric current during electrolysis, were shown as a function of electrolysis duration in CH_4/air and N_2/air atmosphere (P_{CH4}/P_{air} and P_{N2}/P_{air} = 35; Figure 3.2C and 3.2D, respectively). The initial slopes of the Y_{ROS} before plateauing ($\partial Y_{ROS}/\partial t$) were determined as the rate of electrochemical ROS generation in the compartmentalized cascade reaction. $\partial Y_{ROS}/\partial t$ = 18±4 and 22±4 $\mu M \bullet mA^{-1} \bullet min^{-1}$ in CH_4/O_2 atmosphere with the presence and absence of 1 mM Rh^{III} (n = 4 and n = 3; purple and orange traces in Figure 3.2C, respectively); $\partial Y_{ROS}/\partial t$ = 16±4 and 23±3 $\mu M \bullet mA^{-1} \bullet min^{-1}$ in the N_2/air with the presence and absence of 1 mM Rh^{III} (n = 5; yellow and blue traces in Figure 3.2D, respectively). The similar values of $\partial Y_{ROS}/\partial t$ between CH_4 and N_2 atmosphere suggests that the ROS formation is independent of the gaseous environment. The similar values of $\partial Y_{ROS}/\partial t$ with and without Rh^{III} suggests that the electrode surface of Si nanowire is primarily responsible for ROS generation, albeit the presence of Rh^{III} does seem to lower the ROS yield. Here we note that $\partial Y_{ROS}/\partial t$ could be underestimated, because NBT is less reactive towards other ROS that may be concurrently generated during the electrochemical process.

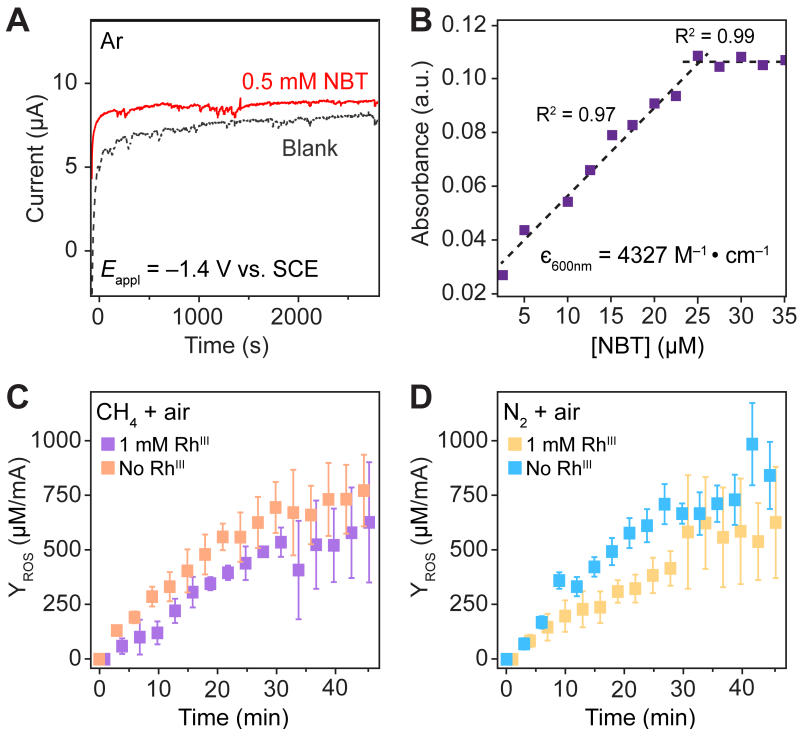

Figure 3.2. Quantification of superoxide ($O_2^{\bullet-}$) with $O_2^{\bullet-}$-selective chromogen nitroblue tetrazolium (NBT). (**A**) Chronoamperometry with glassy carbon working electrode in Ar. (**B**) The absorbance at 600 nm in 1,2-DFB of a fixed concentration of KO_2, a surrogate of ephemeral $O_2^{\bullet-}$, for varying concentrations of NBT. ε_{600nm}, the established absorption coefficient at 600 nm of the yielded monoformazan from stoichiometric reaction between NBT and $O_2^{\bullet-}$.[19] (**C**) and (**D**) The yield of ROS (Y_{ROS}), determined as the detected $O_2^{\bullet-}$ normalized by average electric current, are displayed against electrolysis duration with Si nanowire array of 15 μm length as working electrode. (**C**) CH_4/air atmosphere (P_{CH4}/P_{air} = 35) with (purple, n = 4) and without (orange, n = 3) 1 mM Rh^{III}. (**D**) N_2/air atmosphere (P_{N2}/P_{air} = 35) with (yellow, n = 5) and without (blue, n = 5) 1 mM Rh^{III}. –1.4 V vs. SCE in 1,2-DFB of 0.1M $TBAClO_4$. Error bars denote standard deviations.

Despite the findings that $O_2^{\bullet-}$ is the dominant ROS at steady state, we propose that $O_2^{\bullet-}$ is not the immediate oxidant that reacts with $Rh^{III}–CH_3$ for CH_3OH formation. We found that under strictly dry conditions, no CH_3OH was observed in a mixture of KO_2 and as-synthesized $Rh^{III}–CH_3$. Yet a stoichiometric amount of CH_3OH, calculated by ^1H NMR, was observed in experiments with $Rh^{III}–CH_3$ and KO_2 "wet" in 1,2-DFB (5.1±0.3 mM H_2O based on Karl Fischer titration). Along the same lines, 1:1 reactivity was observed upon mixing $Rh^{III}–CH_3$ with hydroperoxide species such as cumene hydroperoxide or *t*-Butyl hydroperoxide in dry 1,2-DFB.[4] Such observations prompted us to propose that trace hydroperoxide, namely H_2O_2, is constantly generated during the electrolysis and is the immediate reactant towards $Rh^{III}–CH_3$ to afford CH_3OH as the product. We speculate that the electrochemical reduction of O_2 to $O_2^{\bullet-}$ is followed by a chemical protonation step to generate other ROS such as a hydroperoxyl radical ($HO_2^{\bullet}$),[26] which is susceptible to heterolytic and homolytic cleavages and eventually converges on H_2O_2.[27-29] Whether the conversion of $HO_2^{\bullet}$ to H_2O_2 proceeds electrochemically or chemically should be dependent on the proton donor concentration in solution and the reduction potential applied.[29] Once the hydroperoxide species is formed, CH_3OH formation proceeds from its reaction with $Rh^{III}–CH_3$. Such mechanistic consideration would be useful in designing other ROS-initiated CH_4-activation reactions.

Conclusion

Here, we employed spin trap agents in conjunction with EPR spectroscopic studies to qualitatively identify $O_2^{\bullet-}$ as the immediate ROS synthesized upon O_2 reduction at the silicon nanowire array working electrode. Bulk electrolysis with added NBT chromophore, which selectively reacts with $O_2^{\bullet-}$, elucidated the rate and overall yield of $O_2^{\bullet-}$. Moreover, while $O_2^{\bullet-}$ is the immediately generated oxidant, reactions with H_2O impurities in the electrolyte suggest subsequent chemical

and/or electrode reaction steps that ultimately generate H_2O_2. This work uncovers the powerful role that the oxygen reduction species plays in generating CH_3OH from $Rh^{III}–CH_3$ to and can inform future work on the development of Rh porphyrin catalysts in oxidation reactions.

References

(1) Pegis, M. L.; Wise, C. F.; Martin, D. J.; Mayer, J. M. Oxygen Reduction by Homogeneous Molecular Catalysts and Electrocatalysts. *Chem. Rev.* **2018,** *118*, 2340−2391.

(2) Berg, J. M.; Tymoczko, J. L.; Stryer, L. Biochemistry, 4th ed.; Palgrave Macmillan: 1988.

(3) Pegis, M. L.; Wise, C. F.; Martin, D. J.; Mayer, J. M. Nanostructured Pt-alloy electrocatalysts for PEM fuel cell oxygen reduction reaction. *Chem. Soc. Rev.* **2010,** *39*, 2184−2202.

(4) Natinsky, B. S.; Lu, S.; Copeland, E. D.; Quintana, J. C.; Liu, C. Solution Catalytic Cycle of Incompatible Steps for Ambient Air Oxidation of Methane to Methanol. *ACS Cent. Sci.* **2019,** *5*, 1584−1590.

(5) Vasudevan, D.; Wendt, H. Electroreduction of oxygen in aprotic media. *J. Electroanalytical Chem.* **1995,** *392* (1), 69-74.

(6) Sawyer, D. T.; Chiericato, G.; Angelis, C. T.; Nanni, E. J.; Tsuchiya, T. Effects of media and electrode materials on the electrochemical reduction of dioxygen. *Anal. Chem.* **1982,** *54* (11), 1720-1724.

(7) Zhang, J.; Sasaki, K.; Sutter, E.; Adzic, R. R. Stabilization of Platinum Oxygen-Reduction Electrocatalysts Using Gold Clusters. *Science* **2007,** *315* (5809), 220-222.

(8) Stephens, I. E. L.; Bondarenko, A. S.; Grønbjerg, U.; Rossmeisl, J.; Chorkendorff, I. Understanding the electrocatalysis of oxygen reduction on platinum and its alloys. *Energy Environ. Sci.* **2012,** *5* (5), 6744-6762.

(9) Dai, L.; Xue, Y.; Qu, L.; Choi, H.-J.; Baek, J.-B. Metal-Free Catalysts for Oxygen Reduction Reaction. *Chem. Rev.* **2015,** *115* (11), 4823-4892.

(10) Buettner, G. R.; Oberley, L. W. Considerations in the spin trapping of superoxide and hydroxyl radical in aqueous systems using 5,5-dimethyl-1-pyrroline-1-oxide. *Biochem. Biophys. Res. Commun.* **1978,** *83*, 69−74.

(11) Makino, K.; Hagiwara, T.; Murakami, A. A mini review: Fundamental aspects of spin trapping with DMPO. *Int. J. Radiat. Appl. Instrum. C Radiat Phys. Chem.* **1991,** *37*, 657−665.

(12) Hayyan, M.; Hashim, M. A.; AlNashef, I. M. Superoxide Ion: Generation and Chemical Implications. *Chem. Rev.* **2016,** *116*, 3029−3085.

(13) Chen, L.; Kutsuna, S.; Yamane, S.; Mizukado, J. ESR spin trapping determination of the hydroperoxide concentration in polyethylene oxide (PEO) in aqueous solution. *Polym. Degrad. Stab.* **2017,** *139*, 89−96.

(14) Schmitt, F.-J.; Renger, G.; Friedrich, T.; Kreslavski, V. D.; Zharmukhamedov, S. K.; Los, D. A.; Kuznetsov, V. V.; Allakhverdiev, S. I. Reactive oxygen species: Re-evaluation of generation, monitoring and role in stress-signaling in phototrophic organisms. *Biochim. Biophys. Acta Bioenerg.* **2014,** *1837*, 835−848.

(15) Buettner, G. R. The spin trapping of superoxide and hydroxyl free radicals with DMPO (5,5-dimethylpyrroline-N-oxide): more about iron. *Free Radic. Res. Commun.* **1993,** *19*, S79−S87.

(16) Finkelstein, E.; Rosen, G. M.; Rauckman, E. J. Spin trapping of superoxide and hydroxyl radical: Practical aspects. *Arch. Biochem. Biophys.* **1980,** *200*, 1−16.

(17) Huang, Z.; Geyer, N.; Werner, P.; de Boor, J.; Gösele, U. Metal-Assisted Chemical Etching of Silicon: A Review. *Adv. Mater.* **2011,** *23*, 285−308.

(18) McIntire, G. L.; Blount, H. N.; Stronks, H. J.; Shetty, R. V.; Janzen, E. G. Spin trapping in electrochemistry. 2. Aqueous and nonaqueous electrochemical characterizations of spin traps. *J. Phys. Chem.* **1980,** *84*, 916−921.

(19) Liu, R.-h.; Fu, S.-y.; Zhan, H.-y.; Lucia, L. A. General Spectroscopic Protocol to Obtain the Concentration of the Superoxide Anion Radical. *Ind. Eng. Chem. Res.* **2009,** *48*, 9331−9334.

(20) Hirshberg, D.; Sharon, D.; Afri, M.; Lavi, R.; Frimer, A. A.; Metoki, N.; Eliaz, N.; Kwak, W.-j.; Sun, Y.-K.; Aurbach, D. Shedding Light on the Oxygen Reduction Reaction Mechanism in Ether-Based Electrolyte Solutions: A Study Using Operando UV–Vis Spectroscopy. *ACS Appl. Mater. Interf.* **2018,** *10*, 10860−10869.

(21). Choi, H. S.; Kim, J. W.; Cha, Y. N.; Kim, C. A quantitative nitroblue tetrazolium assay for determining intracellular superoxide anion production in phagocytic cells. *J. Immunoassay Immunochem.* **2006,** *27*, 31−44.

(22) Griendling, K. K.; Touyz, R. M.; Zweier, J. L.; Dikalov, S.; Chilian, W.; Chen, Y.-R.; Harrison, D. G.; Bhatnagar, A. Measurement of Reactive Oxygen Species, Reactive Nitrogen Species, and Redox-Dependent Signaling in the Cardiovascular System: A Scientific Statement From the American Heart Association. *Circ. Res.* **2016,** *119*, e39−e75.

(23) Beauchamp, C.; Fridovich, I. Superoxide dismutase: Improved assays and an assay applicable to acrylamide gels. *Anal. Biochem.* **1971,** *44*, 276−287.

(24) Vitols, S. E.; Friesen, D. A.; Williams, D. S.; Melamed, D.; Spiro, T. G. Excited State Dynamics of Rh(II) Tetramesityl Porphyrin Monomer from Nanosecond Transient Absorption and Emission Spectroscopy. *J. Phys. Chem.* **1996,** *100*, 207−213.

(25) Sawyer, D. T.; Valentine, J. S. How super is superoxide? *Acc. Chem. Res.* **1981,** *14*, 393−400.

(26) Che, Y.; Tsushima, M.; Matsumoto, F.; Okajima, T.; Tokuda, K.; Ohsaka, T. Water-Induced Disproportionation of Superoxide Ion in Aprotic Solvents. *J. Phys. Chem.* **1996,** *100*, 20134−20137.

(27) Sawyer, D. T.; McDowell, M. S.; Yamaguchi, K. S. Reactivity of perhydroxyl (HOO•) with 1,4-cyclohexadiene (model for allylic groups in biomembranes). *Chem. Res. Toxicol.* **1988,** *1*, 97−100.

(28) Afanas′ev, I. B.; Kuprianova, N. S. Kinetics and mechanism of the reactions of the superoxide ion in solutions. II. The kinetics of protonation of the superoxide ion by water and ethanol. *Int. J. Chem. Kinet.* **1983,** *15*, 1057−1062.

(29) Cofre, P.; Sawyer, D. T. Electrochemical reduction of dioxygen to perhydroxyl (HOO•) in aprotic solvents that contain Broensted acids. *Anal. Chem.* **1986,** *58*, 1057−1062.

Supplementary Information

Chemicals and methods

Chemicals. The commercial reagents used in the various procedures were purchased from Sigma Aldrich, VWR and Fisher Chemicals unless otherwise noted; all chemicals were used as received unless specified. The deionized (DI) water that was used throughout the experiments came from a Millipore Milli-Q Water Purification System. The protonated tetramesityl porphyrin ligand, $(TMP)H_2$, was purchased from Frontier Scientific. Nitroblue tetrazolium (NBT) chloride salt and 5,5-Dimethyl-1-pyrroline N-oxide (DMPO) were purchased from Cayman Chemical. 1,2-difluorobenzene (1,2-DFB) was purchased from Oakwood Chemical. The 1,2-DFB used in the glove box was distilled from CaH_2 and freeze-pump-thawed to remove residual O_2. The 1,2-DFB used in other experiments outside of the glove box was purified with activated 4 Å molecular sieves to remove residual moisture and methanol (CH_3OH) impurities. Tetrabutylammonium perchlorate ($TBAClO_4$), purified by recrystallization in ethanol (C_2H_5OH), was used as the electrolyte in all electrochemical measurements.

Chemical and materials characterizations. Electron paramagnetic resonance (EPR) spectra were recorded on a X-band continuous wave (CW) spectrometer equipped with a 14" Bruker EPR magnet. The X-band CW microwave bridge is composed of a high sensitivity cavity (4119HS-W1). Ultraviolet-visible (UV-Vis) absorption spectroscopy was conducted on an Agilent Technologies Cary 60 spectrometer. Spectra of one-dimensional proton nuclear magnetic resonance (^{1}H NMR) were recorded on a Bruker AV300 (300 MHz) spectrometer. Chemical shifts for protons are reported in parts per million (ppm) and deuterated benzene (C_6D_6) from Cambridge Isotope Laboratories was used as the locking solvent. A gas chromatograph equipped with a mass spectrometer (GC-MS, Agilent Technologies 5975 with Inert XL Selective Detector) was used for

CH_3OH determination and quantification. A Mettler Toledo C20 Coulometric Karl Fischer (KF) Titrator was utilized for the determination of water content in neat 1,2-DFB.

(TMP)Rh−I (Rh^{III}) and (TMP)Rh−CH_3 (Rh^{III}−CH_3). Both syntheses follow procedures published by Wayland et al[30] and were utilized in past work published by our group.[4]

Si wire array. Si nanowire array applied in the bulk electrolysis experiments was prepared following a modified electroless etching recipe based on the works by Huang et al[17] and was utilized in past work published by our group.[4]

Identification and quantification of oxygen reduction species

Spin trap studies for reactive oxygen species detection. DMPO was dissolved in the electrolyte solution, 0.1 M $TBAClO_4$ in 1,2-DFB, to a final concentration of 200 mM and was stored at –30 °C. 3 mg of KO_2 and 15 mg of 18-crown-6 (2:3 equivalents) were dissolved in 20 mL of the electrolyte solution. This solution was diluted 4-fold and stored under argon (Ar) at –30 °C. 500 µL of the DMPO stock solution was mixed with the KO_2 stock solution, while in a tandem experiment it was mixed with cumene hydroperoxide (Figure 3.1). Additionally, both KO_2 and cumene hydroperoxide were mixed together in the same vial (Figure S3.5). In all experiments, the concentration of DMPO was 50 mM; moreover, the concentrations of KO_2 and cumene hydroperoxide were either 500 µM or 1 mM. When DMPO was combined with KO_2, cumene hydroperoxide, or both, the samples were mixed vigorously and immediately frozen under liquid N_2. They were transported frozen to the EPR facility located at the California Institute of Technology where spectra were obtained at room temperature. For observation of the electrochemically generated reactive oxygen species, typical bulk electrolysis experiments were conducted using a Gamry Instruments Interface 1000-E potentiostat with a customized

electrochemical cell (Figure S3.1) which contained 0.1 M $TBAClO_4$ in 1,2-DFB. In the cell was the silicon (Si) nanowire array working electrode (with an average wire length of 15 μm and diameter of 50 nm) (Figure S3.2), Pt wire counter electrode, and a Ag^+/Ag pseudo-reference electrode with a glass frit. A mixture of CH_4 (Airgas, 99.5%) and house air were introduced into the reactor at a fixed ratio of 35 ($P_{CH4}/P_{air} = 35$) under a constant flow rate with the use of mass flow controllers (Omega Engineering, Inc., Model: FMA5502A 0-10 sccm). The bulk electrolysis was conducted under a constant E_{appl} of –1.4 V vs. Saturated Calomel Electrode (SCE). Upon stabilization of the current, DMPO was added into the electrochemical chamber to a final concentration of 50 mM. In a single experiment, samples were taken 5, 15, and 60 min after the addition of DMPO and were immediately frozen under liquid N_2. The samples were transported to the EPR facility under liquid N_2 and EPR spectra were taken at room temperature (Figure S3.4). Additionally, the thawed reaction mixtures were subjected to room temperature conditions for up to 90 min after which a subsequent spectrum was taken (Figure S3.3).

Determining the extinction coefficient of monoformazan generated between NBT and $O_2^{\bullet-}$. The extinction coefficient of monoformazan generated between NBT and $O_2^{\bullet-}$ at 600 nm was determined following a similar protocol reported before.[7] 3 mg of KO_2 and 15 mg of 18-crown-6 (2:3 equivalents) were dissolved in 20 mL of the electrolyte solution. This solution was diluted 4-fold and stored under argon (Ar) at –30 °C. 100 μM NBT, 100 μM Rh^{III}, and varying concentrations of the stock KO_2 solution were mixed in the electrolyte solution, 0.1 M $TBAClO_4$ in 1,2-DFB, and transferred to a quartz cuvette for UV-Vis absorption measurements (Figure S3.7). The absorbance at 600 nm was chosen and used for future experiments as to not interfere with the characteristic absorption and phosphorescence emission of Rh^{III} (Figure S3.7). The extinction coefficient of NBT in 1,2-DFB at 600 nm, ε_{600nm}, was identified in order to quantify the superoxide

($O_2^{\bullet-}$) concentration. 500 μL of the KO_2 stock solution was mixed with varying concentrations of NBT and diluted with the electrolyte solution to a final volume of 2 mL. The reaction between KO_2 and NBT was allowed to progress overnight to ensure completion and then UV-Vis absorption spectra were obtained. The ε_{600nm} was found to be 4327 $M^{-1}\cdot cm^{-1}$ (Figure 3.2B).

Constant potential electrolysis with NBT for $O_2^{\bullet-}$ quantification. All electrochemical tests were performed using a Gamry Instruments Interface 1000-E potentiostat. In an Ar-filled glovebox, cyclic voltammetry (CV) (Figure S3.6) and bulk electrolysis experiments (Figure 3.2A) were performed on a 500 μM NBT solution in a glass vial equipped with a Teflon top fitted with electrode and gas inlet/outlet ports. The cell contained 0.1 M $TBAClO_4$ in 1,2-DFB with a Pt wire counter electrode, a Ag^+/Ag pseudo-reference electrode with a glass frit, and a 3 mm diameter glassy carbon working electrode. The bulk electrolysis was conducted with flowing inert gas under constant convection and a constant E_{appl} of –1.4 V vs. SCE. The sampling electrolysis experiments were conducted in the customized three-electrode electrochemical reactor with gas inlet/outlet ports as pictured in Figure S1. In a typical experiment, the electrochemical cell contains 100 μM NBT dissolved in the electrolyte solution, 0.1 M $TBAClO_4$ in 1,2-DFB. The working electrode was a Si nanowire array with an average wire length of 15 μm and diameter of 50 nm.[3] The other electrodes included a Pt wire as the counter electrode and a Ag^+/Ag pseudo-reference electrode with a glass frit. The bulk electrolysis was conducted under a constant E_{appl} of –1.4 V vs. SCE. A mixture of CH_4 (Airgas, 99.5%) and house air were introduced into the reactor such that P_{CH4}/P_{air} = 35. In conjunction, control experiments were conducted with flowing N_2 in place of CH_4 at the same constant ratio of 35. For the sampling experiments, 200 μL samples were taken every 3 min, diluted 10-fold with 100 μM NBT solution, and their UV-Vis absorption at 600 nm was measured upon sampling (Figures 3.2C and 3.2D). Additionally, samples were taken before and after the 3

h bulk electrolysis with Rh^{III}, CH_4, and NBT, and were analyzed via GC-MS to observe CH_3OH generation. The reported data are after *iR* correction. Cyclic voltammograms of decamethylferrocene were also conducted to calibrate the potentials of Ag^+/Ag pseudo-reference electrode, based on the reported standard potential of decamethylferrocene (−0.059 V vs. SCE).[31]

Determination of $O_2^{\bullet-}$ formation rate $\partial Y_{ROS}/\partial t$. The concentration of $O_2^{\bullet-}$ generated during the sampling electrolysis experiments was quantified through its reaction with NBT via UV-Vis spectroscopy. As the absorption at 600 nm eventually plateaued over time (Figures 3.2C and 3.2D), that was taken as the steady-state $O_2^{\bullet-}$ concentration. Thus, the absorption at 600 nm was converted to the amount of $O_2^{\bullet-}$ by way of the experimentally determined ε_{600nm} of 4321 $M^{-1} \cdot cm^{-1}$ and the stoichiometry of the reaction between $O_2^{\bullet-}$ and NBT (2:1 equivalent ratio)[19], before being normalized by the average current. The rate of formation of $O_2^{\bullet-}$ during electrolysis measurements was identified as the slope of the line before the steady-state was reached (0–30 min). The slope of equivalent trials was averaged and ultimately, this value was taken as the rate of formation.

Karl Fischer titration. The amount of water impurities in neat 1,2-DFB was quantified via a Mettler Toledo C20 Coulometric Karl Fischer Titrator. Neat 1,2-DFB was injected into the Karl Fischer solution at volumes of 0.3, 0.5 and 1.0 mL. Each volume injected was replicated 6 times to minimize the standard deviation and overall error. The average water content in the 1,2-DFB was found to be 92.2±5.7 ppm (or 5.1±0.3 mM).

Reactivity between Rh^{III}–CH_3 and ROS

Stoichiometric reactions between Rh^{III}–CH_3 and different ROS species were performed and monitored by ^1H NMR. In one example, 0.25 mM Rh^{III}–CH_3 and 0.25 mM *t*-butyl hydroperoxide were mixed in 1,2-DFB for 6 h at room temperature. The ^1H NMR spectra in C_6D_6 indicate the

formation of CH_3OH at the expense of the axial methyl group of $Rh^{III}–CH_3$. Similar results were also obtained with cumene hydroperoxide in decane, 2-(1- hydroperoxy-1-methoxyethyl)-5-methylcyclohexan-1-ol in 1,2-DFB, and KO_2 in "wet" 1,2-DFB. Reactions between 1 mM $Rh^{III}–CH_3$ and KO_2 in strictly dry 1,2-DFB did not yield any observable formation of CH_3OH up to 48 h at room temperature.

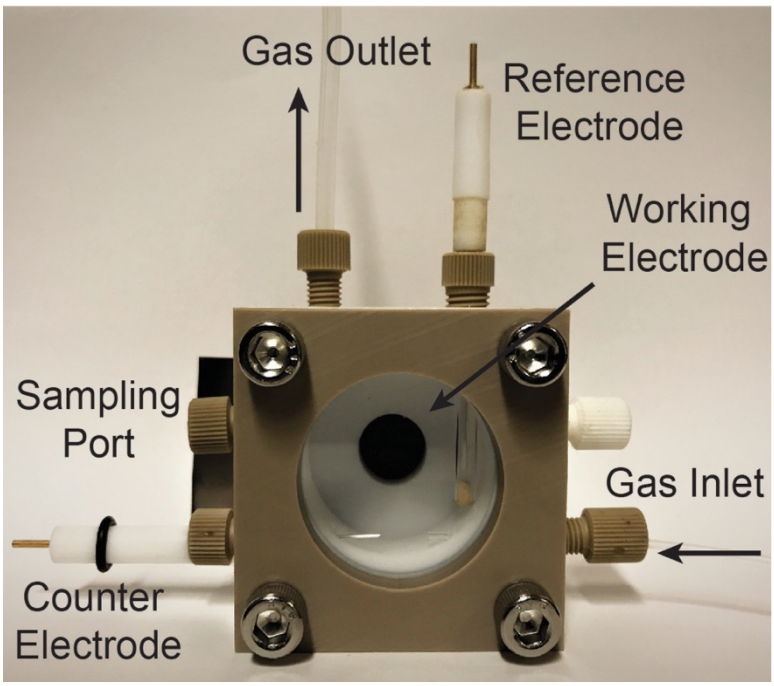

Figure S3.1. Photograph of the customized electrochemical reactor used for bulk electrolysis.

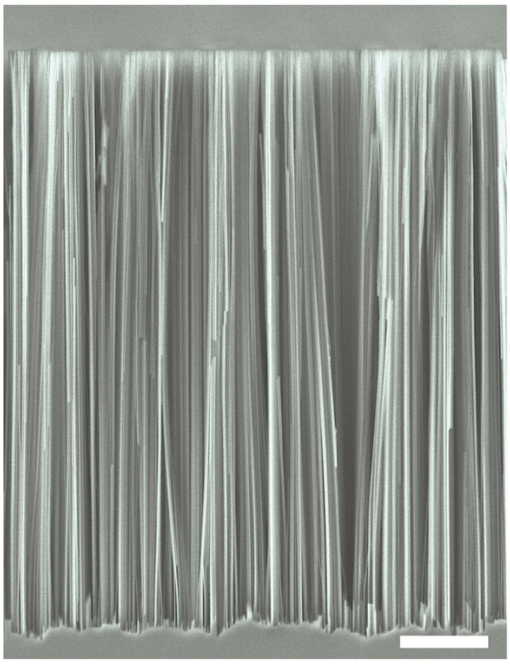

Figure S3.2. Scanning electron microscopy image of silicon nanowire array with length of 15 μm and diameter of 50 nm. Scale bar, 2 μm.

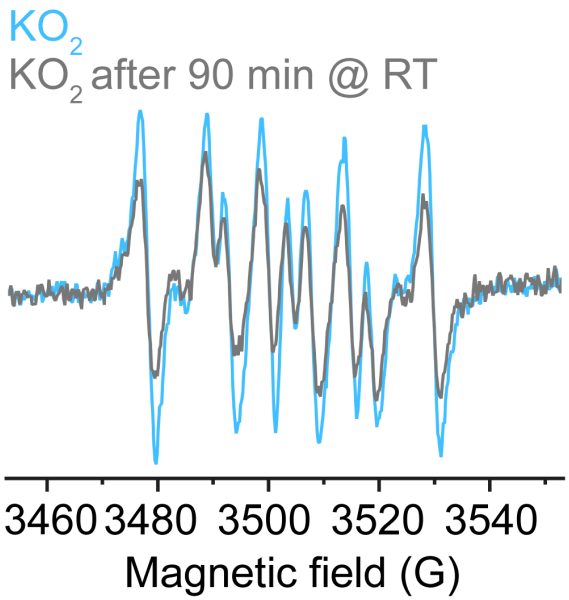

Figure S3.3. Electron paramagnetic resonance spectra depicting the adducts formed upon the reaction of 50 mM DMPO (5,5-dimethyl-1-pyrroline N-oxide) and 1 mM KO_2 (potassium dioxide) after immediate thawing (light blue trace) and the same reaction mixture after 90 min at room temperature, RT (silver trace); 0.1 M $TBAClO_4$ (tetrabutylammonium perchlorate) in 1,2-DFB (1,2 difluorobenzene).

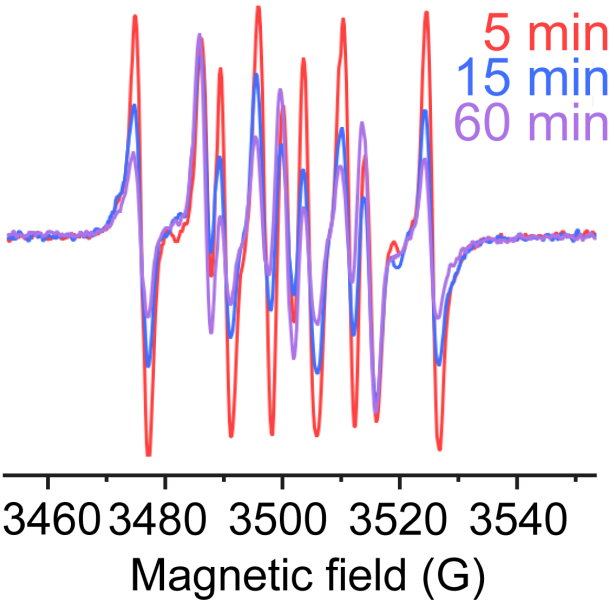

Figure S3.4. Electron paramagnetic resonance spectra depicting the adducts formed upon the addition of 50 mM DMPO (5,5-dimethyl-1-pyrroline N-oxide) to the constant potential electrolysis; samples were taken 5 min (red curve), 15 min (blue curve), and 60 min (purple curve) after the addition of 50 mM DMPO; 1 mM Rh^{III} in the electrolyte solution, 0.1 M $TBAClO_4$ (tetrabutylammonium perchlorate) in 1,2-DFB (1,2 difluorobenzene); constant reduction potential of –1.4 V vs. SCE was applied to the Si nanowire working electrode; a mixture of CH_4 and air were flowed into the customized electrochemical reactor (Figure S3.1) at a defined ratio of 35 ($P_{CH4}/P_{air} = 35$) under ambient pressure.

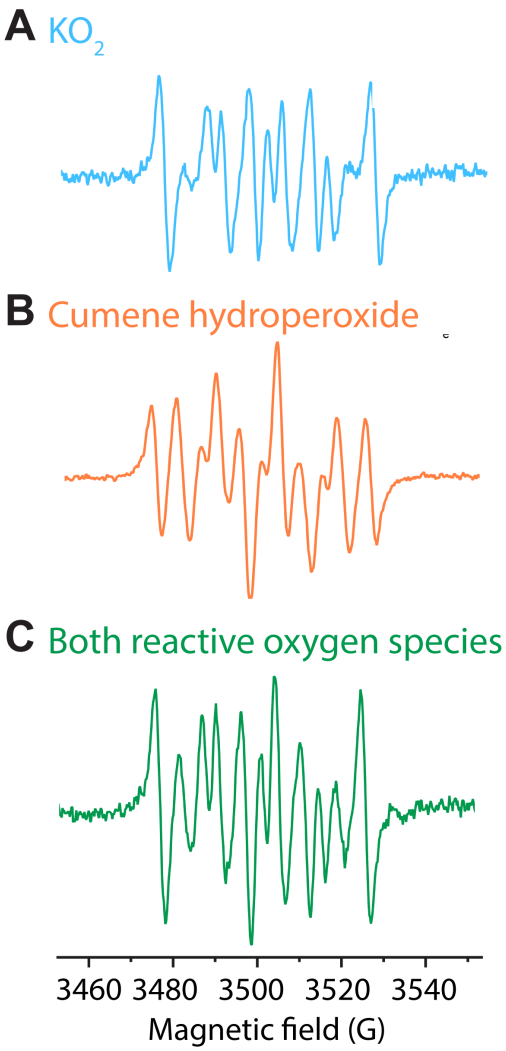

Figure S3.5. Electron paramagnetic resonance spectra depicting the adducts formed upon the reaction of 50 mM DMPO (5,5-dimethyl-1-pyrroline N-oxide) and (**A**) 500 µM KO_2 (potassium dioxide) (**B**) 500 µM cumene hydroperoxide (2-hydroperoxypropan-2-ylbenzene) and (**C**) both 500 µM KO_2 and 500 µM cumene hydroperoxide in the electrolyte solution, 0.1 M $TBAClO_4$ (tetrabutylammonium perchlorate) in 1,2-DFB (1,2 difluorobenzene).

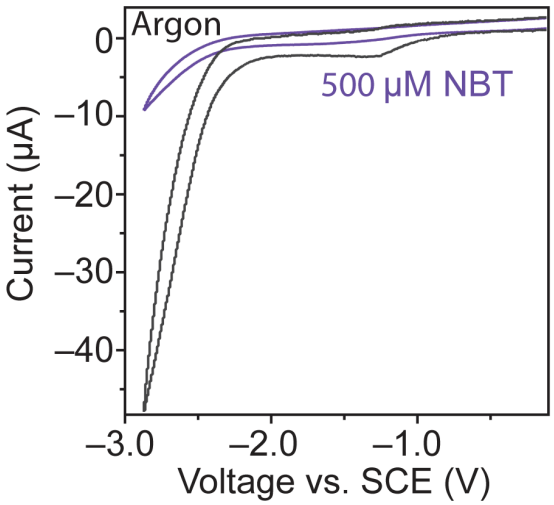

Figure S3.6. Cyclic voltammograms on a glassy carbon electrode under argon environment. Dark gray trace, blank without the addition of NBT (nitroblue tetrazolium); purple trace, 500 µM NBT; 0.1 M $TBAClO_4$ (tetrabutylammonium perchlorate) in 1,2-DFB (1,2 difluorobenzene), 100 mV/s.

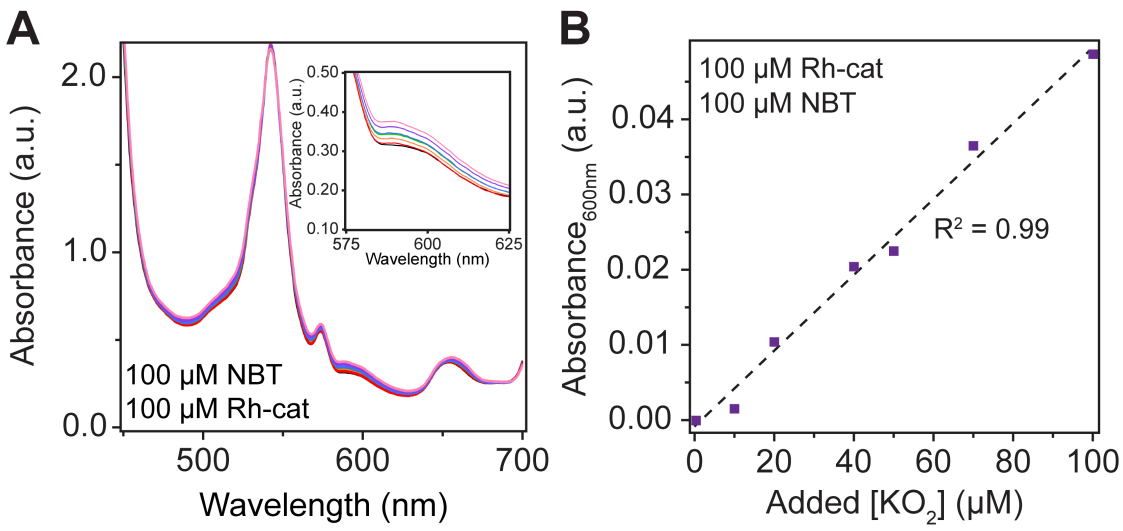

Figure S3.7. (**A**) Ultraviolet-visible absorption spectrum monitoring the reaction product of 100 µM NBT (nitroblue tetrazolium) with varying concentrations of added KO_2 (potassium dioxide) in the presence of 100 µM Rh-cat (Rh^{III}, (TMP)Rh–I); 0 µM KO_2 (black), 10 µM KO_2 (red), 20 µM KO_2 (orange), 40 µM KO_2 (green), 50 µM KO_2 (blue), 70 µM KO_2 (purple), 100 µM KO_2 (pink). (**B**) Beer's Law curve illustrating the reaction product at 600 nm of 100 µM NBT as a function of KO_2 concentration with 100 µM Rh-cat.

Supplementary References

(30) Wayland, B. B.; Ba, S.; Sherry, A. E. Activation of methane and toluene by rhodium(II) porphyrin complexes. *J. Am. Chem. Soc.* **1991**, *113*, 5305−5311.

(31) O'Toole, T. R.; Younathan, J. N.; Sullivan, B. P.; Meyer, T. J. 1,2-Difluorobenzene: a relatively inert and noncoordinating solvent for electrochemical studies on transition-metal complexes. *Inorg. Chem.* **1989,** *28*, 3923−3926.

Chapter 4. Compartmentalization of O_2-sensitive Rh^{II} metalloradical within nanowire array electrode enables ambient CH_4 activation

This chapter is a version of Natinsky, B. S.; Jolly, B. J.; Dumas, D. M.; Liu, C. "Efficacy analysis of compartmentalization for ambient CH_4 activation mediated by Rh^{II} metalloradical in nanowire array electrode." *Chemical Science*. **2021**, *12*, 1818–1825.

Abstract

Compartmentalization is a viable approach of ensuring the turnover of a solution cascade reaction with ephemeral intermediates, which may otherwise deactivate in the bulk solution. In biochemistry or enzyme-relevant cascade reactions, extensive models have been constructed to quantitatively analyze the efficacy of compartmentalization. Nonetheless, the application of compartmentalization and its quantitative analysis in non-biochemical reactions is seldomly performed, leaving much uncertainty about whether compartmentalization remains effective for non-biochemical, such as organometallic, cascade reactions. Here, we report our exemplary efficacy analysis of compartmentalization in our previously reported cascade reaction for ambient CH_4-to-CH_3OH conversion, mediated by an O_2-deactivating Rh^{II} metalloradical with O_2 as the terminal oxidant in the Si nanowire array electrode. We experimentally identified and quantified the productivity of key reaction intermediates, including Rh^{II} metalloradical and reactive oxygen species (ROS) from O_2 (Chapter 3). Based on such findings, we experimentally determined that the nanowire array enables about 81 % of the generated ephemeral intermediate in air, Rh^{II} metalloradical, to be utilized towards CH_3OH formation, which is 0% in homogenous solution. Such an experimentally determined value was satisfactorily consistent with the results from our semi-quantitative kinetic model. The consistency suggests that the reported CH_4-to-CH_3OH

conversion surprisingly possesses minimal unforeseen side reactions, and is favorably efficient as a compartmentalized cascade reaction. Our quantitative evaluation of the reaction efficacy offers design insights and caveats into application of nanomaterials to achieve a spatially controlled organometallic cascade reactions.

Introduction

Compartmentalization, ubiquitous in biology, allows efficient transfer of reaction intermediary or ephemeral species within a multienzyme cascade reaction in the intracellular medium.[1-3] By segregating subsequent catalytic sites from the bulk environment at microscopic or even nanoscopic level, spatial control of catalytic reactions ensures the functionality of biological metabolism in a factory-like manner with high efficiency.[4-6] Here the key to a successful compartmentalized cascade reaction is the capability of confining a transient intermediate within the compartment and preventing its outflux that leads to either intermediate's loss or deactivation (Figure 4.1A). A number of theoretical models have been established to evaluate the capability of compartmentalized cascade reactions in fulfilling this task[7, 8], predominantly in the context of enzymatic catalytic reactions.[9-13] Reaction efficiency (γ), defined as the ratio between the product outflux and the substrate influx to the compartment for a one-to-one stoichiometric reaction (Figure 4.1A), quantitatively measures the efficacy of a cascade system in retaining and utilizing the intermediate species generated within the compartment.[6, 9, 14, 15] With the value of γ commonly approaching unity for cascade reactions in biology,[4-6, 14] nature masters the design strategy of compartmentalization for enzymatic reactions.

The benefits of confining catalytic reactions spatially at microscopic and nanoscopic level in nature inspire the development of other non-enzymatic cascades, mostly with surface-attached molecular,

nanoparticle, or enzyme catalysts in porous medium such as metal-organic frameworks[16-18] or superposed on scaffolds[10-12]. Nonetheless, analyzing and determining the value of γ, a quantitative figure-of-merit for the efficacy of compartmentalization, remains infrequent, to say the least, for non-enzymatic scenarios. As resonated in recent publications[9, 16, 19], the scarcity of experimentally determined γ values casts uncertainty about the effectiveness of a certain design strategy of compartmentalization. A synergistic study comparing experimentally determined γ values with the one from a theoretical model will offer valuable insights whether the designed cascade reaction is effective without undesirable side effects, ascertain the merits of designed compartmentalization, and further justify the design strategy of non-enzymatic compartmentalized systems. This research report aims to offer an exemplary case of such study for organometallic catalysis with compartmentalized systems.

We are interested in employing microscopic concentration gradients within nanomaterials to design organometallic catalytic cycles of seemingly incompatible steps, in which key reaction intermediates will be quickly deactivated once they diffuse out of the nanomaterials. In our previous report[20], a cascade catalysis with O_2-sensitive reaction intermediate was established to achieve ambient CH_4-to-CH_3OH conversion with O_2 as the terminal oxidant assisted with electricity. As shown in Figure 4.1B, the nanowire array electrode electrochemically reduces rhodium (III) tetramesityl porphyrin iodide (Rh^{III}) into rhodium (II) tetramesityl porphyrin metalloradical (Rh^{II}) in aprotic solvent 1,2-difluorobenzene (1,2-DFB). At the same time, the nanowire array reduces O_2 into reactive oxygen species (ROS) and creates a sharp O_2 concentration gradient with a locally O_2-free environment near the bottom of nanowire array in aerobic conditions. In the O_2-free microenvironment, two equivalents of the generated Rh^{II} species, while highly reactive with O_2[21], activate one equivalent of CH_4 ambiently to yield methylated rhodium

(III) tetramesityl porphyrin (Rh^{III}–CH_3) and rhodium (III) tetramesityl porphyrin hydride (Rh^{III}–H). Both species are proposed to react with the generated ROS that remain to be further identified (vide infra), leading to the formation of CH_3OH. While no barrier is present to physically separate the liquid phase within the nanowire array from the bulk solution, the whole system can be considered as a compartmentalized cascade with the nanowire array as the compartment with its unique microenvironment (Figure 4.1C), analogous to the previous argument in the case of two-enzyme cascades in which enzymes are placed in close proximity at nano-scale.[12, 22] The overall process was reported to be catalytic, achieving a turnover number up to 52,000 within 24 hours.[20] The synergy between nanomaterials and organometallic chemistry warrants a new catalytic route of CH_4 functionalization, while additional study is needed to understand the underlying mechanism and quantitatively evaluate the efficacy of the strategy that interfaces nanowires with organometallics.[23]

Here we report our analysis of the above-mentioned CH_4-to-CH_3OH catalysis in the context of a compartmentalized cascade. We translated the reported catalytic system into a theoretical model that estimates the numerical value of γ. Electron paramagnetic resonance (EPR) spectroscopy with a spin-trap agent, along with other characterizations, unraveled that the predominant ROS present in the system is superoxide and illustrated its role in CH_3OH formation (Chapter 3). This piece of mechanistic insight allowed us to subsequently determine the value of γ in the catalysis, which surprisingly amounts to more than 80%. The high value of measured γ is consistent with our theoretical framework and illustrates the efficacy of the created nanoscopic concentration gradient with minimal side reactions. Our results demonstrate that carefully designed compartmentalization, spatially controlling the occurrence of organometallic reactions in solution

at microscopic length scale, can circumvent undesirable reactions efficiently and create organometallic catalytic cycles impossible in homogenous solution.

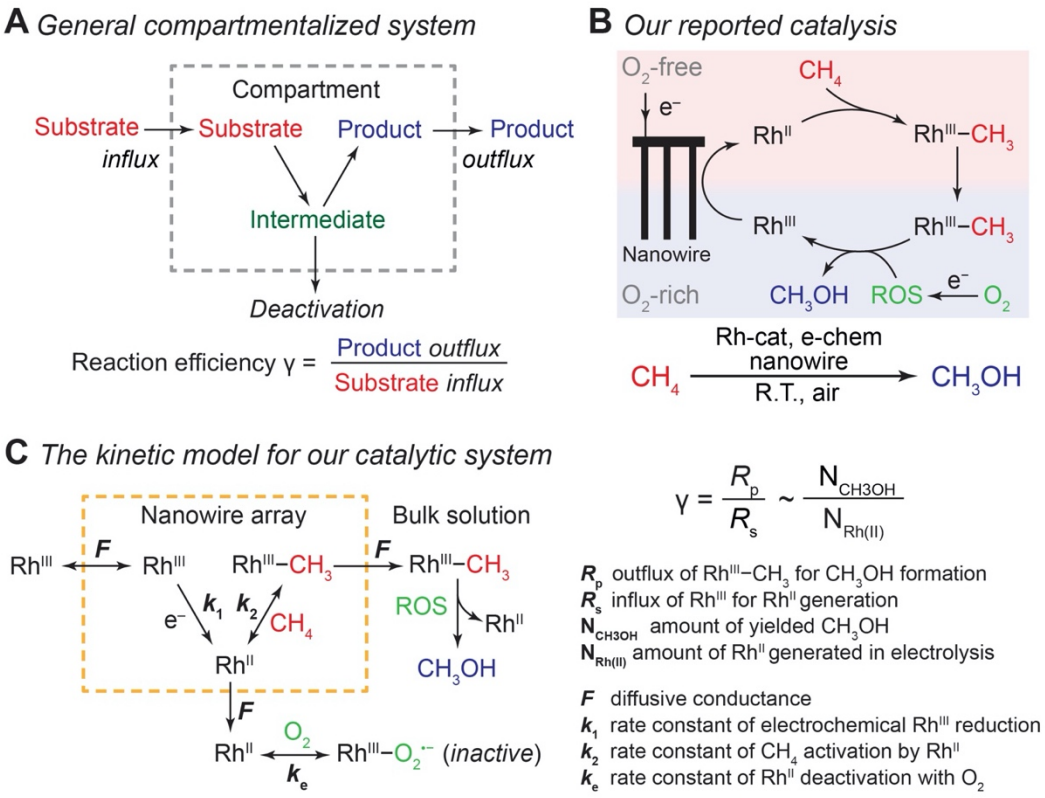

Figure 4.1. Reaction efficiency γ in compartmentalized cascade reactions. (**A**) A generalized schematic for compartmentalization cascade. (**B**) The proposed mechanism of our previously reported system for ambient CH_4-to-CH_3OH conversion.[20] Rh^{III}, rhodium (III) tetramesityl porphyrin iodide; Rh^{II}, rhodium (II) tetramesityl porphyrin metalloradical; Rh^{III}–CH_3, methylated rhodium (III) tetramesityl porphyrin; ROS, reactive oxygen species; Rh-cat, rhodium (III) tetramesityl porphyrin iodide; e-chem, electrochemistry; R.T., room temperature. (**C**) A theoretical framework of kinetic model for the CH_4-to-CH_3OH system in the context of compartmentalization cascade.

Results and Discussion

A theoretical framework of cascade reactions in nanowire array electrode

Generally applicable for non-enzymatic cascade design as noted above, one question that we ask is whether our previously reported design employing the nanowire array and a concentration gradient is effective in utilizing the ephemeral O_2-sensitive intermediate, Rh^{II}, whose activation of CH_4 was considered turnover-limiting.[20, 24] Our approach to this question is to construct a numerical model in the context of compartmentalization and analyze the reaction efficiency γ that will be valuable for future design consideration. Figure 4.1C displays the reported reaction in the context of compartmentalized cascade reactions. Here the compartment, schematically shown as a yellow-colored dashed box, is defined as the O_2-free liquid phase within the nanowire array where Rh^{II}-initiated CH_4 activation is proposed to take place. Following its definition[9, 15], γ is expressed as the ratio between the outward flux of Rh^{III}–CH_3 for CH_3OH formation (R_p) and the rate of Rh^{II} generation (R_s) during the electrolysis. Based on the proposed reaction mechanism (Figure 4.1B and 4.1C), R_p and R_s are dictated by the kinetic rate constant of electrochemical reduction of Rh^{III} into Rh^{II} (k_1) as well as the Rh^{II}-initiated CH_4 activation (k_2), respectively. We note that γ could also be interpreted as the competition between the rate of CH_4 activation (R_p) in the compartment and the deactivation of Rh^{II} with O_2 in the bulk, whose rate constant is denoted as k_e. Because such a competition depends on the diffusive mass transport at steady state, another important factor is the diffusive conductance F, as used in the design of enzymatic cascades[6, 9, 13], which describes the rate of mass transport for chemical species crossing into and out of the compartment boundary. However, in order to obtain the flux of a particular species in and out of the compartment, F must be normalized to the volume of the compartment V and Avogadro's number N_A.[9] We anticipate that F and V will be co-dependent, therefore we derive an expression for $F/(VN_A)$, denoted F_V, in terms of the nanowire geometry (see Supplementary Information for full derivations). Since the

Rh^{II}, Rh^{III}, and Rh^{III}–CH_3 species share the bulky metalloporphyrin structure, as a first-order approximation F_V is assumed to be the same among Rh^{II}, Rh^{III}, and Rh^{III}–CH_3, and only dependent on the morphology of the nanowire array. Assuming $k_e \rightarrow \infty$ due to the reported rapid deactivation[21], we incorporated the above-mentioned components and derived a numerical model, which describes γ in a compartmentalized cascade as shown below:

$$\gamma = \frac{R_p}{R_s} = \frac{k_1 F_V C_{Rh,total}}{k_2 (F_V + k_1)[Rh^{II}]^2 C_{CH_4}} \tag{4.1}$$

$$F_V \approx \frac{8D}{L^2} \tag{4.2}$$

Here $C_{Rh,total}$ is the total concentration of Rh species in the bulk solution, almost exclusively in the form of Rh^{III}; $[Rh^{II}]$ the steady-state concentration of Rh^{II} in the compartment during electrolysis that remains to be numerically calculated; C_{CH_4} the concentration of CH_4 in the bulk solution; D the diffusion coefficient of the Rh species; and L the length of the nanowire array. Similarly, we derived the expression of γ in the non-compartmentalized homogenous solution (see Supplementary Information for full derivations). After solving the steady-state kinetic equations that include the mass transport across the compartment, we further derived the expressions of γ from equation (4.1) for the nanowire array electrode:

$$\gamma = \frac{(F_V + k_1)\left(-F_V + \sqrt{{F_V}^2 + \frac{4F_V k_1 k_2 C_{CH_4} C_{Rh,total}}{F_V + k_1}}\right)^2}{4F_V k_1 k_2 C_{CH_4} C_{Rh,total}} \tag{4.3}$$

And the expressions of γ in a homogenous solution:

$$\gamma' = \frac{\left(-k_e + \sqrt{k_e^2 + 4k_1k_2C_{CH_4}C_{Rh,total}}\right)^2}{4k_1k_2C_{CH_4}C_{Rh,total}} \quad (4)$$

We note that k_e is explicitly incorporated in equation (4) while we assumed $k_e \rightarrow \infty$ in equation (4.3). The above equations establish the theoretical framework for us to analyze the efficacy of the organometallic reactions in the nanowire array electrode.

The established theoretical model demands input from experimental results. Because of the high reactivity between Rh^{II} and O_2 outside of the O_2-free microenvironment in the nanowire array[21], i.e. $k_e \rightarrow \infty$, γ can be approximated as the ratio between the amount of generated CH_3OH (N_{CH3OH}) and Rh^{II} from electrochemical reduction of Rh^{III} ($N_{Rh(II)}$) (Figure 4.1C), if we presume that the conversion from Rh^{III}–CH_3 to CH_3OH is stoichiometric as corroborated by our prior experimental evidence.[20] While N_{CH3OH} is experimentally readily measurable as we have done before[20], the value of $N_{Rh(II)}$ is less accessible and requires the quantification of ROS because the electrochemical reduction of Rh^{III} into Rh^{II} is concurrent with the electrochemical reduction of O_2 into ROS (Figure 4.1B). Therefore, the identification and quantification of the ROS that was performed in Chapter 3 not only allowed for deeper insights about the chemical steps involved in the catalysis but also will provide a quantitative determination of γ.

Experimental determination and analysis of reaction efficiency γ

Our successful quantification of the electrochemical ROS generation rate ($\partial Y_{ROS}/\partial t$) (Chapter 3) led to an experimentally determined value of reaction efficiency γ. As the reductive current is responsible for the generation of both ROS and CH_4-activating Rh^{II}, the equation for γ in Figure 4.1C can be written as:

$$\gamma = \frac{R_p}{R_s} \sim \frac{N_{CH3OH}}{N_{Rh(II)}} = \frac{N_{CH3OH}}{\int Idt - \int IF_{Faradaic} V \frac{\partial Y_{ROS}}{\partial t} dt} \tag{4.5}$$

Here I denotes the electric current, $F_{Faradaic}$ the Faradaic constant, and V the volume of electrochemical reactor. Equation (4.5) leads to γ = 81% for a 3-hr electrolysis of CH_4 activation, based on the results of our previous report[20] and the value of Y_{ROS} determined in Figure 3.2 in Chapter 3. The experimentally determined value of γ is relatively close to unity, suggesting that a large portion of the generation Rh^{II} activates CH_4 before diffusing out the nanowire array despite the high reactivity between Rh^{II} and O_2 (Figure 3.2C).

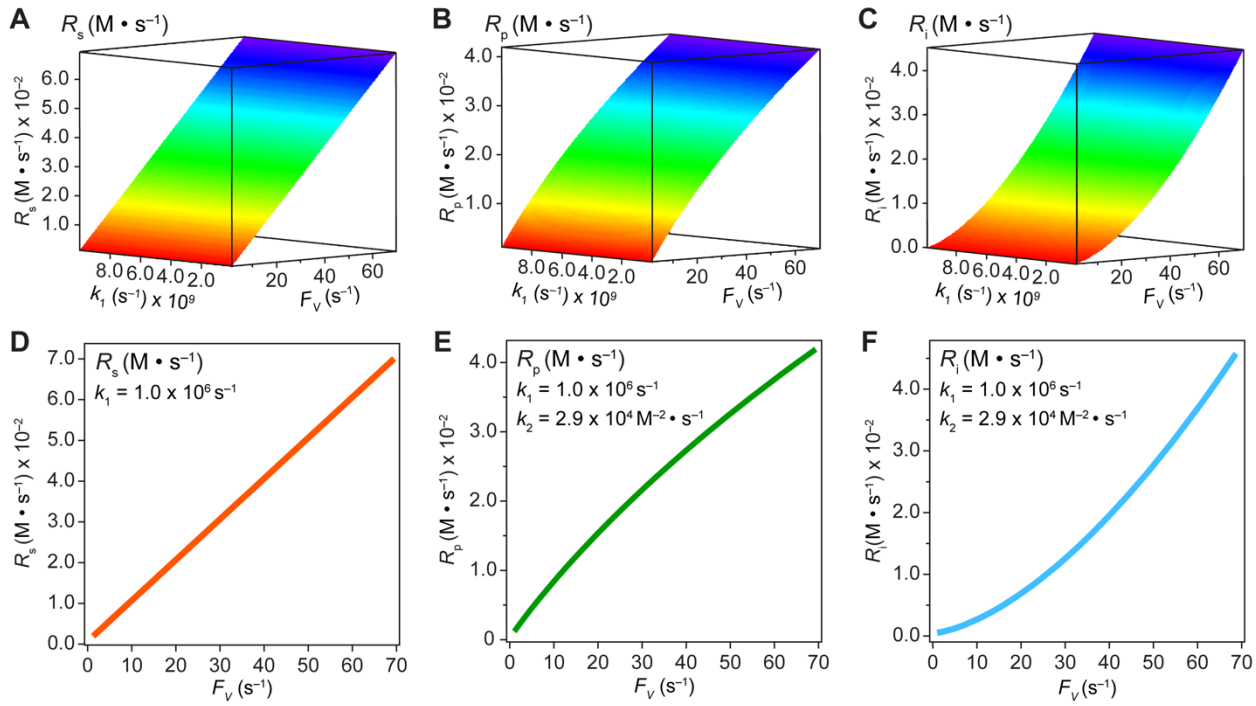

Figure 4.2. Graphical representations of substrate conversion (R_s), product formation (R_p), and intermediate outflux (R_i) in the compartmentalized system. Panels (**A**), (**B**), and (**C**) represent R_s, R_p, and R_i, respectively, as a function of both F_V and k_1. Panels (**D**), (**E**), and (**F**) represent R_s, R_p, and R_i, respectively, as a function of F_V for a constant value of k_1 (1.0 ×10^6 s^{-1}). k_2 was

experimentally determined to be 2.9×10^4 $M^{-2}\bullet s^{-1}$ within the nanowire array in our previous report.[20]

In an effort to compare our experimentally determined γ values with the theoretical maximum, we numerically calculated the values of γ based on the established theoretical framework for a nanowire-based compartmentalization. Following the model displayed in Figure 4.1C, the calculated values of R_s (Figure 4.2A and 4.2D), R_p (Figure 4.2B and 4.2E), and the Rh^{II} flux diffusing out of the compartment R_i (Figure 4.2C and 4.2F) were displayed as a function of k_1 and F_V. Those calculations use $k_e \rightarrow \infty, me$ for Rh^{II}-initiated CH_4 activation within the nanowire array as determined in our previous report.[20] Because the rate of electrochemical reduction of Rh^{III} (k_1) was not readily determinable in our system, k_1 was assigned as a range of values spanning four orders of magnitude (10^6–10^{10} s^{-1}) based on a typical range reported for electron transfer of metalloporphyrin complexes in literature.[25] Nonetheless, Figure 4.2 shows that the effect of compartmentalization is not sensitive to the value of k_1, evident as the k_1 term cancels out in Equations S4.14, S4.18, and S4.19 during the derivation as long as k_1 is sufficiently large ($\geq 10^6$ s^{-1}) to the value of F_V, with an increased F_V value leading to increase fluxes both outward and inward of the compartment. Because the value of F_V is dependent on the nanowire array's morphology, such a trend suggests that we can control and possibly optimize the mass transport across the compartment by controlling the length L of nanowire array based on equation (4.2).

A comparison between the experimental value of γ with simulation results suggests that the Rh-based organometallic catalysis enabled by nanowire array is indeed functioning near its theoretical limit. Given the strong dependence on the value of F_V for R_s, R_p, and R_i, we envisioned that γ is mostly a function of F_V, whose relationship is displayed as the red trace in Figure 4.3. While R_s,

R_p, and R_i all increase with larger values of F_V (vide supra), overall a larger F_V value tends to decrease the value of γ (Figure 4.3). Such a trend is corroborated with our previous observation that nanowire array of longer length L, hence smaller F_V value based on equation (4.2), corresponds to a larger yield of CH_3OH before mass transport becomes rate-limiting.[20] One thing to note is that this theoretical framework does not account for those Rh^{III} molecules that enter and leave the nanowire compartment without undergoing the initial electrochemical reduction reaction. However, the alignment of the experimental and theoretical values indicate that this phenomenon remains minimal in our system, but it cannot be excluded completely. In comparison, the value of γ for a non-compartmentalized scenario, *i.e.* homogenous solution without nanostructured electrode, is also shown as the black trace in Figure 4.3. A clear difference is observable as the value of γ for the non-compartmentalized scenario is virtually near zero (at most 0.001% indeed), in line with our previous experimental work that utilized a planar electrode surface and resulted in no CH_3OH generation.[20] We also positioned our experimentally determined γ value in Figure 4.3, after we determinized $F_V = 20.\ s^{-1}$ given $L = 15\ \mu m$ and $D = 5.6 \times 10^{-10}\ m^2 \bullet s^{-1}$ in 1,2-DFB as measured before.[20] The error bar in Figure 4.3 represents the approximation incurred when deriving the expression for F_V (Equation 4.2). A good agreement between the experimental and theoretical values of γ for the nanocompartment was observed (Figure 4.3), yet the slightly higher value of experimentally derived γ might originate from the underestimation of $\partial Y_{ROS}/\partial t$ calculated in Chapter 3. The agreement indicates that minimal unforeseen side reactions, if any, are present in the catalyst system and the proposed benefit of a nanowire-generated O_2-free microenvironment for Rh^{II}-initiated CH_4 activation is well demonstrated.

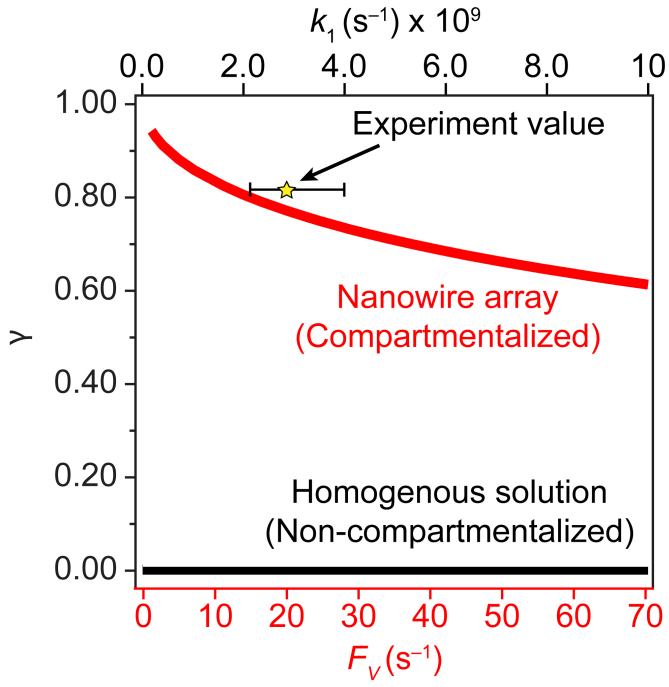

Figure 4.3. Reaction efficiency γ plotted as a function of diffusive conductance F_V for the scenarios with nanowire-enabled compartmentalization (red trace) and γ plotted as a function of k_1 without nanowire-enabled compartmentalization (black trace). The experimentally determined data point of γ for nanowire array of 15 μm length is represented by the star. The error bar presents the approximation when deriving the experimental value of F_V (see Supplementary Information for full derivations).

Additional design insights are available from our results. We examined the dependence of γ under different hypothetical values of CH_4-acitvation rate constant k_2. Smaller values of k_2 significantly lowers γ, *i.e.* the efficiency of compartmentalization created by the nanowire array (Figure S4.1). Such a trend is reasonable since a lower value of k_2 will lead to more prominent outward flux R_i of the unreacted Rh^{II} species which will introduce a larger percentage of undesirable Rh^{II} deactivation. Therefore, while our Rh-based catalysis demonstrates the benefits of compartmentalization by constructing a catalytic cycle of seemingly incompatible steps for

organometallics, we caution that the efficacy of this strategy depends on the specific chemical system under consideration. As the value of γ depends on F_V and thus the nanostructure's morphology, such as nanowire length L in our case, there exists an optimal morphology of nanostructures for specific organometallic compounds' reactivities in order to create an effective microenvironment and efficient cascade reactions with minimal detrimental deactivation. A quantitative evaluation of reaction efficiency γ, however estimated, is recommended in order to justify the introduction of nanostructures and a micro-environment. A general numerical design framework of nanostructures for a typical organometallic catalytic cycle that includes oxidative addition and reductive elimination is currently being developed in the authors' laboratory.

Conclusion

In this work, we applied the concept of reaction efficiency γ in biochemical cascades to quantitatively evaluate the efficacy of compartmentalization for organometallic reactions with the use of nanowire array electrodes. A high γ value approaching unity, the theoretical limit, was experimentally observed, suggesting minimal detrimental side reactions. This observation indicates that with proper design it is possible to employ nanomaterials to spatially control organometallic reactions and achieve efficient cascade with ephemeral intermediates, analogous to the biological counterparts with near-unity γ values. This work quantitatively highlights the transformative power of spatial control at the nanoscale for new chemical reactivity.

References

(1) Shi, J.; Wu, Y.; Zhang, S.; Tian, Y.; Yang, D.; Jiang, Z. Bioinspired construction of multi-enzyme catalytic systems. *Chem. Soc. Rev.* **2018,** *47*, 4295−4313.

(2) Vázquez-González, M.; Wang, C.; Willner, I. Biocatalytic cascades operating on macromolecular scaffolds and in confined environments. *Nat. Catal.* **2020,** *3*, 256−273.

(3) Trantidou, T.; Friddin, M.; Elani, Y.; Brooks, N. J.; Law, R. V.; Seddon, J. M.; Ces, O. Engineering Compartmentalized Biomimetic Micro- and Nanocontainers. *ACS Nano* **2017,** *11*, 6549−6565.

(4) Tu, Y.; Peng, F.; Adawy, A.; Men, Y.; Abdelmohsen, L. K. E. A.; Wilson, D. A. Mimicking the Cell: Bio-Inspired Functions of Supramolecular Assemblies. *Chem. Rev.* **2016,** *116*, 2023−2078.

(5) Lin, J.-L.; Palomec, L.; Wheeldon, I. Design and Analysis of Enhanced Catalysis in Scaffolded Multienzyme Cascade Reactions. *ACS Catal.* **2014,** *4*, 505−511.

(6) Hinzpeter, F.; Gerland, U.; Tostevin, F. Optimal Compartmentalization Strategies for Metabolic Microcompartments. *Biophys. J.* **2017,** *112*, 767−779.

(7) Weisz, P. B. Diffusion and Chemical Transformation. *Science* **1973,** *179*, 433−440.

(8) Weisz, P. B. Stepwise Reaction via Intermediates on Separate Catalytic Centers. *Science* **1956,** *123*, 887−888.

(9) Tsitkov, S.; Hess, H. Design Principles for a Compartmentalized Enzyme Cascade Reaction. *ACS Catal.* **2019,** *9*, 2432−2439.

(10) Wilner, O. I.; Weizmann, Y.; Gill, R.; Lioubashevski, O.; Freeman, R.; Willner, I. Enzyme cascades activated on topologically programmed DNA scaffolds. *Nat. Nanotechnol.* **2009,** *4*, 249−254.

(11) Park, S.-H.; Zarrinpar, A.; Lim, W. A. Rewiring MAP Kinase Pathways Using Alternative Scaffold Assembly Mechanisms. *Science* **2003,** *299*, 1061−1064.

(12) Idan, O.; Hess, H. Origins of Activity Enhancement in Enzyme Cascades on Scaffolds. *ACS Nano* **2013,** *7*, 8658−8665.

(13) Zhang, Y.; Hess, H. Toward Rational Design of High-efficiency Enzyme Cascades. *ACS Catal.* **2017,** *7*, 6018−6027.

(14) Castellana, M.; Wilson, M. Z.; Xu, Y.; Joshi, P.; Cristea, I. M.; Rabinowitz, J. D.; Gitai, Z.; Wingreen, N. S. Enzyme clustering accelerates processing of intermediates through metabolic channeling. *Nat. Biotechnol.* **2014,** *32*, 1011−1018.

(15) Chavan, K. S.; Calabrese Barton, S. Simulation of Intermediate Channeling by Nanoscale Confinement. *J. Phys. Chem. C* **2018,** *122*, 14474−14480.

(16) Chen, W.-H.; Vázquez-González, M.; Zoabi, A.; Abu-Reziq, R.; Willner, I. Biocatalytic cascades driven by enzymes encapsulated in metal–organic framework nanoparticles. *Nat. Catal.* **2018,** *1*, 689−695.

(17) Ikezoe, Y.; Washino, G.; Uemura, T.; Kitagawa, S.; Matsui, H. Autonomous motors of a metal–organic framework powered by reorganization of self-assembled peptides at interfaces. *Nat. Mater.* **2012,** *11*, 1081−1085.

(18) Riccò, R.; Liang, W.; Li, S.; Gassensmith, J. J.; Caruso, F.; Doonan, C.; Falcaro, P. Metal–Organic Frameworks for Cell and Virus Biology: A Perspective. *ACS Nano* **2018,** *12*, 13−23.

(19) Wheeldon, I.; Minteer, S. D.; Banta, S.; Barton, S. C.; Atanassov, P.; Sigman, M. Substrate channelling as an approach to cascade reactions. *Nat. Chem.* **2016,** *8*, 299−309.

(20) Natinsky, B. S.; Lu, S.; Copeland, E. D.; Quintana, J. C.; Liu, C. Solution Catalytic Cycle of Incompatible Steps for Ambient Air Oxidation of Methane to Methanol. *ACS Cent. Sci.* **2019,** *5*, 1584−1590.

(21) Cui; Wayland, B. B. Superoxo, Peroxo, and Hydroperoxo Complexes Formed from Reactions of Rhodium Porphyrins with Dioxygen: Thermodynamics and Kinetics. *J. Am. Chem. Soc.* **2006,** *128*, 10350−10351.

(22) Idan, O.; Hess, H. Diffusive transport phenomena in artificial enzyme cascades on scaffolds. *Nat. Nanotechnol.* **2012,** *7*, 769−770.

(23) Berben, L. A.; Loewen, N. D. Control of Substrates Beyond the Catalyst Active Site. *ACS Cent. Sci.* **2019,** *5*, 1485−1487.

(24) Wayland, B. B.; Ba, S.; Sherry, A. E. Activation of methane and toluene by rhodium(II) porphyrin complexes. *J. Am. Chem. Soc.* **1991,** *113*, 5305−5311.

(25) Kadish, K. M., Smith, K. M., Guilard, R. *The Porphyrin Handbook*. Elsevier Inc.: 2003; Vol. 16.

Supplementary Information

Derivation of the theoretical framework

Derivation of diffusive conductance (F). We adapt a definition for diffusive conductance (F) where F is proportional to the compartment permeability (p), compartment surface area (SA), and Avogadro's number (N_A), to suit the nanowire array geometry.[9, 26] Permeability of the anaerobic nanowire-based compartment is defined here in terms of the diffusion coefficient (D) and diffusion path length (Δx), where Δx is approximated as being half of the nanowire length, under the assumption that a particular species will traverse, on average, half the length of the nanowire.

$$p \approx \frac{D}{\Delta x} \tag{S4.1}$$

Where $\Delta x = 0.5 \times L$. We note that such an assumption of Δx is an approximate and may incur sizable errors in the calculation of F values (vide infra). Yet, this approximation is experimentalized supported by our previous work, which indicates that the bottom half of the 15 μm wire array is mostly O_2-free.[20]

We then multiplied p by SA and N_A to obtain:

$$F \approx \frac{D \times SA \times N_A}{0.5 \times L} \tag{S4.2}$$

However, in a previous report[9, 26], F is normalized to $V \times N_A$ and then multiplied by concentration in order to obtain the flux of particular species. We postulate that within our nanowire array, F and V will be related, therefore we derive a term for $F/(VN_A)$ as F_V in the unit of s^{-1}. In addition, we derive the volume of the anaerobic compartment as $0.5 \times SA$ multiplied by the length of the compartment, $L - \Delta x = 0.5 \times L$, to obtain the following:

$$F_V = \frac{F}{VN_A} \approx \frac{\frac{D \times SA \times N_A}{0.5 \times L}}{0.5 \times SA \times (L - \Delta x) \times N_A} \quad \text{(S4.3)}$$

$$F_V = \frac{F}{VN_A} \approx \frac{8D}{L^2} \quad \text{(S4.4, Eqn 4.2 in main text)}$$

Furthermore, since all relevant Rh porphyrin species are about the same size, the diffusion coefficient D for the substrate, intermediate, and product (Rh^{III}, Rh^{II}, and Rh^{III}–CH_3, respectively), were approximated as being equal and was previously found for Rh^{III} to be 5.62 x 10^{-10} m^2 s^{-1}.[20]

Lastly, we estimate an error of ±1 μm to Δx in the derivation of $F/(VN_A)$ for the 15 μm wire array experimental reaction efficiency (star with error bar in Figure 4.3). This estimation accounts for variances in the location of the anaerobic region established within the nanowire array compartment, which is evident in our experimental quantification of the locally O_2-free environment in previous report.[20] A more in depth approximation of F is currently being explored, and will be discussed in future work.

Derivation of reaction efficiency γ for nanowire-based compartmentalization. The enclosed reactions within the nanowire domain are represented by rate constants, k, as well as the diffusive conductance, F_V as presented in Figure 4.1C. As Rh^{III} enters the system based on the diffusive conductance, F_V, it is reduced to the active Rh^{II} governed by the kinetic rate of electron transfer, k_1. Then, the rate constant for CH_4 activation within the wire array domain is denoted as k_2, which was previously quantified as 2.9 ×10^4 $L^2 \cdot mol^{-2} \cdot s^{-1}$.[20] However, the reaction of Rh^{II} with CH_4 is contingent on its ability to outcompete diffusion and subsequent elimination with O_2 outside the compartment, k_e, creating the inactive superoxo adduct Rh^{III}–$O_2^{\bullet-}$.[21] Here, k_e is assumed to be infinitely large ($k_e \rightarrow \infty$) such that Rh^{II} in the bulk $[Rh^{II}]_b$ is considered negligible ($[Rh^{II}]_b = 0$). In this system, Rh^{III} is defined as the substrate, Rh^{II} as the intermediate species, and Rh^{III}–CH_3 the

product. Within the model, $C_{Rh,total}$ is the total concentration of Rh species in the bulk solution, almost exclusively in the form of Rh^{III}; C_{CH_4} is the concentration of CH_4 in the bulk solution; $[Rh^{III}]$, $[Rh^{II}]$, and $[Rh^{III}-CH_3]$ are the steady-state concentrations of Rh^{III} that influxes into the compartment, Rh^{II} generated from electroreduction of Rh^{III} within the compartment, and Rh^{III}–CH_3 generated upon CH_4 activation, respectively. Thus, the concentration of each species in the compartment is outlined by equations S4.5–4.8 below:

$$\frac{d[Rh^{III}]}{dt} = F_V(C_{Rh,total} - [Rh^{III}]) - k_1[Rh^{III}] \tag{S4.5}$$

$$\frac{d[Rh^{II}]}{dt} = k_1[Rh^{III}] - k_2[Rh^{II}]^2 C_{CH_4} - F_V([Rh^{II}] - [Rh^{II}]_b) \tag{S4.6}$$

$$\frac{d[Rh^{III}-CH_3]}{dt} = k_2[Rh^{II}]^2 C_{CH_4} - F_V[Rh^{III}-CH_3] \tag{S4.7}$$

$$\frac{d[Rh^{II}]_b}{dt} = F_V([Rh^{II}] - [Rh^{II}]_b) - k_e[Rh^{II}]_b \tag{S4.8}$$

$[Rh^{II}]$ may be solved for in terms of $C_{Rh,total}$ when we assuming $[Rh^{II}]_b = 0$,

$$F_V(C_{Rh,total} - [Rh^{III}]) - k_1[Rh^{III}] = 0 \tag{S4.9}$$

$$F_V C_{Rh,total} = (F_V + k_1)[Rh^{III}] \tag{S4.10}$$

$$[Rh^{III}] = \frac{F_V C_{Rh,total}}{F_V + k_1} \tag{S4.11}$$

Solving for $[Rh^{II}]$ from Equation S6 at steady state leads to the expression of $[Rh^{II}]$:

$$k_2[Rh^{II}]^2 C_{CH_4} + F_V([Rh^{II}] - [Rh^{II}]_b) - k_1[Rh^{III}] = 0 \tag{S4.12}$$

$$[Rh^{II}] = \frac{-F_V + \sqrt{{F_V}^2 + \frac{4F_V k_1 k_2 C_{CH_4} C_{Rh,total}}{F_V + k_1}}}{2k_2 C_{CH_4}} \quad \text{(S4.13)}$$

The expression of $[Rh^{II}]$ leads us to derive the mathematical expression of substrate conversion (R_s), product formation (R_p), and intermediate outflux (R_i) in the compartmentalized system:

$$R_s = k_1[Rh^{III}] = \frac{k_1 F_V C_{Rh,total}}{F_V + k_1} \quad \text{(S4.14)}$$

$$R_i = F_V([Rh^{II}] - [Rh^{II}]_b) \quad \text{(S4.15)}$$

$$R_p = k_2[Rh^{II}]^2 C_{CH_4} \quad \text{(S4.16)}$$

$$\gamma = \frac{R_p}{R_s} = \frac{k_1 F_V C_{Rh,total}}{k_2(F_V + k_1)[Rh^{II}]^2 C_{CH_4}} \quad \text{(S4.17, Eqn 4.1 in main text)}$$

Assuming $[Rh^{II}]_b = 0$, R_s is invariant and remains the same as Equation S4.14. Therefore,

$$R_i = \frac{-{F_V}^2 + F_V\sqrt{{F_V}^2 + \frac{4F_V k_1 k_2 C_{CH_4} C_{Rh,total}}{F_V + k_1}}}{2k_2 C_{CH_4}} \quad \text{(S4.18)}$$

$$R_p = \frac{\left(-F_V + \sqrt{{F_V}^2 + \frac{4F_V k_1 k_2 C_{CH_4} C_{Rh,total}}{F_V + k_1}}\right)^2}{4k_2 C_{CH_4}} \quad \text{(S4.19)}$$

$$\gamma = \frac{(F_V + k_1)\left(-F_V + \sqrt{{F_V}^2 + \frac{4F_V k_1 k_2 C_{CH_4} C_{Rh,total}}{F_V + k_1}}\right)^2}{4F_V k_1 k_2 C_{CH_4} C_{Rh,total}} \quad \text{(S4.20, Eqn 4.3 in main text)}$$

Derivation of reaction efficiency γ for non-compartmentalized homogenous solution. Similar calculations in previous sessions can be applied to the non-compartmentalized scenarios in

homogeneous solutions. While we assuming $k_e \rightarrow \infty$ in previous sections, here k_e is explicitly incorporated.

$$\frac{d[Rh^{III}]}{dt} = -k_1 C_{Rh,total} \tag{S4.21}$$

$$\frac{d[Rh^{II}]}{dt} = k_1 C_{Rh,total} - k_2 [Rh^{II}]^2 C_{CH_4} - k_e [Rh^{II}] \tag{S4.22}$$

$$\frac{d[Rh^{III} - CH_3]}{dt} = k_2 [Rh^{II}]^2 C_{CH_4} \tag{S4.23}$$

Solving for $[Rh^{II}]$ from Equation S12 at steady state:

$$k_2 [Rh^{II}]^2 C_{CH_4} + k_e [Rh^{II}] - k_1 C_{Rh,total} = 0 \tag{S4.24}$$

$$[Rh^{II}] = \frac{-k_e + \sqrt{{k_e}^2 + 4k_1 k_2 C_{CH_4} C_{Rh,total}}}{2k_2 C_{CH_4}} \tag{S4.25}$$

Here, the substrate conversion (R_s'), product formation (R_p'), and intermediate generation (R_i') in the homogeneous solution are expressed as:

$$R_s{}' = k_1 C_{Rh,total} \tag{S4.26}$$

$$R_i' = k_e [Rh^{II}] \tag{S4.27}$$

$$R_p{}' = k_2 [Rh^{II}]^2 C_{CH_4} \tag{S4.28}$$

Taking the expression of $[Rh^{II}]$ leads to the expression of reaction efficiency γ' in homogeneous solution,

$$R_i = \frac{-{k_e}^2 + k_e \sqrt{{k_e}^2 + 4k_1 k_2 C_{CH_4} C_{Rh,total}}}{2k_2 C_{CH_4}} \tag{S4.29}$$

$$R_p = \frac{\left(-k_e + \sqrt{{k_e}^2 + 4k_1k_2C_{CH_4}C_{Rh,total}}\right)^2}{4k_2C_{CH_4}} \quad \text{(S4.30)}$$

$$\gamma' = \frac{\left(-k_e + \sqrt{k_e^2 + 4k_1k_2C_{CH_4}C_{Rh,total}}\right)^2}{4k_1k_2C_{CH_4}C_{Rh,total}} \quad \text{(S4.31, Eqn 4.4 in main text)}$$

Calculation of reaction efficiency in nanowire array compartment.

The experimental calculation of the reaction efficiency γ can be written as:

$$\gamma = \frac{R_p}{R_s} \sim \frac{N_{CH3OH}}{N_{Rh(II)}} = \frac{N_{CH3OH}}{\int Idt - \int IF_{Faradaic}V\frac{\partial Y_{ROS}}{\partial t}dt} \quad \text{(S4.32, Eqn 4.5 in main text)}$$

Here, N_{CH3OH} and $N_{Rh(II)}$ denote the amount of generated CH_3OH and Rh^{II} from electrochemical reduction during the reaction, respectively; I denotes the electric current, $F_{Faradaic}$ the Faradaic constant, V the volume of electrochemical reactor, and $\partial Y_{ROS}/\partial t$ the electrochemical ROS generation rate that can be experimentally determined. The amount of Rh^{II} generated throughout a 3 h electrolysis was determined by the difference in the amount of charge passed (in Coulombs) with and without the pre-catalyst in solution. Under the aforementioned electrolysis conditions with $P_{CH4}/P_{air} = 35$, the total charged passed with and without Rh^{III} in solution was 0.63 C and 0.30 C, respectively. The increase in charge in the presence of Rh^{III} was attributed to the reduction of Rh^{III} to Rh^{II}, which was determined as 0.33 C. This is equivalent to 13.64 μmoles Rh^{II} generated in a 3 h electrolysis. This was converted to Rh^{III}–CH_3 via the reaction stoichiometry of 2 equivalents of Rh^{II} per 1 equivalent of CH_4. Thus, the theoretical maximum CH_3OH synthesized was 6.82 μmoles. This quantity was compared alongside the observed average amount of CH_3OH obtained previously, 5.55 μmoles[20], which resulted in a reaction efficiency of 81 %.

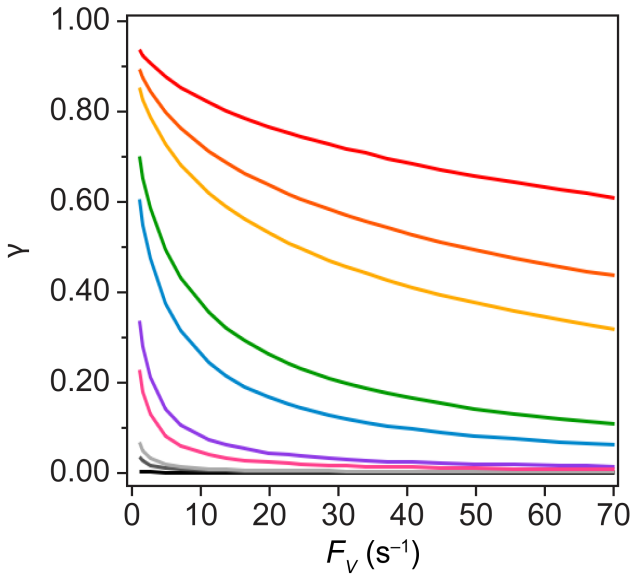

Figure S4.1. Derived values of γ as a function of F_V for an array of k_2 values 0.132 $L^2 \cdot mol^{-2} \cdot s^{-1}$, (black), the experimentally determined value in the bulk solution[5], 5 $L^2 \cdot mol^{-2} \cdot s^{-1}$ (gray), 10 $L^2 \cdot mol^{-2} \cdot s^{-1}$ (silver), 50 $L^2 \cdot mol^{-2} \cdot s^{-1}$ (pink), 100 $L^2 \cdot mol^{-2} \cdot s^{-1}$ (purple), 500 $L^2 \cdot mol^{-2} \cdot s^{-1}$ (blue), 1×10^3 $L^2 \cdot mol^{-2} \cdot s^{-1}$ (green), 5×10^3 $L^2 \cdot mol^{-2} \cdot s^{-1}$ (light orange), 1×10^4 $L^2 \cdot mol^{-2} \cdot s^{-1}$ (dark orange) and the experimentally determined value within the nanowire 2.9×10^4 $L^2 \cdot mol^{-2} \cdot s^{-1}$ (red).

Supplementary References

(26) Berg, H. C. Diffusion Macroscopic Theory. In *Random Walks in Biology*, REV - Revised ed.; Princeton University Press: 1993; pp 17−36.

Chapter 5. Polyketone from carbon dioxide and ethylene by integrating electrochemical and organometallic catalysis

This chapter is a version of unsubmitted work of Natinsky, B. S.; Dodge, H. M.; Zhang, H.; Mu, Y.; Chapp, S. M.; Tran, T. V.; Diaconescu, P. L.; Do, L. H.; Wang, D.; Liu, C.; Miller, A. J. M. "Polyketone from carbon dioxide and ethylene by integrating electrochemical and organometallic catalysis." *In preparation.* **2022.**

Abstract

The integration of multiple catalytic cycles together in one pot continues to be a longstanding challenge. One main hurdle for this scientific marriage resides in the contrasting conditions required for each reaction. Here, we report a two-pot, one vessel integration strategy to merge electrochemical carbon dioxide reduction with the palladium-mediated copolymerization of carbon monoxide and ethylene at room temperature. The electrochemical generation of carbon monoxide enables control over the concentration of the monomer in solution at any given time. With [(DPPP)Pd(Me)(NCMe)][$BAr^F{}_4$] as the polymerization catalyst, perfectly alternating polyketone consisting of 50 wt. % carbon dioxide was synthesized. When (PO)Pd(Me)(pyridine) was substituted in, polyketone of varying carbon monoxide content was afforded (depending on the applied current density) and a carbon monoxide incorporation as low as 5.8 % was achieved. To the best of our knowledge, this is the first report of non-alternating polyketone synthesized at room temperature, owing to the novel reactivity emerging from integrated catalysis. This strategy warrants further study into unifying distinct catalytic reactions to offer new opportunities in sustainable polymer synthesis.

Introduction

The majority of synthetic plastics, adhesives, and other polymer materials are derived from fossil fuels.[1–3] The environmental consequences are significant, as preparation of monomers releases large amounts of carbon dioxide (CO_2) to the atmosphere. [1–4] Furthermore, few of these polymers are readily degraded or recycled.[5–7] One approach to address these challenges is to utilize CO_2 as the source of carbon (and possibly oxygen) in polymer synthesis. [8–12] Polycarbonates can be prepared in this fashion via copolymerization of CO_2 and epoxides.[10–12] Reactions of olefins with CO_2 have been less fruitful, although recent research coupling CO_2 with butadiene had led to polymers incorporating 29 wt% CO_2.[13] General strategies for accessing other classes of polymer materials from CO_2 feedstocks are lacking.

Polyketone materials[14–16] attracted our attention as a possible target for improving sustainability in polymer synthesis. The perfectly alternating copolymer of carbon monoxide (CO) and ethylene (C_2H_4), 1-oxo-trimethylene, is a prototypical example polyketone. Prepared most commonly from molecular palladium (Pd) complex catalysts, 1-oxo-trimethylene materials have extremely high melting points and excellent durability leading to applications as thermoplastics in sectors such as the automotive industry. A few catalysts also produce "non-alternating" polyketones under specific conditions (elevated temperature, low CO pressure relative to C_2H_4 pressure) that feature several C_2H_4 units between each carbonyl group (Figure 5.1).[17–19] These materials have lower melting temperatures and improved solubility, which can enhance processability.[20] At extremely low CO incorporation, non-alternating polyketone behaves more like polyethylene.[21] A recent study demonstrated as low as 0.3% CO incorporation with a nickel complex catalyst, which

produced materials that could be processed like polyethylene but were much more easily degraded due to the isolated ketone functional groups.[21]

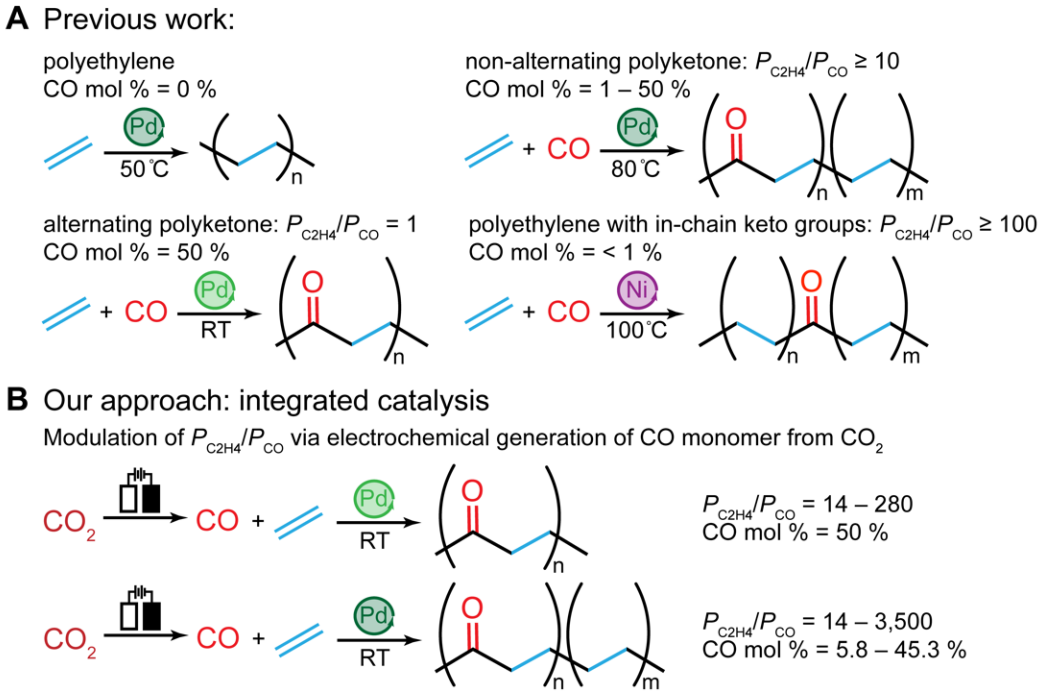

Figure 5.1. Comparison of polyethylene and polyketone synthesized under varying reaction conditions and polymerization catalysts as well as our integrated catalytic approach. (**A**) Previous work on the polymerization of ethylene (C_2H_4) and copolymerization of carbon monoxide (CO) and C_2H_4. Higher partial pressures of C_2H_4 relative to CO, under the right conditions, have led to polyketone with < 1 % CO incorporation. (**B**) Our proposed integrated catalysis which features electrochemically generated CO monomer which, after electrogeneration, is copolymerized alongside C_2H_4 at room temperature. Electrochemical CO synthesis allows for varying CO partial pressures, which, under the right conditions, results in non-alternating polyketone with CO incorporation as low as 5.8 %.

To date, polyketones have been prepared from CO and C_2H_4, which are presently sources from fossil fuel feedstocks (vida supra). CO poses safety concerns in some settings due to its high toxicity. Methods for the sustainable production of CO have been developed, but the fundamental

catalysis tools needed to integrate electrochemical CO_2 reduction with organometallic polymerization catalysis are lacking. The challenge is reflected in the starkly different reaction conditions employed by electrocatalysts and organometallic catalysts. CO_2 electroreduction is most commonly carried out in water at room temperature at 1 bar pressure.[22, 23] Copolymerization of CO and C_2H_4 is usually conducted in organic solvents at ca. 20 bar total pressure and ca. 100 ^oC.[24]

Results and Discussion

Polyketone materials in which each carbonyl unit is derived from CO_2 are reported here, accessed through integration of heterogeneous electrocatalytic CO_2 reduction to CO and homogeneous organometallic CO/C_2H_4 copolymerization catalysis in a single reactor (Figure 5.1). Overcoming incompatibility challenges through reactor design and development of reaction conditions enables the synthesis of perfectly alternating polyketone (1-oxo-trimethylene) that is 50% CO_2-derived by mass. In the integrated catalysis reactor using CO_2 feedstock, non-alternating polyketones can be prepared at room temperature under conditions that produced only 1-oxo-trimethylene in a classical organometallic catalysis reactor using CO feedstock, raising the prospect of unique reactivity via integrated catalysis.

While the electroreduction of CO_2 typically employs an aqueous electrolyte at room temperature and 1 bar CO_2, and Pd-catalyzed polyketone synthesis typically utilizes organic solvents at elevated temperatures and high pressures (vida supra), our initial studies focused on finding suitable solvent, temperature, and pressure conditions under which both the copolymerization catalyst and the electrochemical catalyst could be integrated.

Since organic solvents are preferred for the controlled polymerization of polyketone, the electrochemical reduction of CO_2 to CO was tested in three polar aprotic solvents, 1,2-dichloroethane (1,2-DCE), 1,2-difluorobenzene (1,2-DFB), and N,N-Dimethylformamide (DMF), all with the addition of 5% v/v methanol (MeOH) as a proton donor and 0.25 M tetrabutylammonium hexafluorophosphate ($TBAPF_6$) electrolyte salt. Gold (Au) is amongst the most CO-selective catalysts in aqueous electrolytes[25–29], so we were surprised to find that Au sputtered on carbon paper gave very low Faradaic efficiency (FE) for CO in DMF solvent (Table S5.3). Thus, the need for a nonaqueous solvent for the organometallic catalyst forced us to discover an alternative to the standard CO_2 reduction electrocatalyst materials that would work well in organic solvents.

We turned to Pd next, as Pd has shown a high selectivity for CO from CO_2 in both aqueous and organic electrolytes.[30–33] Room temperature constant current electrolysis in each of the three aforementioned co-solvent systems was performed with a Pd foil working electrode (Table S5.1). CO_2 reduction in 1,2-DCE and 1,2-DFB produced CO with low FE as quantified by online detection with a gas chromatograph (GC). Competing with CO_2 reduction, the hydrodechlorination of 1,2-DCE to C_2H_4 and ethane gas was observed via GC analysis, in line with previous reports that utilize Pd catalysts in 1,2-DCE.[34, 35] When DMF with 5 % v/v MeOH was employed as the electrochemical solvent (and Pd foil working and counter electrodes), the CO yield was higher than the other organic solvents examined. Using pure DMF, with no MeOH present, depressed the competitive hydrogen (H_2) evolution reaction (HER) and further promoted CO_2 reduction to CO (Table S5.1).

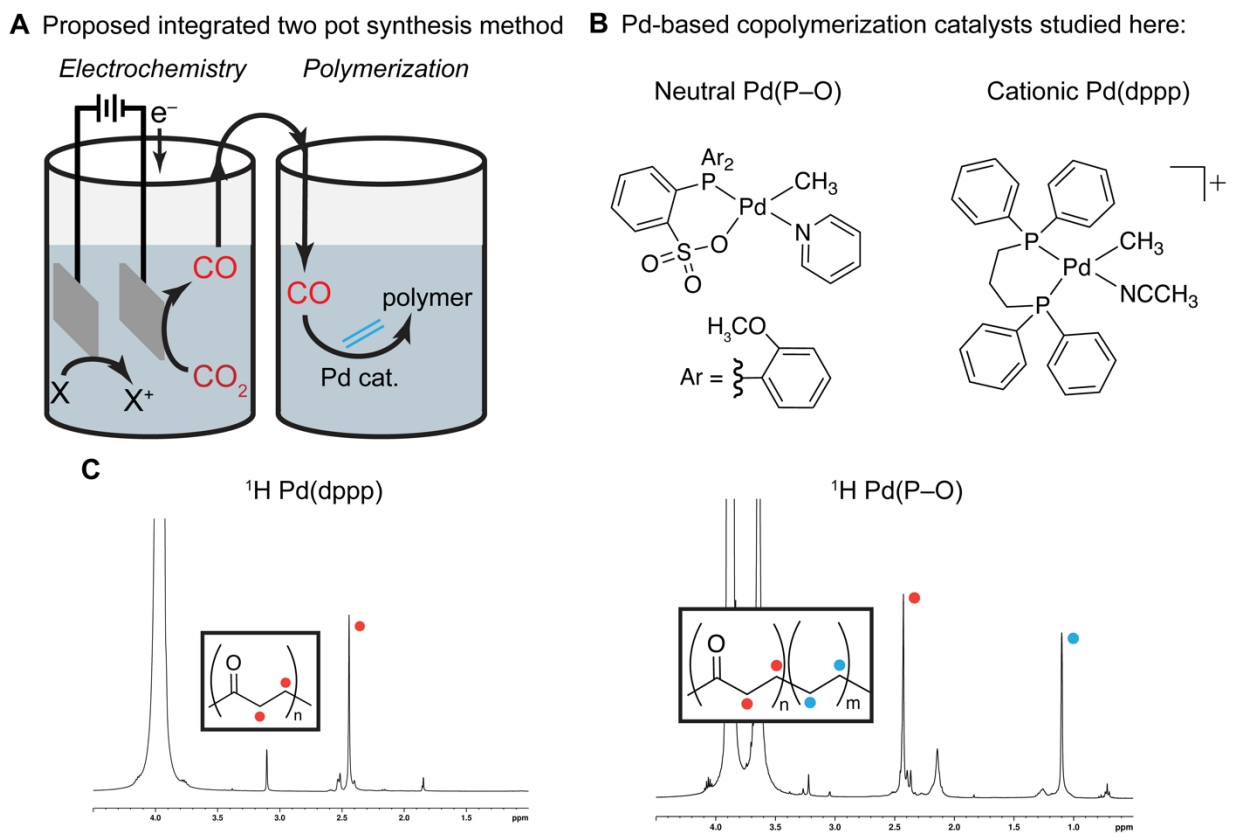

Figure 5.2. Proposed integrated catalysis setup and initial results. (**A**) Proposed integrated catalysis approach featuring a two-pot system in which CO generation and copolymerization are in physically separated beakers. (**B**) The copolymerization catalysts studied, one cationic (Pd(dppp)) and one neutral (Pd(P–O)). (**C**) Initial ^{1}H NMR results of copolymers obtained from integrated catalysis under 0.7 mA·cm^{-2} current density for 24 at room temperature. The precipitate synthesized with Pd(dppp) is perfectly alternating, while that obtained from Pd(P–O) contains a second peak at ~1.2 ppm, owing to the disruption of perfect alternation.

The reaction pressure represented another concern for combining electrochemical and organometallic catalysts, given the high pressures required for traditional polyketone synthesis. We thus sought to identify the minimum C_2H_4 and CO pressures necessary to achieve a suitable rate of copolymerization. Copolymerization of CO and C_2H_4 was thus carried out under similar

conditions as examined in the electrochemical studies, but varying CO and C_2H_4 pressure to see the effect on activity and microstructure in low-temperature copolymerization (Table S5.2). Isolated organometallic catalysts known to lie on the catalytic cycle were utilized to ensure well-defined catalyst species at low temperatures. Two classic catalysts were examined: [(DPPP)Pd(Me)(NCMe)][BAr^F_4] (Pd(dppp)), one of the first reported catalysts for polyketone synthesis, gives exclusively perfectly alternating 1-oxo-trimethylene; (PO)Pd(Me)(pyridine) (Pd(P–O)) was the first catalyst reported to furnish non-alternating polyketone (Figure 5.2B). Non-integrated copolymerization studies show that at least 7 bar C_2H_4 is needed for suitable polymerization activity. However, CO pressures down to 0.5 bar are tolerated, which makes interfacing with electrode-generated CO easier (Table S5.2).

Based on the initial organometallic catalysis experiments showing that at least ca. 7 bar C_2H_4 would be required, high-pressure electrochemical setup was custom-designed (Figure S5.1) in which C_2H_4 monomer and CO_2 could be supplied at various pressures. It was hypothesized that higher pressures of CO_2 would increase CO yield, as the mass transport of CO_2 to the Pd foil working electrode is assumed to be the limiting step.[22, 28] Initial high-pressure electrolysis efforts in a DMF solvent (with no added MeOH) at a current density of 0.7 $mA \cdot cm^{-2}$ and under a total pressure of 14 bar with a 1:1 ratio between CO_2 and C_2H_4 for 3 h resulted in a CO partial pressure of 0.028 bar (FE_{CO} = 18.8) (Table S5.1). The output CO pressure rose to 0.531 bar with a FE for CO of 44.1 % after a 24 h electrolysis, a sufficient amount for integration purposes (Table S5.1).

Initial attempts at catalyst integration under the mutually optimized conditions were thwarted by electroreductive instability of the organometallic Pd complexes. Cyclic voltammograms collected in DMF solvent with 0.25 M $TBAPF_6$ (based on successful CO_2-to-CO electrolysis results) on a glassy carbon working electrode suggest that both complexes undergo irreversible reduction

reactions (Figure S5.2). Versus the ferrocene/ferrocenium redox couple (Fc/Fc^+), Pd(dppp) undergoes initial reduction at –2.85 V and Pd(P–O) at –2.48 V. At a current density of 0.7 $mA \cdot cm^{-2}$, the corresponding output voltage is –3.71 V vs. Fc/Fc^+, and such negative potentials would be expected to decompose both Pd-based complexes preceding the reduction of CO_2 to CO. Complete integration of both catalytic systems in the same solution proved highly challenging. So, to combat the degradation of the polymerization catalysts under CO_2 reduction potentials, we pursued a vial-in-a-vial approach such that the tandem reactions were situated in physically separated beakers within a shared headspace, ultimately allowing for each reaction in its optimized solution (Figure 5.2A). While pursuing CO_2 electrolysis in aqueous electrolyte would be preferred for ample CO generation, we eventually envision a single pot system and organic media are favorable for polymerization activity.

The high-pressure reactor containing DMF and 0.25 M $TBAPF_6$ as electrolyte and a vial of DMF containing 5 mM Pd(dppp) was charged with 7 bar CO_2 and 7 bar C_2H_4 at room temperature, and a current density of 0.7 $mA \cdot cm^{-2}$ was applied for 24 h. An off-white precipitate was observed at the end of the reaction. The solid was isolated, washed with acidified MeOH and characterized by ^1H and ^{13}C nuclear magnetic resonance (NMR) spectroscopy (Figure 5.2C) and infrared (IR) spectroscopy (Figure 5.3). The NMR and IR spectra of the polyketone samples are consistent with a perfectly alternating microstructure, as expected for the catalyst employed. For NMR analysis, the precipitate was dissolved in a 1,1,1,3,3,3-Hexafluoro-2-propanol (HFIP)/C_6D_6 (4:1) mixture. The ^1H NMR signal at 2.5 ppm corresponds to C_2H_4 units in perfect alternation with carbonyl units. The ^{13}C NMR signals at 35 and 212 ppm correspond to the C_2H_4 aliphatic carbons and the ketone carbons of the perfectly alternating units[15, 20, 21], respectively. These experiments thus

demonstrate dual electrochemical/organometallic catalytic synthesis of polyketone that is 50 % CO_2-derived by weight.

The same reactor was employed using Pd(P–O). Based on control experiments, the precipitate formed with the Pd(P–O) catalyst has an extra peak at ~1.2 ppm in the ^{1}H NMR spectrum (in addition to the signal at ~2.5 ppm) which conveys the non-alternating, or extra C_2H_4 units, and multiple peaks in the carbonyl region of the ^{13}C NMR spectrum, owing to the disruption of perfect alternation. Yields of copolymer are higher when using the cationic Pd(dppp) catalyst, which reflects the difference in activity of the cationic vs. neutral catalysts for CO/C_2H_4 copolymerization.[15] As CO incorporation in the polyketone copolymer decreases, solubility in HFIP decreases, but solubility in 1,1,2,2-tetrachloroethane (TCE) increases. NMR spectra were thus also collected in (TCE)-d_2 at 100 °C for comparison with those collected in HFIP. Samples with a high degree of non-alternation (CO incorporation below 25%), exhibit a striking difference in the ^{1}H NMR spectra in HFIP (25° C) vs. TCE (100 °C) (Figure S5.3). In light of this observation, all polymer samples were analyzed in both solvents to allow for a comprehensive microstructure analysis. Attenuated total reflectance-IR (ATR-IR) analysis of the polymer samples made using the cationic Pd(dppp) catalyst show a single C–O stretching frequency of 1692 cm^{-1}, consistent with reports of an alternating copolymer microstructure.[21] The polymer samples made using the neutral Pd(P–O) catalyst reveal C–O stretching frequencies that are dependent on the CO content of the polymer (Figure 5.3). Such shifts in the ATR-IR signals are consistent with reports of non-alternating polyketone. While ATR-IR and NMR spectroscopic studies are indicative of the generation of non-alternating polyketone at room temperature, size exclusion chromatography is

still underway to confirm this and further elucidate molecular weight data and the polydispersity of the synthesized polymers.

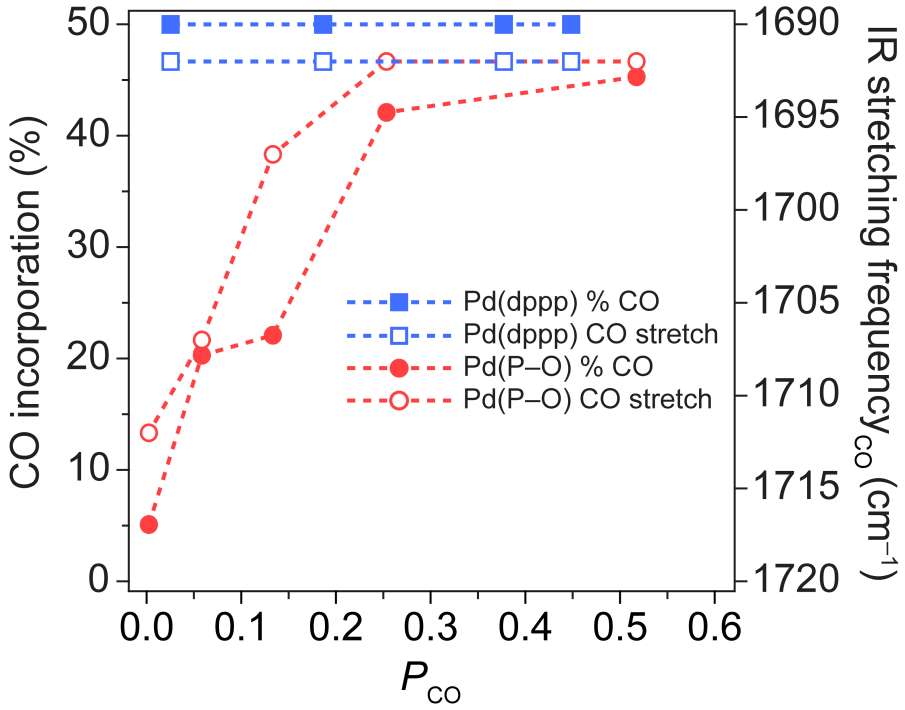

Figure 5.3. CO incorporation percentage and the C–O stretching frequency are plotted against the partial pressure of CO. The cationic Pd(dppp) is plotted in blue with the corresponding CO incorporation (filled blue squares) and IR stretching frequency (open blue squares). The neutral Pd(P–O) is plotted in red with the corresponding CO incorporation (filled red squares) and IR stretching frequency (open red squares).

Most surprising is the generation of non-alternating polyketone at room temperature by Pd(P–O) in the integrated system. In non-integrated copolymerizations under otherwise similar conditions using the Pd(P–O) catalyst, only alternating polyketone is observed at 25 ºC. At elevated temperatures (40–100 ºC), with a 20:1 C_2H_4:CO ratio in the gas feed, non-alternation is observed, and % CO incorporation decreases with increasing temperature (Table S5.2). Generation of CO

monomer from CO_2 presents an opportunity to gain control over the amount of CO available to the copolymerization catalyst at any given time, which could ultimately lead to tunable polyketone microstructures.

The physically separated beakers, applied current to the Pd foil working electrode, and CO_2 and C_2H_4 gasses are all necessary for polymer formation. When Pd(P–O) was dissolved directly in the electrolyte solution, the electrochemically active catalysts were rapidly reduced and deactivated at the Pd foil cathode, inhibiting CO formation, and preventing polymer growth (vide supra) (Table S5.3). Either in the absence of an external applied current or when N_2 is substituted for CO_2 integrated catalysis with Pd(dppp) yielded no precipitate while Pd(P–O) catalyzed the homopolymerization of C_2H_4 (Table S5.3), consistent with previous reports.[36–38] Integrated trials using $^{13}CO_2$ as pre-monomer yielded ^{13}CO, which led to a surge in the characteristic ^{13}C NMR peak (~212 ppm) of the polyketone product.

The electrochemical generation of CO allows for a high degree of control over the monomer's local concentration through varying of the applied current density to the Pd foil cathode. In the case of Pd(dppp), adjusting the current density from 0.7 $mA \cdot cm^{-2}$ to 0.2 $mA \cdot cm^{-2}$ lowers the CO partial pressure from 0.448 to 0.025 bar and consistently results in alternating polyketone with a C–O stretch positioned at 1692 cm^{-1}, denoting CO incorporation = 50 % (Figure 3). Surprisingly, CO partial pressures below 0.2 bar still resulted in precipitate formation. When the current density was lowered to 0.1 $mA \cdot cm^{-2}$ and the resulting CO formed was 0.005 bar there was no observed precipitate in solution. Substituting in the Pd(P–O) catalyst and lowering the current density from 0.7 $mA \cdot cm^{-2}$ to 0.5 $mA \cdot cm^{-2}$ decreased the observed CO partial pressure from 0.517 bar to 0.253 bar. This suppression in CO yield subsequently decreased the % CO incorporation from 45.3 % to 42.1 % (Figure 5.3). Even though there is < 50 % CO content, a single stretching frequency at

1692 cm^{-1} is observed for both of these copolymers, suggesting an alternating microstructure. Successive decreases in current density to 0.3, 0.2 and 0.1 $mA \cdot cm^{-2}$ led to even lower CO partial pressures (0.133 bar, 0.058 bar, and 0.002 bar, respectively) and ultimately decreased the % CO incorporation to 22.1 %, 20.3 %, and 5.8 %, respectively (Figure 5.3). In line with this observation, Figure 5.3 illustrates the corresponding C–O IR stretches shifted to frequencies of 1697, 1707, and 1712 cm-1 at CO pressures of 0.133, 0.058, and 0.002 bar, respectively. The shift of these C–O stretches to values higher than 1692 cm^{-1} correlates with increasing regions of non-alternation within the copolymer.[21] As the high-pressure reactor is initially void of CO, prior to applying a current, Pd(P–O) can homopolymerize C_2H_4, evidenced by our control experiments (Table S5.3) as well as previous literature.[36–38] But, once CO is generated from CO_2 and migrates over to the polymerization beaker, copolymerization of the two monomers can begin.

Conclusion

Integrating electrochemical and organometallic catalysis enables the synthesis of CO_2-derived polyketones. This report provides a blueprint for approaching the challenge of catalyst integration, using a unique reactor design and systematic variation of reaction conditions to achieve suitable conditions for co-catalysis. The integrated system has unexpected emergent properties, wherein non-alternating polyketone was accessible under conditions where traditional homogeneous CO/C_2H_4 copolymerization produced only alternating polyketone. Integrated catalysis produces polyketone materials of variable composition, with the molecular weight and degree of CO incorporation controlled by the choice of organometallic catalyst and applied current density, offering new opportunities in sustainable polymer synthesis.

References

(1) Fagnani, D. E.; Tami, J. L.; Copley, G.; Clemons, M. N.; Getzler, Y. D. Y. L.; McNeil, A. J. 100th Anniversary of Macromolecular Science Viewpoint: Redefining Sustainable Polymers. *ACS Macro Lett.* 2021, *10*, 41–53.

(2) Miller, S. A. Sustainable polymers: replacing polymers derived from fossil fuels. *Polym. Chem.* **2014**, *5*, 3117.

(3) Mecking, S. Nature or Petrochemistry?—Biologically Degradable Materials. *Angew. Chem. Int. Ed.* **2004**, *43*, 1078 –1085.

(4) Gross, R. A.; Kalra, B. Biodegradable Polymers for the Environment. *Science* **2002**, *297*, 803–807.

(5) Zhu, Y.; Romain, C.; Williams, C. K. Sustainable polymers from renewable resources. *Nature* **2016**, *540*, 354–362.

(6) Jambeck, J. R. et al. Plastic waste inputs from land into the ocean. *Science* **2015**, *347*, 768–771.

(7) Philp, J. C.; Bartsev, A.; Ritchie, R. J.; Baucher, M.-A.; Guy, K. Bioplastics science from a policy vantage point. *New Biotechnol.* **2013**, *30*, 635–646.

(8) Markewitz, P. et al. Worldwide innovations in the development of carbon capture technologies and the utilization of CO_2. *Energy Environ. Sci.* **2012**, *5*, 7281–7305.

(9) von der Assen, N.; Voll, P.; Peters, M.; Bardow, A. Life cycle assessment of CO_2 capture and utilization: a tutorial review. *Chem. Soc. Rev.* **2014**, *43*, 7982–7994.

(10) Ren, W. M.; Liu, Z. W.; Wen, Y. Q.; Zhang, R.; Lu, X. B. Mechanistic aspects of the copolymerization of CO_2 with epoxides using a thermally stable single-site cobalt(III) catalyst. *J. Am. Chem. Soc*. **2009**, *131*, 11509–11518.

(11) Ellis, W. C. et al. Copolymerization of CO_2 and meso epoxides using enantioselective β-diiminate catalysts: a route to highly isotactic polycarbonates. *Chem. Sci*. **2014**, *5*, 4004–4011.

(12) Chapman, A. M.; Keyworth, C.; Kember, M. R.; Lennox, A. J. J.; Williams, C. K. Adding value to power station captured CO_2: tolerant Zn and Mg homogeneous catalysts for polycarbonate polyol production. *ACS Catal*. **2015**, *5*, 1581–1588.

(13) Nakano, R.; Ito, S.; Nozaki, K. Copolymerization of carbon dioxide and butadiene via a lactone intermediate. *Nature*, **2014**, *6*, 325–331.

(14) Luo, R.; Newsham, D. K.; Sen, A., Palladium-Catalyzed Nonalternating Copolymerization of Ethene and Carbon Monoxide: Scope and Mechanism. *Organometallics* **2009,** *28*, 6994–7000.

(15) Drent, E.; van Dijk, R.; van Ginkel, R.; van Oort, B.; Pugh, R. I., The First Example of Palladium Catalysed Non-Perfectly Alternating Copolymerisation of Ethene and Carbon Monoxide. *Chem. Commun.* **2002,** *9*, 964–965.

(16) Bettucci, L.; Bianchini, C.; Claver, C.; Suarez, E. J. G.; Ruiz, A.; Meli, A.; Oberhauser, W., Ligand Effects in the Non-Alternating CO–Ethylene Copolymerization by Palladium(II) Catalysis. *Dalt. Trans.* **2007,** *47*, 5590–5602.

(17) Chen, C.; Anselment, T. M. J.; Fröhlich, R.; Rieger, B.; Kehr, G.; Erker, G., o-Diarylphosphinoferrocene Sulfonate Palladium Systems for Nonalternating Ethene–Carbon Monoxide Copolymerization. *Organometallics* **2011,** *30*, 5248–5257.

(18) Hearley, A. K.; Nowack, R. J.; Rieger, B. New Single-Site Palladium Catalysts for the Nonalternating Copolymerization of Ethylene and Carbon Monoxide. *Organometallics* **2005,** *24*, 2755–2763.

(19) Chen, S.-Y.; Pan, R.-C.; Chen, M.; Liu, Y.; Chen, C.; Lu, X.-B., Synthesis of Nonalternating Polyketones Using Cationic Diphosphazane Monoxide-Palladium Complexes. *J. Am. Chem. Soc.* **2021,** *143*, 10743–10750.

(20) Soomro, S. S.; Cozzula, D.; Leitner, W.; Vogt, H.; Müller, T. E., The Microstructure and Melt Properties of CO–Ethylene Copolymers With Remarkably Low CO Content. *Polym. Chem.* **2014,** *5*, 3831–3837.

(21) Baur, M.; Lin, F.; Morgen, T. O.; Odenwald, L.; Mecking, S. Polyethylene materials with in-chain ketones from nonalternating catalytic copolymerization. *Science* **2021**, *374*, 604–607.

(22) Li, F.; Thevenon, A.; Rosas-Hernández, A.; Wang, Z.; Li, Y; Gabardo, C. M.; Ozden, A.; Dinh, C. T.; Li, J.; Wang, Y.; Edwards, J. P.; Yi, Y.; McCallum, C.; Tao, L.; Liang, Z.-Q.; Luo, M.; Wang, X.; Li, H.; O'Brien, C. P.; Tan, C.-S. Nam, D.-H.; Quintero-Bermudez, R.; Zhuang, T.-T.; Li, Y. C.; Han, Z.; Britt, R. D.; Sinton, D.; Agapie, T.; Peters, J. C.; Sargent, E. H. Molecular tuning of CO_2-to-ethylene conversion. Nature 2020, 577, 509–513.

(23) Zheng, T.; Jiang, K.; Wang, H. Recent Advances in Electrochemical CO_2-to-CO Conversion on Heterogeneous Catalysts. *Adv. Mater.* **2018**, *30*, 1802066.

(24) Drent, E.; Budzelaar, P. H. M. Palladium-Catalyzed Alternating Copolymerization of Alkenes and Carbon Monoxide. *Chem. Rev.* **1996**, *96*, 663–682.

(25) Zhao, S.; Jin, R.; Jin, R. Opportunities and Challenges in CO_2 Reduction by Gold- and Silver-Based Electrocatalysts: From Bulk Metals to Nanoparticles and Atomically Precise Nanoclusters. *ACS Energy Lett.* **2018**, *3*, 452–462.

(26) Monteiro, M. C. O.; Philips, M. F.; Schouten, K. J. P.; Koper, M. T. M. Efficiency and selectivity of CO2 reduction to CO on gold gas diffusion electrodes in acidic media. *Nat. Commun.* **2021**, *12*, 1–7.

(27) Marcandalli, G.; Goyal, A.; Koper, M. T. M. Electrolyte effects on the faradaic efficiency of CO_2 reduction to CO on a gold electrode. *ACS Catal.* **2021**, *11*, 4936–4945.

(28) Goyal, A.; Marcandalli, G.; Mints, V. A.; Koper, M. T. M. Competition between CO_2 reduction and hydrogen evolution on a gold electrode under well-defined mass transport conditions. *J. Am. Chem. Soc.* **2020**, *2*, 4154–4161.

(29) Verma, S. et al. Insights into the low overpotential electroreduction of CO2 to CO on a supported gold catalyst in an alkaline flow electrolyzer. *ACS Energy Lett*. **2018**, *3*, 193–198.

(30) Gao, D.; Zhou, H.; Cai, F.; Wang, D.; Hu, Y.; Jiang, B.; Cai, W.-B.; Chen, X.; , Si, R.; , Yang, F.; Miao, S.; Wang, J.; Wang, G.; Bao, X. Switchable CO2 electroreduction via engineering active phases of Pd nanoparticles. *Nano Research* **2017**, *10*, 2181–2191.

(31) Gao, D. F.; Zhou, H.; Wang, J.; Miao, S.; Yang, F.; Wang, G. X.; Wang, J. G.; Bao, X. H. Size-dependent electrocatalytic reduction of CO2 over Pd nanoparticles. *J. Am. Chem. Soc.* **2015**, *137*, 4288–4291.

(32) Noda, H.; Ikeda, S.; Oda, Y.; Imai, K.; Maeda, M.; Ito, K. Electrochemical Reduction of Carbon Dioxide at Various Metal Electrodes in Aqueous Potassium Hydrogen Carbonate Solution. *Bull. Chem. Soc. Jpn*., **1990**, *63*, 2459.

(33) Saeki, T.; Hashimoto, K.; Kimura, N.; Omata, K.; Fujishima, A. Electrochemical reduction of CO_2 with high current density in a CO_2 + methanol medium at various metal electrodes. *J. Electro. Chem.* **1996**, *404*, 299–302.

(34) Ball, M. R.; Rivera-Dones, K. R.; Stangland, E.; Mavrikakis, M.; Dumesic, J. A. Hydrodechlorination of 1,2-dichloroethane on supported AgPd catalysts. *J. Catal.* **2019**, *370*, 241–250.

(35) Heinrichs, B.; Delhez, P.; Schoebrechts, J.-P., Pirard, J.-P. Palladium–Silver Sol-Gel Catalysts for Selective Hydrodechlorination of 1,2-Dichloroethane into Ethylene. *J. Catal.* **1997**, *172*, 322–335.

(36) Nakano, R.; Chung, L. W.; Watanabe, Y.; Okuno, Y.; Okumura, Y.; Ito, S.; Morokuma, K.; Nozaki, K. Elucidating the Key Role of Phosphine−Sulfonate Ligands in Palladium-Catalyzed Ethylene Polymerization: Effect of Ligand Structure on the Molecular Weight and Linearity of Polyethylene. *ACS Catal*. **2016**, *6*, 6101−6113.

(37) Nakamura, A.; Ito, S.; Nozaki, K. Coordination−Insertion Copolymerization of Fundamental Polar Monomers. *Chem. Rev.* **2009**, *109*, 5215–5244.

(38) Mu, H.-L.; Ye, J.-H.; Zhou, G.-L.; Li, K.-K.; Jian, Z.-B. Coordination–insertion copolymerization of polar vinyl monomers by palladium catalysts. *Chinese J. Polym. Sci.* **2020**, *38*, 579–586.

Supplementary Information

Chemicals and methods

Chemicals. The commercial reagents used in the various procedures were purchased from Sigma Aldrich, VWR and Fisher Scientific unless otherwise noted; all chemicals were used as received unless specified. The deionized (DI) water that was used throughout the experiments came from a Millipore Milli-Q Water Purification System. The N,N-Dimethylformamide (DMF) used in all experiments was dried with 3 Å molecular sieves for at least 24 h prior to use.

Chemical and materials characterizations. Spectra of one-dimensional proton nuclear magnetic resonance (^{1}H NMR and ^{13}C NMR) were recorded on a Bruker AV400 spectrometer. Chemical shifts for protons are reported in parts per million (ppm) and deuterated benzene (C_6D_6) or deuterated 1,1,2,2-tetrachloroethane (TCE)-d_2 were used as the locking solvents. A gas chromatograph (GC, SRI 8610C) was used for gas product determination and quantification. A Thermo Scientific Sorvall ST 8 Centrifuge was utilized for separation of the solid precipitate from the liquid solution.

Synthetic procedures

(PO)Pd(Me)(pyridine) (Pd(P–O)). To a solution of 2-[Di(2-methoxyphenyl)phosphino]benzenesolufonic acid (0.5056 g, 1.25 mmol) in dichloromethane (5 mL) was added a solution of Pd(TMEDA)$(CH_3)_2$ (0.3180 g, 1.25 mmol) in dichloromethane (5 mL). The cloudy mixture was stirred at room temperature for 1 h, then pyridine (0.509 mL, 6.29 mmol) was added via syringe. Upon pyridine addition, the mixture turned clear, faintly yellow and was allowed to stir an additional 30 min. The solution was then concentrated under vacuum to a total volume of about 5 mL. Diethyl ether (15 mL) was added, resulting in a fine precipitate. The

pale yellow solids were collected by filtration, washed three times with diethyl ether (10 mL), and dried under vacuum (0.6935 g, 91%).

[(DPPP)Pd(Me)(NCMe)][BAr$^{F}{}_{4}$] (Pd(dppp)). A 20 mL vial was charged with (COD)Pd(Me)(Cl) (0.1055 g, 0.400 mmol) and 1,3 bis(diphenylphosphino)propane (0.1650 g, 0.400 mmol) and dichloromethane (5 mL). The solution was allowed to stir at room temperature for 15 h. The solvent was removed under vacuum and the off-white solid was washed three times with diethyl ether (2 mL). The white solid was dried under vacuum (0.1711 g, 76%). Then, a fresh 20 mL vial was charged with the newly synthesized (dppp)Pd(Me)(Cl) (0.1650 g, 0. mmol), NaBArF4 (0.2574 g, 0. mmol), MeCN (0.30 mL), and dichloromethane (10 mL). The mixture was allowed to stir at room temperature for 15 h. The mixture was filtered and the filtrate was concentrated under vacuum to yield an orange solid (0.3988 g, 96%).

Electrochemical measurements

Electrochemical CO_2 reduction. Non-integrated electrolysis measurements were performed using a Gamry Instruments Interface 1000-E potentiostat. The electrolyte solution was composed of 0.25 M $TBAPF_6$ dissolved in DMF that had been dried with 3 Å molecular sieves for at least 24 h. The solution volume was 200 mL and the gas headspace was ~750 mL (the value used for Faradaic efficiency calculations). A two-electrode setup was utilized. The working electrode was Pd foil with an average surface area of ~130 cm^2 and the counter/reference electrode was Pd foil as well. The constant current electrolysis was conducted under a constant I_{appl} of 90 mA resulting in a current density of 0.7 $mA \cdot cm^{-2}$. CO_2 gas (Airgas, 99.999 %) and C_2H_4 gas (Airgas, 99.9 %) were charged into the high-pressure reactor such that the total pressure was 14 bar and $P_{CO2}/P_{C2H4} = 1$. The constant current electrolysis was run for 24 h. The gas headspace of the reactor was sampled via online detection with a gas chromatograph before and after electrolysis. The amount of CO

and H_2 produced was quantified with a standard calibration gas mixture (0.5 % CO_2, 0.5 % CO, 0.5 % H_2, and 0.5 % O_2 in N_2). After the reaction, the Pd foil electrodes were sequentially rinsed and sonicated in acetone, DI water, and dilute nitric acid. To determine the potential at the working Pd foil electrode, a Ag^+/Ag pseudo-reference electrode with a glass frit was added and the output potential was calibrated versus the ferrocene/ferrocenium redox couple.

Cyclic voltammetry of Pd copolymerization catalysts. Cyclic voltammograms of both Pd complexes were collected on a CH Instruments 630D potentiostat. In an Ar-filled glovebox, cyclic voltammetry (CV) was performed on both a 1 mM Pd(dppp) solution and 1 mM Pd(P–O) solution (in separate trials) in a glass vial equipped with a Teflon top fitted with electrode and gas inlet/outlet ports. The cell contained 0.25 M $TBAPF_6$ in DMF with a Pt wire counter electrode, a Ag^+/Ag pseudo-reference electrode with a glass frit, and a 3 mm diameter glassy carbon working electrode. CVs were collected under scan rates of 50, 100, 200, and 500 mV/s. The reported data are after *iR* correction. Cyclic voltammograms of ferrocene were also conducted to calibrate the potentials of Ag^+/Ag pseudo-reference electrode.

Copolymerization of CO and C_2H_4

Pd-assisted CO/C_2H_4 copolymerization. In a nitrogen glovebox, a 5 mM stock solution of Pd catalyst was prepared in the solvent of choice. Aliquots (1 mL) of the stock solution were transferred to Agilent 2 mL vials via syringe (3-5 vials in total). The vials were sealed with caps that have pre-cut septa, which allow gas to enter, and placed in a Cat18 high pressure reactor (HEL Group). The reactor was sealed and brought outside the glovebox. The reactor was placed on a heating/stirring plate and connected to a high pressure gas manifold equipped with carbon monoxide, ethylene, and nitrogen gases. CO (Airgas, 99.999 %) was added to the desired pressure first. If low CO pressures were desired (e.g. 0.5 bar), the reactor was first pressurized to 20 bar

with carbon monoxide and nitrogen (10 bar each) and then vented to atmospheric pressure. Once the desired CO pressure was reached, the reactor was pressurized with C_2H_4 gas (Airgas, 99.9 %). To end the reaction, the reactor was vented to atmospheric pressure and the vials were retrieved. The contents of the vials were combined into a single scintillation vial. MeOH (10 mL) and 35% HCl (0.6 mL) were added and the mixture was stirred vigorously for at least 4 h. The solids were then collected by vacuum filtration and dried under vacuum.

Integrated catalysis

Integrated catalysis combining electrochemical CO_2 reduction and CO/C_2H_4 copolymerization. Electrolysis measurements were performed using a Gamry Instruments Interface 1000-E potentiostat. The integrated reaction setup was composed of physically separated vessels, one containing the electrolyte solution and the other housing the polymerization solution, within a high-pressure reactor (Parr Instrument) fitted with electrochemical feedthroughs. The electrolyte solution, roughly 200 mL (contained in the larger vessel), was composed of 0.25 M $TBAPF_6$ dissolved in DMF that had been dried with 3 Å molecular sieves for at least 24 h. In a typical experiment, a two-electrode cell was used. The working electrode was Pd foil with an average surface area of ∼130 cm^2 and the counter/reference electrode was Pd foil as well. The constant current electrolysis was conducted under a constant I_{appl} of 90 mA resulting in a current density of 0.7 $mA \cdot cm^{-2}$. For current densities of 0.5, 0.3, 0.2, and 0.1 $mA \cdot cm^{-2}$ the applied current was 65, 39, 26, and 13 mA, respectively. The polymerization vessel contained 5 mM of the Pd complex. In the case of Pd(dppp), Pd(dppp) was dissolved in 10 mL of DMF while Pd(P–O) was dissolved in 10 mL of 1,2-DCE. CO_2 gas (Airgas, 99.999 %) and C_2H_4 gas (Airgas, 99.9 %) were charged into the high-pressure reactor such that the total pressure was 14 bar and $P_{CO2}/P_{C2H4} = 1$. In conjunction, control experiments were conducted with flowing N_2 in place of CO_2 at the same total

pressure, but P_{N2} = 5 bar and P_{C2H4} = 9 bar. The integrated experiment was run for 24 h. The gas headspace of the reactor was sampled via online detection with a gas chromatograph before and after electrolysis. The amount of CO and H_2 produced was quantified with a standard calibration gas mixture (0.5 % CO_2, 0.5 % CO, 0.5 % H_2, and 0.5 % O_2 in N_2). After the reaction, the Pd foil electrodes were sequentially rinsed and sonicated in acetone, DI water, and dilute nitric acid. Upon completion of the integrated catalysis, and a precipitate was generated in the polymerization beaker, the polymerization solution was transferred to a 50 mL centrifuge tube where 15 mL of methanol and 3 mL of hydrochloric acid (HCl) were added. This mixture was sonicated overnight to facilitate the dissolution of Pd and then the mixture was centrifuged at 7500 rpm for 15 min. Once the solid was concentrated to the bottom of the tube, the supernatant was discarded. The process of solid suspension and centrifugation was repeated 3 more times. The resulting off-white precipitate was collected and dried under vacuum overnight. Then, the air-stable samples collected at UCLA were shipped to UNC – Chapel Hill for characterization.

Product quantification

Gas product quantification from CO_2 electrolysis. The gas products of CO_2 reduction were quantified via online detection with a GC (SRI 8610C). The valve oven temperature was set to 175 ºC. The carrier gas was argon which was supplied at a pressure of 15 psi and a flow rate of 40 mL/min. Upon sample injection, the initial column temperature was held at 50 ºC for 1 min, after which the temperature ramp rate was 20 ºC/min with a final temperature of 90 ºC. The column temperature was held at 90 ºC for 3.75 min. Then, at a ramp rate of 30 ºC/min, the temperature was increased to 210 ºC. Three columns were utilized within the GC in the following order: a 0.5 m Haysep-D pre-column, a 2 m MoleSieve5A column, and a 2 m Haysep-D column. Both a flame ionization detector equipped with a methanizer (FIDm) and a thermal conductivity detector (TCD)

were used for sample quantification. Hydrogen was supplied to the FID from a H_2-100 Hydrogen Generator at a pressure of 20 psi and a flow rate of 30 mL/min. Air was also supplied to the FID at a pressure of 5 psi and a flow rate of 250 mL/min.

CO was quantified at a retention time of ~5.45 min on the spectrum obtained from the FIDm and H_2 was quantified at a retention time of ~1.25 min on the spectrum obtained from the TCD. The amount of CO and H_2 produced was quantified with a standard calibration gas mixture (0.5 % CO_2, 0.5 % CO, 0.5 % H_2, and 0.5 % O_2 in N_2).

NMR of copolymers synthesized via integrated and non-integrated catalysis. Once the crude precipitates were isolated, washed, and dried, they were subjected to ^{1}H and ^{13}C NMR on a Bruker AV400 spectrometer to confirm polymer synthesis. For all samples, NMR spectroscopy was conducted in a HFIP/C_6D_6 (4:1) mixture at room temperature and (TCE)-d_2 at 100 ºC for accurate comparison. The percentage of CO incorporation in the polymer was quantified via ^{1}H NMR.

Infrared spectroscopic analysis. Attenuated total reflectance-infrared spectroscopy (ATR-IR) was employed to observe the C–O stretching frequency in the polymer. ATR-IR spectra of polymers were acquired on a Perkin Elmer Spectrum 100 instrument. The IR resonances of ketones gradually shift with their spatial proximity, from 1712 cm^{-1} for a low density of C=O groups to 1692 cm^{-1} for alternating polyketones.

Table S5.1. Summary of CO_2 electrolysis experiments for reaction optimization.

Working electrode	Counter electrode	Solvent	Additive (H^+ donor)	Current density (mA/cm^2)	Duration (h)	Temperature (°C)	P_{CO2} (bar)	P_{Total} (bar)	FE_{CO} (%)	P_{CO} (bar)	FE_{H2} (%)
Pd foil	Pd foil	1,2-DCE[a]	5 % MeOH[b]	0.45	6	25	1	1	~15	N/A[c]	~12
Pd foil	Pd foil	1,2-DCE	5 % MeOH	0.45	6	40	1	1	< 1	N/A	~4
Pd foil	Pd foil	1,2-DCE	5 % MeOH	0.45	6	60	1	1	< 1	N/A	~8
Pd foil	Pd wire	1,2-DCE	5 % MeOH	1.20	12	25	5	10	0.3	0.0003	2.5
Pd foil	FTO[d]	1,2-DCE	5 % MeOH	0.70	6	25	5	10	5.3	0.003	1.0
Pd foil	Pd foil	1,2-DCE	5 % MeOH	0.70	24	25	5	10	2.5	0.002	1.7
Au-C[e]	Au-C	1,2-DCE	5 % MeOH	0.70	1.5	25	8	23	10	< 0.0001	22.3
Pd foil	Pd foil	1,2-DFB[f]	5 % MeOH	0.45	6	25	1	1	~21	N/A	~11
Pd foil	Pd foil	1,2-DFB	5 % MeOH	0.45	6	40	1	1	< 1	N/A	~6
Pd foil	Pd foil	1,2-DFB	5 % MeOH	0.45	6	60	1	1	< 1	N/A	~7
Pd foil	Pd foil	1,2-DFB	5 % MeOH	0.70	12	25	6	12	12.4	0.019	19.4
Pd foil	Pd foil	1,2-DFB	5 % MeOH	0.70	24	25	6	12	1.3	0.004	29.3
Pd foil	FTO	1,2-DFB	5 % MeOH	0.70	24	25	6	12	< 1	0.0001	23.4
Au-C	Au-C	1,2-DFB	5 % MeOH	0.70	2	25	8	23	< 1	< 0.0001	25.5
Au-Ti[g]	Au-Ti	1,2-DFB	5 % MeOH	0.70	2	25	8	23	< 1	< 0.0001	22.1
Pd foil	Pd foil	DMF[h]	5 % MeOH	0.70	3	25	7	14	18.8	0.028	31.5
Pd foil	Pd foil	DMF	5 % MeOH	0.70	6	25	7	14	14.4	0.043	45.1
Pd foil	Pd foil	DMF	5 % MeOH	0.70	12	25	7	14	17.2	0.103	58.4
Pd foil	Pd foil	DMF	5 % MeOH	0.70	24	25	7	14	7.9	0.095	67.8
Au-Ti	Au-Ti	DMF	10 % H_2O + 5 mM $CsCO_3$[i]	0.70	15	25	8	23	7.5	0.056	20.5
Au-Ti	Au-Ti	DMF	10 % MeOH	0.70	2	25	8	23	6.5	0.008	35.7
Pd foil	Pd foil	DMF	5 % H_2O	0.70	12	25	7	14	5.3	0.032	41.0
Pd foil	Pd foil	DMF	3 % AA[j]	0.70	12	25	7	14	3.9	0.006	47.6
Pd foil	Pd foil	DMF	None	0.70	24	25	7	14	86.0	0.518	0.9
Pd foil	Pd foil	DMF	None	0.70	24	25	7	14	44.1	0.531	22.3
Pd foil	Pd foil	DMF	None	0.70	24	25	7	14	34.6	0.493	32.3

[a]1,2-DCE, 1,2-dichloroethane [b]MeOH, methanol [c]total CO pressure was unable to be quantified because a flow cell open to air was utilized [d]FTO, fluorine-doped tin oxide [e]Au-C, gold sputtered on carbon [f]1,2-DFB, 1,2-difluorobenzene [g]Au-Ti, gold sputtered on titanium [h]DMF, N,N-Dimethylformamide [i]$CsCO_3$, cesium carbonate [j]AA, acetic, acid

Table S5.2. Summary of non-integrated copolymerization experiments.

Catalyst	[Catalyst] (mM)	Solvent	Temperature (°C)	Duration (h)	P_{CO} (bar)	P_{C2H4} (bar)	P_{CO2} (bar)	P_{H2} (bar)	Yield (mg)	Activity ($g \cdot mmol \cdot Pd^{-1} \cdot h^{-1}$)
Pd(P–O)	10	1,2-DCE[a]	40	2	0.5	10.5	0	0	22.5	0.75
Pd(P–O)	10	1,2-DCE	40	2	1	11	1	0	26.9	0.45
Pd(P–O)	10	1,2-DCE	40	2	1	10	10	0	32.6	0.54
Pd(P–O)	10	1,2-DCE	40	2	1	11	11	1	33.0	0.55
Pd(P–O)	5	1,2-DCE	25	24	0.5	10.5	0	0	45.0	0.08
Pd(P–O)	10	1,2-DCE	40	24	0.5	10.5	0	0	123.3	0.17
Pd(P–O)	5	1,2-DCE	60	24	0.5	10.5	0	0	318.2	0.53
Pd(P–O)	10	1,2-DCE	80	2	0.5	10.5	0	0	103.7	1.73
Pd(P–O)	5	1,2-DCE	100	2	0.5	10.5	0	0	683.9	13.68
Pd(P–O)	5	1,2-DCE	25	24	0.5	10.5	0	0	45.0	0.08
Pd(P–O)	5	1,2-DCE	25	24	5	10	0	0	61.8	0.10
Pd(P–O)	5	1,2-DCE	25	24	10	10	0	0	63.0	0.11
Pd(dppp)	5	DMF[b]	25	24	0.5	10	0	0	102.0	0.43
Pd(dppp)	5	DMF	25	24	5	10	0	0	461.4	0.77
Pd(dppp)	5	DMF	25	24	10	10	0	0	491.1	0.82

[a]1,2-DCE, 1,2-dichloroethane [b]N,N-Dimethylformamide

Table S5.3. Integration control experiments

Entry	Gas mixture	Current density (mA/cm^2)	Polymerization catalyst	P_{Total} (bar)	P_{CO} (bar)	FE_{CO} (%)	Polymer yield (mg)
1	$CO_2 + C_2H_4$	0.70	None (DMF)	14	0.422	35.0	N/A
2	$CO_2 + C_2H_4$	None	Pd(dppp)	14	0.0	0.0	N/A
3	$N_2 + C_2H_4$	0.70	Pd(dppp)	14	0.0002	0.01	N/A
4	$CO_2 + C_2H_4$	0.70	None (1,2-DCE)	14	0.471	39.2	N/A
5	$CO_2 + C_2H_4$	None	Pd(P–O)	14	0.0	0.0	39.0 (polyethylene)
6	$N_2 + C_2H_4$	0.70	Pd(P–O)	14	0.0001	0.01	25.5 (polyethylene)
7[a]	$CO_2 + C_2H_4$	0.70	Pd(P–O)	25	0.083	2.2	2.1

[a]Pd(P–O) was dissolved directly in the electrolyte solution.

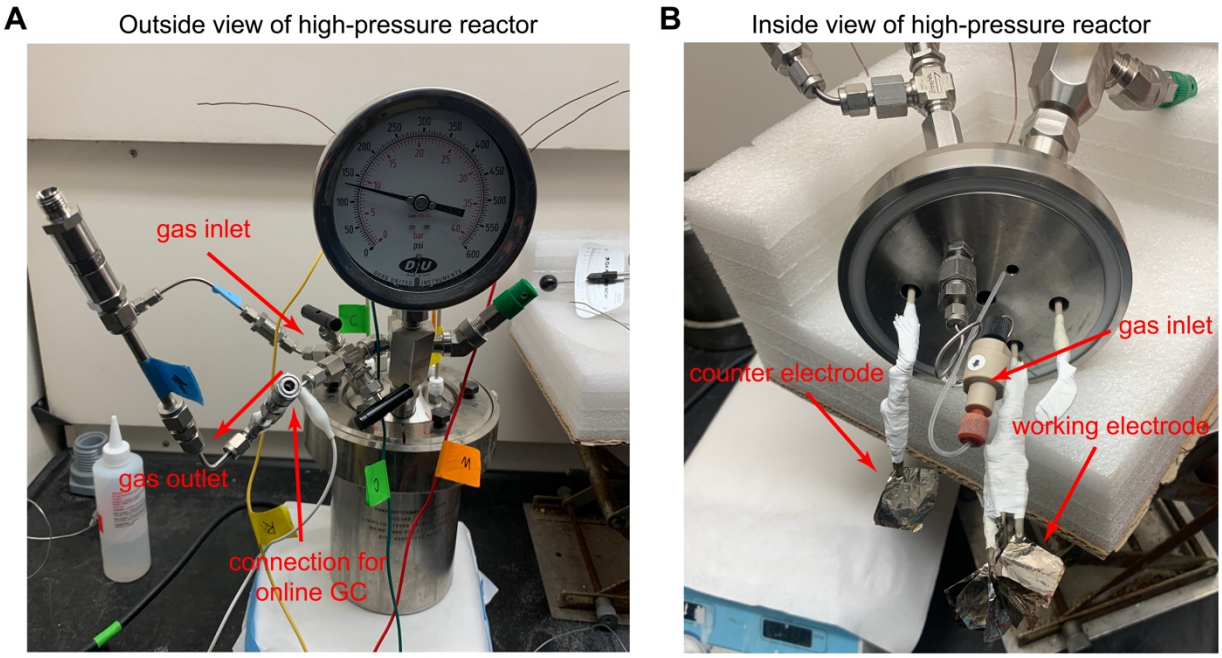

Figure S5.1. Photograph of high-pressure reactor fitted with electrochemical feedthroughs for integrated catalysis. (**A**) outside view and (**B**) inside view of reactor.

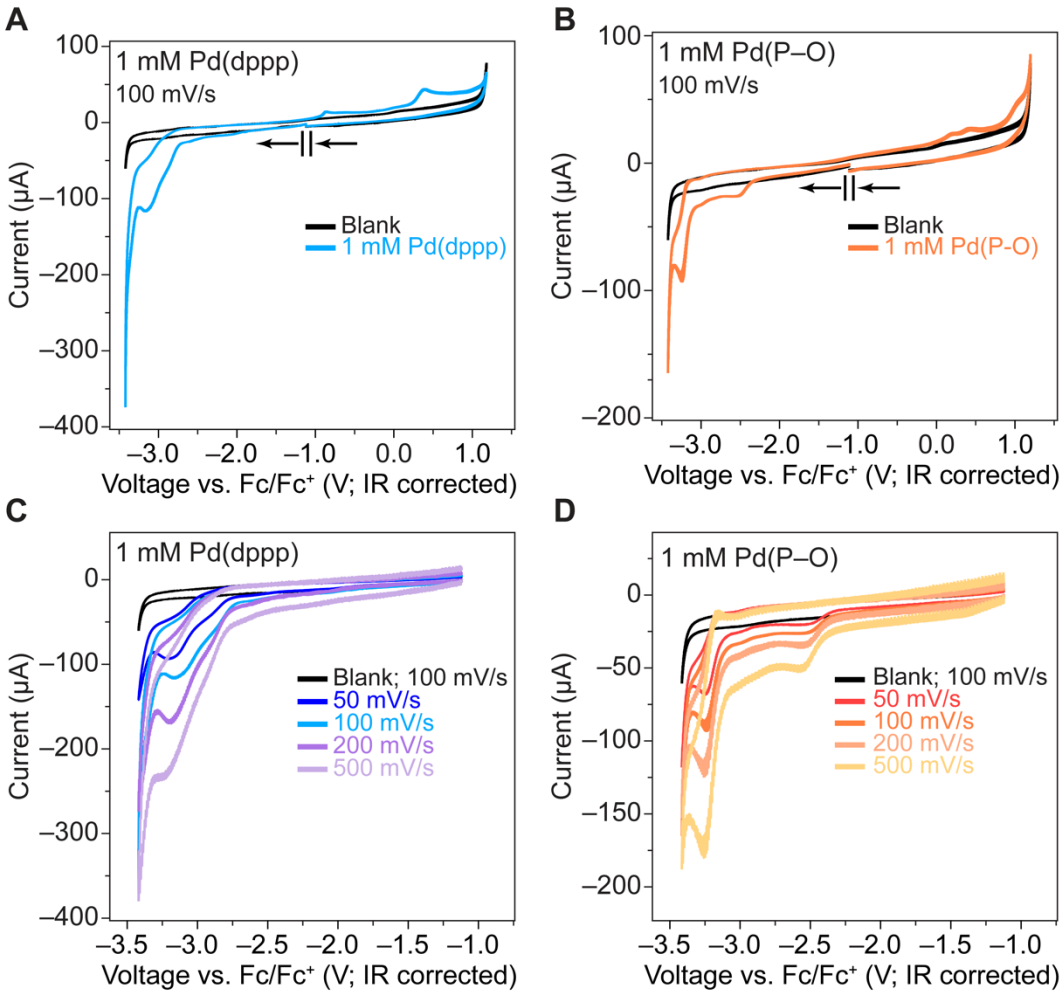

Figure S5.2. Cyclic voltammograms of both Pd(P–O) and Pd(dppp) copolymerization catalysts. (**A**) blank trace (black, no Pd(dppp)) and 1 mM Pd(dppp) (light blue) and (**B**) blank trace (black, no Pd(P–O)) and 1 mM Pd(P–O) (orange) at a scan rate of 100 mV/s. (**C**) 1 mM Pd(dppp) at scan rates of 50 mV/s (navy blue), 100 mV/s (light blue), 200 mV/s (purple), and 500 mV/s (light purple) (**D**) 1 mM Pd(P–O) at scan rates of 50 mV/s (red), 100 mV/s (dark orange), 200 mV/s (orange), and 500 mV/s (light orange). Glassy carbon working electrode, platinum wire counter electrode, and Ag/Ag^+ pseudo-reference electrode. 0.25 M tetrabutylammonium hexafluorophosphate in N,N-Dimethylformamide. Potentials, after *IR* compensation, are referenced to the ferrocene/ferrocenium redox couple (Fc/Fc^+).

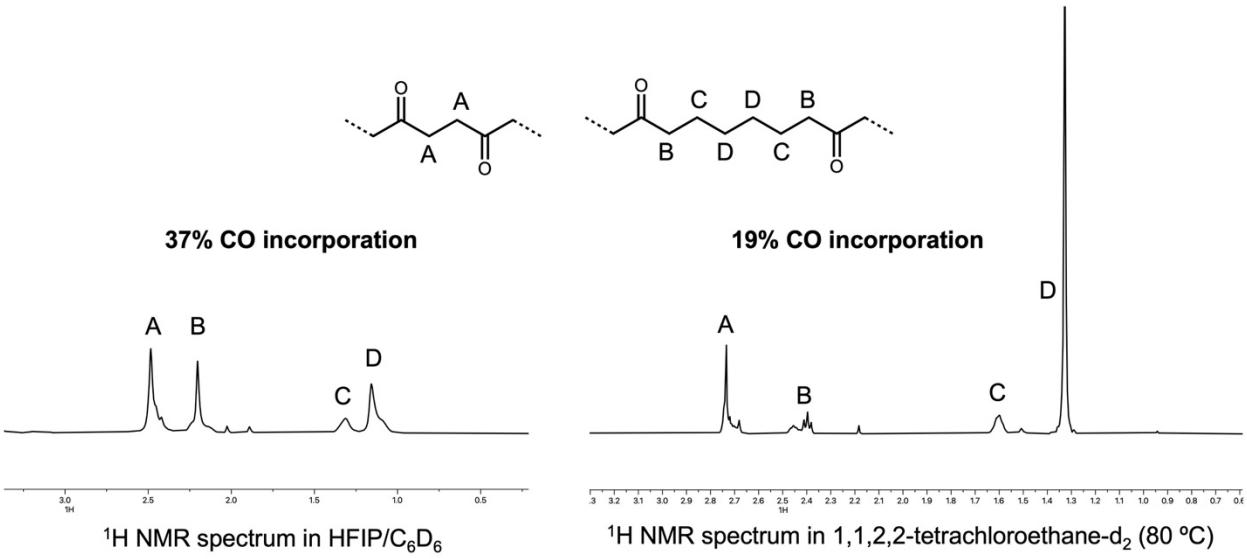

Figure S5.3. ^{1}H nuclear magnetic resonance spectra of a precipitate synthesized from the neutral Pd(P–O) copolymerization catalyst. The left spectrum shows the precipitate dissolved in 1,1,1,3,3,3-hexafluoro-2-propanol/C_6D_6 (4:1) mixture and the spectrum is collected at room temperature and on the right the polymer is dissolved 1,1,2,2-tetrachloroethane-d_2 and the spectrum is collected at 80 ºC.

Chapter 6. Concluding Remarks

The science I have presented in this dissertation highlights the work throughout my graduate student career in integrating nanomaterials and electrochemistry with homogeneous organometallic catalysis with the goal of circumventing incompatibilities and uncovering unforeseen reaction routes. We showed that the application of sufficient cathodic potential to a silicon nanowire array working electrode in air engenders a steep O_2 concentration gradient, such that the area near the bottom of the wires (where the base of the wires meets bulk silicon) is rendered anaerobic. Thus, we created a pseudo "mini glove box" in air. The spatiotemporal control we achieved over O_2 resolved the reaction incompatibility and promoted the ambient air oxidation of CH_4 to CH_3OH with an O_2-sensitive Rh^{II} metalloradical complex. This compelled us to question the role of the nanowire array electrode as a microcompartment. We validated the efficacy of the nanowire microcompartment which enhanced the rate of reaction by retaining the Rh^{II} intermediate in order to promote anaerobic C–H activation, which would be impossible in a purely homogeneous solution.

In my current work, we translated the O_2 gradient we observed previously with the goal of applying this phenomenon to the electrochemical reduction of CO_2 to CO. The ultimate goal of this project is to couple the catalytic reactions of electrochemical CO generation from CO_2 and Pd-catalyzed CO/C_2H_4 copolymerization in one pot. However, this project currently lies in the two-pot, one-vessel stage in which each catalytic reaction is physically separated within a single high-pressure reactor. Initial results illustrate the room temperature synthesis of CO_2-derived polyketone that is upwards of 50 wt. % CO_2 (with the cationic, symmetric Pd complex). Varying the applied current density controls the output pressure of CO, leading to non-alternating polyketone with a CO incorporation as low as 5.8 % (with the neutral, asymmetric Pd complex). The synthesis of non-

alternating polyketone, to our knowledge, is the first instance in which non-alternation has been achieved at room temperature, owing to unique reactivity within the integrated system.

There are many avenues that this project can be taken after the completion of my thesis. The first hurdle we must traverse is to take our current two-vessel approach to a single beaker. While the electrochemical deactivation of the Pd complexes poses a challenge based on the applied potentials, anchoring the copolymerization catalysts to a surface can reconcile this incompatibility. By tethering through the ligand backbone, the polymer chain and monomer binding sites remain accessible, but the polymerization activity of the grafted complexes must be retained. Once we have an active anchored complex, we will have added a dimension of spatial control to the temporal control we already have established. At this stage, efforts will be focused on the room temperature synthesis of non-alternating polyketone mediated by the neutral Pd(P–O) complex. Concurrent finite-element simulations with the COMSOL software can guide experimental efforts by predicting the percentage of CO incorporation in the polymer as a function of the distance between the cathode (CO generation) and the anchored Pd(P–O) catalyst (CO and C_2H_4 consumption). Further temporal control can be achieved by introducing pulses within the chronopotentiometry experiments such that the applied current density, and thus CO available for copolymerization, can be turned on and off on demand. Additionally, with the introduction of a nanostructured electrode (i.e. wire array) as the site of CO generation, we can harness tunable CO spatial gradients and we can visualize such gradients through spectroelectrochemical techniques in which we monitor the intensity of the C–O stretch in solution during electrolysis. With precise spatiotemporal control of CO in hand, we hope to gain access to the first non-alternating gradient polyketone materials by varying the degree of non-alternation throughout the poylmer's microstructure that will unlock polyketone materials with unknown and unique properties.